# Glass-Based Anodes for Lithium-Ion Batteries

Yan, Jiajia

*DOI (link to publication from Publisher):*
10.54337/aau499833222

*Publication date:*
2022

*Document Version*
Publisher's PDF, also known as Version of record

# GLASS-BASED ANODES FOR LITHIUM-ION BATTERIES

BY
JIAJIA YAN

DISSERTATION SUBMITTED 2022

AALBORG UNIVERSITY
DENMARK

# GLASS-BASED ANODES FOR LITHIUM-ION BATTERIES

by

Jiajia Yan

AALBORG UNIVERSITY
DENMARK

Dissertation submitted 2022

Dissertation submitted: September 2022

PhD supervisor: Prof. Yuanzheng Yue,
Aalborg University

PhD committee: Associate Professor Morten Lykkegaard Christensen
Aalborg University, Denmark (chair)

Professor Poul Norby
Technical University of Denmark, Denmark

Associate Professor Elie-Elisee Georges Paillard
Politecnico di Milano, Italy

PhD Series: Faculty of Engineering and Science, Aalborg University

Department: Department of Chemistry and Bioscience

ISSN (online): 2446-1636
ISBN (online): 978-87-7573-820-5

Published by:
Aalborg University Press
Kroghstræde 3
DK – 9220 Aalborg Ø
Phone: +45 99407140
aauf@forlag.aau.dk
forlag.aau.dk



Printed in Denmark by Stibo Complete, 2022

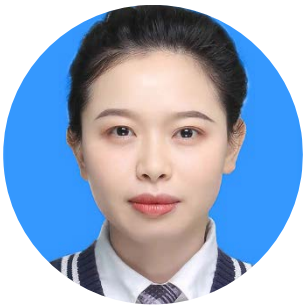

# CV

Ms. Jiajia Yan was born in Mianyang, Sichuan, P. R. China in May 1991. She received her Bachelor's degree and Ph.D. degree in Material Science from Fuzhou University, P. R. China, in 2014 and 2022, respectively. She started her PhD study at Department of Chemistry and Bioscience in Aalborg University in October 2019, which is funded by China Scholarship Council (CSC). Her research focused on glass-based anode materials for lithium-ion batteries during her three-year PhD study at AAU.

# ENGLISH SUMMARY

Lithium-ion batteries (LIBs) are one of the most advanced energy storage devices in modern society due to their high energy density, long lifespan, and environmental friendliness, etc. However, the fast-growing large-scale smart grids and electric vehicle market urgently demand better performances with lower cost of LIBs. To meet the demands, new anode materials with higher capacity have been extensively investigated. Glass materials show great potentials as anode materials owing to their unique disordered open network, tunable composition, simple preparation process, low cost and excellent cycling stability, etc. Nonetheless, the specific capacities of glasses are still far from satisfactory for high energy density devices. To overcome this problem, in this thesis, we combined silicon (Si), which has high theoretical capacity but poor cycling stability due to volume changes, with glasses and fabricated Si-glass composite anodes. The structure and electrochemical performances of two types of glasses (vanadium-tellurite glass and metal-organic framework glass) based anodes have been investigated.

To find an effective strategy to combine Si with vanadium-tellurite glass (VT), two methods, i.e., traditional heat-treatment and hot-pressing methods, have been explored. The latter method allows Si to be embedded in the VT matrix, and thus the Si/VT composite produces a synergistic effect as the volume change of Si can be buffered by the VT matrix. The formation of $V^{4+}$ arising from the redox reaction between Si and $V^{5+}$ during heat-treatment increases the electronic conductivity. Moreover, the glass open network provides numerous channels for both $Li^+$ storage and transport. Therefore, the Si/VT composite exhibits better electrochemical performances than pristine Si and VT.

In addition, by combining the reflux and melt-quenching methods, Si nanoparticles were wrapped into a subset of metal-organic framework (MOF) glass, i.e., cobalt-ZIF-62 glass, chemical formula $Co(imidazole)_{1.75}(benzimidazole)_{0.25}$. The ZIF glass not only possesses an open network structure beneficial for $Li^+$ diffusion, but also buffers the volume change of Si during cycling. After 500 cycles, the lithiation/delithiation could induce pronounced structural changes of the ZIF, i.e., the distortion or breakage of Co-N, and aromatic rings, leading to an increase in structural defects and diffusion channels for the transport and storage of $Li^+$. Furthermore, the increased channels lead to more $Li^+$ ions going into ZIF and reacting with Si, and thereby achieving a strong synergistic effect and exhibiting excellent reversible capacity, rate capability and cycling stability.

# DANSK RESUME

Litium-ion-batterier (LIB'er) er en af de mest avancerede energilagringsenheder i det moderne samfund på grund af deres høje energitæthed, lange levetid og miljøvenlighed osv. Men det hurtigt voksende storskala smarte net og elbilmarked kræver batterier med bedre ydeevne og levetid. For at imødekomme kravene er nye materialer til anoder med højere kapacitet blevet grundigt undersøgt. Glasmaterialer viser stort potentiale som et materiale til anoder, på grund af deres unikke uordnede åbne netværk, fleksibel sammensætning, enkle forberedelsesproces, lave omkostninger og fremragende levetid osv. Ikke desto mindre skal kapaciteten af glas materialerne stadig forbedres yderligere. For at løse dette problem har vi i dette speciale kombineret silicium, som har høj teoretisk kapacitet, men lav stabilitet på grund af volumenændringer, med glas og kompositanoder fremstillet af Si og glas. Strukturen og den elektrokemiske ydeevne af to typer glas (vanadium-tellurit-glas og metal-organiske netværker) baserede anoder er blevet undersøgt.

For at finde en effektiv strategi til at kombinere Si med vanadium-tellurit glas (VT), er to metoder, dvs. traditionel varmebehandling og varmpresningsmetoder, blevet forsøgt. Sidstnævnte metode tillader Si at blive del af VT-matricen, og således producerer Si/VT-kompositten en synergetisk effekt, da volumenændringen af Si kan hæmmes af VT-matricen. Dannelsen af $V^{4+}$ som følge af redoxreaktionen mellem Si og $V^{5+}$ under varmebehandling øger den elektroniske ledningsevne. Desuden giver det åbne glasnetværk adskillige kanaler til både $Li^{+}$ opbevaring og transport. Derfor udviser Si/VT-kompositten bedre elektrokemisk ydeevne end uberørt Si og VT.

Ved at kombinere tilbagesvaling og smelte-køling metoder blev Si nanopartikler desuden pakket ind i en undergruppe af metal-organiske netværker (MOF) glas, dvs. Cobalt-ZIF-62 glas, med kemisk formel $Co(imidazolate)_{1,75}(benzimidazolate)_{0,25}$. ZIF-glasset har ikke kun en åben netværksstruktur, der er gavnlig for Li+-diffusion, men reducerer også volumenændringen af Si under cykling. Efter 500 cyklusser af lithiering/delithiering skete der strukurelle og kemiske ændringer af ZIF anoden, dvs. forvrængning eller brud af Co-N bindinger og aromatiske ringe, hvilket fører til en stigning i strukturelle defekter og diffusionskanaler til transport og opbevaring af $Li^{+}$. Ydermere fører de øgede kanaler til, at flere $Li^{+}$ ioner går ind i ZIF og reagerer med Si, og derved opnår en stærk synergetisk effekt og udviser fremragende reversibel kapacitet, god kinetik og cyklusstabilitet.

# ACKNOWLEDGEMENTS

I would like to express my gratitude to a great number of people for their help during my Ph.D. study. Without their support, it would not be possible for me to accomplish PhD study and research. First and foremost, I would like to thank my supervisor Professor Yuanzheng Yue. I met him on a glass conference in Kunming, China in 2018, when I was a Ph.D. student at Fuzhou University. I was thrilled by his extensive and deep scientific knowledge and his cautious attitude toward research work after getting to know him. It encouraged me to come to Denmark to learn from him as a guest PhD student in 2019 first and then he enrolled me as a full-time Ph.D. at Aalborg University (AAU). With his guidance and support, I feel comfortable to conduct my research independently. We had spent a lot of time together sharing research ideas, discussing experimental results, revising our papers as well as chatting about interesting things in life. I am very grateful to him for enrolling me as a full-time Ph.D. at AAU and for his dedicated supervision in my Ph.D. study.

Then, I would like to give my appreciation to my co-supervisor Professor Hongbing Zhan. When I was at Fuzhou University, she encouraged me to go to Denmark and learn from Professor Yuanzheng Yue. She recommended me to Yuanzheng and also guided my first Ph.D. project (sealing glass for solid oxide fuel cells). With her supervision, I got my Ph.D. degree from Fuzhou University in June 2022.

Next, I would like to thank Professor Zhang from Qilu University of Technology. Her research creativity, scientific insight and working efficiency inspired me. Discussions with her are always joyful and meaningful. Whenever she revised my academic manuscripts, her writing skills impressed me and stimulated me to improve my writing ability. With her kind help, I collected important battery data for my Ph.D. project at AAU.

It is a marvelous experience to work with all my colleagues in the chemistry section. They helped me so much in supporting my experiments and reviewing my paper, as well as other leisure activities, like cake sharing. I would like to thank my colleagues and collaborators: Assoc. Prof. Morten Lykkegaard Christensen, Assoc. Prof. Vittorio Boffa, Assoc. Prof. Donghong Yu, Prof. Morten M. Smedskjær, Assoc. Prof. Thorbjørn Nielsen, Assoc. Prof. Mads Jørgensen, Dr. Ang Qiao, Dr. Chengwei Gao, Dr. Zhencai Li, Dr. Rasmus R. Petersen, Dr. Linling Tan, Dr. Junwei Ding, Dr. Junjun Tan, Dr. Qi Zhang, Dr. Tao Du, Dr. Martin Østergaard, Dr. Theany To, Dr. Pengfei Liu, Dr. Fengchao Li, Rasmus Madsen, Wessel M.W. Winters, Søren Sørensen, Wei Fan, Xiangting Ren, Wei Xu, Johan Christensen, Xianzheng Ma, Xinxin Chen, Zhimin Chen, Daming Sun, Annemarie Davidsen, Anne Flensborg, Timo Kirwa, Michelle Hyldegård Mortensen, Mette Haferbier.

During my external study at Wuhan University of Technology and Fuzhou University, I also had a great time because of many brilliant and supportive co-workers. I am very grateful to Prof. Haizheng Tao, Prof. Ang Qiao, Dr. Qidi Chen, Dr. Zhenhuan Zheng, Dr. Qingming Huang, Dr. Xiang Hu, Zijuan Du, Xuefei Ke, Qingshuang Zheng, Penghui Li, Meizi Xu, Xin Huang, Hemin Zhou, Feiyue Xia, Ban Fei, Junhao Dong, Yaxuan Zhuang, Mincai for the great help in both research and life when I study there. I really enjoy working together with them and I hope they will enjoy their academic life and have a bright future. The experiences are so memorable that I will never forget the fantastic moments there.

I also appreciate my collaborators for their scientific assistance and helpful discussions. They are Prof. Jinjun Ren, Dr. TongYao Zhao, Nianshi from Shanghai institute of Optics and Fine Mechanics, Chinese Academy of Sciences, Assoc. Prof. Lars Jensen from Aalborg University, Dr. Zhaoyang Wang and Dr. Fangyu Xiong from Wuhan University of Technology, Zhengjing Jiang, Shibin Qi, Peixing Wang from Qilu University of Technology. Dr. Chengwei Gao from Ningbo University. It is my great lucky to work with them. I also would like to thank for the support from China Scholarship Council (CSC). It provides me a great opportunity to conduct my research with many talent researchers and scientists.

Furthermore, I would personally give my tremendous appreciation to my friends: Ning Xu, Juan Han, Miaomiao, Jinfeng, Xiaoguang, Luona, Hanyu, XiaoYue, Xiaohui, Taixiong, Lisa, Elisabeth, Cathrine, Sofie. It is lovely to have them around.

My great thanks go to my husband Jianxin, my parents, my brothers and sisters, and my parents-in-law. I could not imagine how I would be without their encouragement and love. I survived my Ph.D. study, and I really appreciate their support. I love all of you forever!

# LIST OF ABBRIVATIONS

| | |
|---|---|
| VT | Vanadium-tellurite glass |
| VTS | Composite composed of Si doped into vanadium-tellurite glass |
| 10VTS | 10 wt.%Si and 90 wt.% vanadium-tellurite glass composite |
| 20VTS | 20 wt.%Si and 80 wt.% vanadium-tellurite glass composite |
| 30VTS | 30 wt.%Si and 70 wt.% vanadium-tellurite glass composite |
| 40VTS | 40 wt.%Si and 60 wt.% vanadium-tellurite glass composite |
| HP | Hot-pressing method |
| MOF | Metal-organic frameworks |
| ZIF | Zeolitic imidazolate framework |
| Cobalt-ZIF-62 | $Co(imidazole)_{1.75}(benzimidazole)_{0.25}$ |
| Im | Imidazole |
| BIm | Benzimidazole |
| DMF | N,N-Dimethylformamide |
| Z | Zeolitic imidazolate framework crystal |
| ZG | Zeolitic imidazolate framework glass |
| SiZGC | Composite containing Si and ZIF-glass |
| SiZC | Composite containing Si and ZIF-crystal |
| XRD | X-ray diffraction |
| DSC | Differential scanning calorimetry |
| $T_g$ | Glass transition Temperature |
| $T_{c1}$ | Onset temperature of the first crystallization |
| $T_{c2}$ | Onset temperature of the second crystallization |
| $T_{c3}$ | Onset temperature of the third crystallization |
| $T_m$ | Melting point |
| $T_{max}$ | Maximum DSC scanning temperature |
| SEM | Scanning electron microscopy |
| TEM | Transmission electron microscopy |
| HRTEM | High-resolution Transmission Electron Microscopy |
| EDS | Energy-dispersive X-ray spectrometer or spectra |
| NMR | Nuclear magnetic resonance |
| XPS | X-ray photoelectron spectroscopy |
| FTIR | Fourier-transform infrared spectroscopy |
| GCD | Galvanostatic charge-discharge |
| CV | Cyclic voltammetry |
| EIS | Electrochemical impedance spectroscopy |
| $R_e$ | Ohmic resistance |
| $R_s$ | Solid electrolyte interface resistance |
| $R_{ct}$ | Charge transfer resistance |
| $C_{PE}$ | Capacitance |
| $Z_w$ | Diffusion impedance |
| σ | Warburg factor |

# TABLE OF CONTENTS

**Chapter 1. Introduction** ..... **1**

1.1. Background and Challenges ..... 1

1.2. Objectives ..... 3

1.3. Thesis Contents ..... 4

**Chapter 2. Experimental Sections** ..... **5**

2.1. Synthesis ..... 5

2.1.1. Vanadium-Tellurite Glasses (VT) ..... 5

2.1.2. Si/VT Composites ..... 5

2.1.3. Colbalt-ZIF-62 Crystals/Glasses ..... 6

2.1.4. Si@ZIF-62 Composites ..... 6

2.2. Characterization Methods ..... 6

2.2.1. X-ray Diffraction (XRD) ..... 6

2.2.2. Differential Scanning Calorimetry (DSC) ..... 7

2.2.3. Raman Spectroscopy ..... 7

2.2.4. Attenuated Total Reflection Fourier Transform Infrared Spectroscopy (ATR-FTIR) ..... 7

2.2.5. X-Ray Photoelectron Spectroscopy (XPS) ..... 7

2.2.6. Solid-State Nuclear Magnetic Resonance (NMR) ..... 7

2.2.7. Scanning Electron Microscopy (SEM) ..... 8

2.2.8. Transmission Electron Microscopy (TEM) ..... 8

2.3. Electrochemical Methods ..... 8

2.3.1. Cyclic Voltammetry ..... 9

2.3.2. Galvanostatic Charge-Discharge ..... 9

2.3.3. Electrochemical Impedance Spectroscopy ..... 9

**Chapter 3. Structrue and Crystallization of VT and Si/VT-Glass Composites .11**

3.1. Characterizations of VT and Si/VT Composites ..... 11

3.1.1. Phase and Thermodynamic Analyses of VT and VTS ..... 11

3.1.2. Structural Analyses of VT and VTS ..... 14

3.2. Electrochemical Performances of VT and VTS ..... 20

3.3. Summary ..... 21
**Chapter 4. Optimizing Performances of Si/VT-Glass Composites by Hot Pressing ..... 23**
4.1. Characterations of Si/VT Composites ..... 23
4.1.1. Phase and Thermodynamic Analyses ..... 23
4.1.2. Morphological and Structural Chracterizations ..... 25
4.2. Electrochemical Performances ..... 27
4.2.1. Cycling Performance ..... 27
4.2.2. Rate Performance ..... 28
4.2.3. Cyclic Voltammetry Curve ..... 29
4.2.4. Electrochemical Impedance Spectra ..... 31
4.3. Proposed Mechanism ..... 32
4.4. Summary ..... 32
**Chapter 5. Structure and Performances of Si@MOF-Glass Composites ..... 33**
5.1. Characterization of Si@ZIF Composites ..... 33
5.1.1. Phase and Thermodynamic Analyses ..... 33
5.1.2. Morphological and Structural Chracterizations ..... 35
5.2. Electrochemical Performances ..... 36
5.2.1. Cycling Performance ..... 36
5.2.2. Rate Performance ..... 37
5.2.3. Cyclic Voltammetry Curve ..... 38
5.2.4. Electrochemical Impedance Spectra ..... 39
5.3. Characterizations of Si@ZIF Composites after Charging/Discharging Cycling ..... 39
5.3.1. Structural and Morphorlogical Characterizations ..... 39
5.3.2. Cyclic Voltammetry Curve ..... 43
5.3.3 Electrochemical Impedance Spectra ..... 43
5.4. Proposed Mechanism ..... 44
5.5. Summary ..... 45
**Chapter 6. General Discussions ..... 47**
**Chapter 7. Conclusions and Perspectives ..... 49**
7.1. Conclusions ..... 49

7.2. Perspectives..... 50
**Biography.....53**
**List of Publications.....61**
**Teaching Activities.....61**

# TABLE OF FIGURES

Fig. 1-1 Schematic illustration of the Li-ion battery. The graphite anode and $LiCoO_2$ cathode are attached to copper and aluminum foils acting as the current collectors, respectively [4]..... 2
Fig. 3-1 DSC upscan curves of both VT and VTS, which are obtained at 10 K/min in argon. The characteristic temperatures such as glass transition ($T_g$) and crystallization onset temperatures ($T_{c1}$, $T_{c2}$, and $T_{c3}$) are denoted in the curves..... 12
Fig. 3-2 DSC upscan curves of both VT and VTS, which are obtained at 10 K/min in argon. (a) DSC upscan to 650K for three times. (b) DSC upscan to 650K for the first time and then to 725K for the second and third times. The characteristic temperatures such as glass transition ($T_g$) and crystallization onset temperatures ($T_{c1}$, $T_{c2}$, $T_{c3}$ and $T_{c4}$) are denoted. ..... 13
Fig. 3-3 XRD patterns of (a) VT and (b) VTS after the first, second and third DSC upscans to 650K at 10 K/min in argon. ..... 13
Fig. 3-4 XRD patterns of VT and VTS after two DSC upscans at 10 K/min in argon. The first upscan was carried out to 650 K and the second one was to 725K, which are referred to as VT-650-725 and VTS-650-725, respectively. ..... 14
Fig. 3-5 Possible linkage modes between (a) $VO_4$ tetrahedra, (b) $VO_5$ trigonal bipyramids (tbps) with $TeO_3$ or $TeO_4$ in vanadium-tellurite glasses [34]. ..... 14
Fig. 3-6 $^{51}V$ NMR spectra of (a) VT and (b) VTS samples before and after two different DSC upscans at 10 K/min in argon. For VT/VTS-650-2, samples were upscanned to 650K twice, while for VT/VTS-650-725, samples were upscanned to 650K first and then to 725K. The deconvolution of $^{51}V$ NMR spectra for VT/VTS (c), VT/VTS-650-2 (d), and VT/VTS-650-725 (e). Purple and green curves represent the $VO_4$ and $VO_5$ contributions, respectively. ..... 15
Fig. 3-7. $^{125}Te$ NMR spectra of (a) VT and (b) VTS samples before and after two different DSC upscans at 10 K/min in argon. For VT/VTS-650-2, samples were upscanned to 650K twice, while for VT/VTS-650-725, samples were upscanned to 650K first and then to 725K. Dashed lines: the fitting curves. ..... 16
Fig. 3-8 XPS high-resolution of Si 2p(a) and V 2p (b) spectra for VTS and VTS-650. ..... 17
Fig. 3-9 (a) $^{29}Si$ NMR spectra of VTS upscanned in DSC to $T_g \sim 2.1T_g$ at 10 K/min in argon (b) $^{51}V$ NMR spectra of VTS upscanned in DSC to $T_g \sim 1.4T_g$ at 10 K/min in argon (c) deconvolution of $^{51}V$ NMR spectra shown in (b). ..... 18
Fig. 3-10 The dependences of both $Si_{(dec.)}/(Si+SiO_2)$ and $VO_{4(trans.)}/((VO_4+VO_5)$ on the DSC $T_{max}$ for VTS samples. The $T/T_g$ represents the ratio of the $T_{max}$ to the glass transition temperature of VTS……18
Fig. 3-11. FTIR spectra of Si and VTS after upscanning in DSC to $T_g$, $1.1T_g$ and $1.2T_g$ at 10 K/min in argon. ..... 19
Fig. 3-12. Schematic diagram of the reaction between Si and VT glass (a), and the evolution of $[VO_4]$ to $[VO_5]$ (b) when VTS was upscanned by DSC to 725K at 10 K/min in argon. ..... 20

Fig. 3-13. The cycling performance of anodes based on the VTS, VTS-650-2, VTS-650-725, Nano Si, VT, VT-650-2, VT-650-725 at 0.1 A $g^{-1}$ for 50 cycles. ..... 21
Fig. 4-1 XRD patterns of 10VTS-550-HP, 10VTS-570-HP, 10VTS-620-HP, 10VTS-670-HP, and 10VTS-770-HP. ..... 23
Fig. 4-2 DSC upscan curves of both 10VTS and 10VTS-620-HP, which are obtained at the rate of 10 K/min in argon. The characteristic temperatures such as glass transition ($T_g$) and crystallization onset temperatures ($T_{c1}$, $T_{c2}$, and $T_{c3}$) are denoted in the curves. ..... 24
Fig. 4-3 SEM images and EDS elemental mappings of Si, V and Te. (a) 10VTS-620, (b) 10VTS-620-HP, (c) 10VTS-670-HP, where the number, i.e., 10, represents the introduction of 10 wt.% Si nanoparticles into VT..... 25
Fig. 4-4 FTIR spectra of Si, 10VTS, 10VTS-620, 10VTS-620-HP, where the number, i.e., 10, represents the introduction of 10 wt.% Si nanoparticles into VT. ..... 26
Fig. 4-5 XPS high-resolution of Si 2p(a) and V 2p (b) spectra for 10VTS, 10VTS-620, 10VTS-620-HP, and 10VTS-670-HP. ..... 26
Fig. 4-6 Cycling performances of anodes based on Si, VT, 10VTS-570-HP, 10VTS-620-HP, 10VTS-670-HP, 10VTS-770-HP, 10VTS-620, 20VTS-620-HP, 30VTS-620-HP, and 40VTS-620-HP. ..... 27
Fig. 4-7 The rate performances of anodes based on Si, 10VTS-570-HP, 10VTS-620, 10VTS-620-HP, 10VTS-670-HP, 10VTS-770-VTS, 20VTS-620-HP, 30VTS-620-HP, and 40VTS-620-HP at current densities of 0.1, 0.2, 0.5, 1, 2 A $g^{-1}$. ..... 28
Fig. 4-8 Cyclic Voltammetry (CV) curves of 10VTS-620-HP(a), 10VTS-670-HP(b), 30VTS-620-HP(c), 40VTS-620-HP(d) within the range from 0.01 to 3.0 V at a scan rate of 0.1 mV $s^{-1}$..... 30
Fig. 4-9 Nyquist plots of 10VTS-620-HP and 10VTS-670-HP, which were obtained from electrochemical impedance spectra within the frequency range from 0.01 Hz to 100 kHz. ..... 31
Fig. 4-10 The protecting role of VT glass matrix, which prolongs the cycling life of Si. ..... 32
Fig. 5-1 XRD patterns of the ZIF-62 crystal (Z), ZIF-62 glass (ZG), 10Si@ZIF-62 composite (10SiZC), 10Si@ZIF-62-glass composite (10SiZGC), and the simulated ZIF-62 crystal, where the number, i.e., 10, represents that weight percent of Si nanoparticles introduced into ZIF-62. ..... 34
Fig. 5-2 DSC upscan curves (a) and thermogravimetric curves (b) of the ZIF crystal (Z), ZIF glass (ZG), 10Si@ZIF composite (10SiZC), and 10Si@ZIF-glass composite (10SiZGC), which were obtained at 10 °C $min^{-1}$ in argon. ..... 34
Fig. 5-3 (a) SEM images of the 10Si@cobalt-ZIF-62composite (10SiZC) (Inset: EDS elemental mappings of Co, N and Si for SZ); (b) SEM images of the 10Si@cobalt-ZIF-62-glass composite (10SiZGC). ..... 35
Fig. 5-4 (a)FTIR spectra of Z, ZG, 10SiZC and 10SiZGC. (b) Raman spectra of 10SiZC and 10SiZGC. ..... 36
Fig. 5-5 (a) The cycling performances of anodes based on the ZIF crystal (Z), ZIF glass (ZG), 5Si@ZIF composite (5SiZC), 5Si@ZIF-glass composite (5SiZGC), 10Si@ZIF composite (10SiZC), 10Si@ZIF-glass composite (10SiZGC), 15Si@ZIF

composite (15SiZC), and 15Si@ZIF-glass composite (15SiZGC) at 1 A $g^{-1}$ for 500 cycles, and (b) cycling performance of 10SiZGC at 1 A $g^{-1}$ for 1000 cycles..... 37
Fig. 5-6 The rate performances of anodes based on the 5SiZC, 5SiZGC, 10SiZC, 10SiZGC, 15SiZC, and 15SiZGC at current densities of 0.1, 0.2, 0.5, 1, 2, 5 and 0.1A $g^{-1}$. ..... 38
Fig. 5-7 Cyclic Voltammetry (CV) curves of pristine 10SiZGC within the range from 0.01 to 3.0 V at a scan rate of 0.1 mV $s^{-1}$. ..... 38
Fig. 5-8 Nyquist plots of 10SiZC and 10SiZGC before and after cycling obtained from electrochemical impedance spectra within the frequency range from 0.01 Hz to 100 kHz. ..... 39
Fig. 5-9. XPS high-resolution spectra of Co 2p (a), N 1s (b), Si 2p (c) and C 1s (d) for 10SiZC and 10SiZGC before and after cycling. ..... 40
Fig. 5-10 FTIR spectra (a) and XRD patterns (b) of the 10SiZC and 10SiZGC after cycling. ..... 41
Fig. 5-11 (a), (c) TEM images and EDS mappings of Si, N, Co for 10SiZGC and 10SiZC after cycling, respectively. (b), (d) HRTEM images and the corresponding SAED patterns of 10SiZGC and 10SiZC after cycling. ..... 42
Fig. 5-12 Cyclic Voltammetry (CV) curves of 10SiZGC after 500 cycles within the range from 0.01 to 3.0 V at a scan rate of 0.1mV $s^{-1}$ ..... 43
Fig. 5-13 (a) Nyquist plots of 10SiZC and 10SiZGC after cycling obtained from electrochemical impedance spectra within the frequency range from 0.01 Hz to 100 kHz. (b) The dependence of Z' on $\omega^{-1/2}$ in the low-frequency region obtained from Nyquist plots in Figs. 5-8, 5-13a. ..... 44
Fig. 5-14 The protecting role of ZIF glass matrix, which prolongs the cycling life of Si. ..... 44

# TABLE OF TABLES

Table 3-1 The fraction of $VO_5$ and $VO_4$, which were obtained from the deconvoluted $^{51}V$ NMR spectra shown in Fig. 3-6. ..... 16
Table 3-2 The fraction of Si, $SiO_2$ of VTS and VTS-650, which were obtained from the deconvoluted Si 2p XPS spectra shown in Fig. 3-8a. ..... 17
Table 4-1 The fraction of Si, $SiO_2$ of VTS, VTS-620, VTS-620-HP, VTS-670-HP, which were obtained from the deconvoluted Si 2p XPS spectra shown in Fig. 4-5. 27
Table 4-2 Calculated impedance ($R_e$, $R_{ct}$) of 10VTS-620-HP and 10VTS-670-HP based on EIS equivalent circuit model. ..... 31
Table 5-1 The fraction of C=N-C, C-N-H of 10SiZC and 10SiZGC before and after cycling, which were obtained from the deconvoluted N 1s XPS spectra shown in Fig. 5-9b. ..... 40
Table 5-2 The fraction of Si, $SiO_2$ of 10SiZC and 10SiZGC before and after cycling, which were obtained from the deconvoluted Si2p XPS spectra shown in Fig. 5-9c. 41

# CHAPTER 1. INTRODUCTION

## 1.1. BACKGROUND AND CHALLENGES

With the continued development of society, the consumption of fossil fuels has increased dramatically, leading to global warming and environmental pollution. To achieve the goal of sustainable development, renewable energy technologies, such as wind energy and solar cells, are expanding rapidly. However, compared to traditional fossil fuels, these new energy sources are inherently intermittent, which results in an urgent need to develop large-scale and low-cost energy storage technologies to fully utilize renewable energy [1-3].

Batteries, which convert electrical energy into electrochemical energy or vice-versa, are one of the most important energy storage technologies in mobile devices. Among them, lithium-ion batteries (LIBs) have attracted worldwide attention due to their high energy density, long lifespan, and environmental friendliness. They are supporting modern society with lightweight power from portable electronics, such as smartphones, laptops, to electric vehicles (EVs). In 1970, Whittingham proposed the first LIB model, and then in 1981, Jhon Goodenough and Kaichi Mizushima, established a rechargeable cell by using lithium cobalt oxide ($LiCoO_2$) and lithium metal as cathode and anode, respectively. However, the formation of lithium dendrites of the anode during charging hinders its application. It was not until 1990, Sony Corporation released the first commercial LIB with $LiCoO_2$ as cathode and graphite as anode [1, 2]. As shown in Fig. 1-1, besides the two electrodes, a practical LIB uses organic solvent containing $Li^+$ ($LiPF_6$) as the electrolyte. The electrolyte acts as a guard, allowing only lithium ions to pass through. When connecting a power source, the positive side of the power source attracts electrons from the cathode. These electrons flow through the external circuit and reach the graphite layer as they cannot pass through the separator and electrolyte. Meanwhile, the lithium ions migrate from the cathode side through the electrolyte to the graphite layer space. Once the graphite is saturated with lithium ions, the cell is fully charged. As soon as the power source is disconnected, and a load is connected, the lithium ions travel back to intercalate into the favorable state as a part of the metal oxide cathode. When the lithium ions move through the electrolyte, the electrons are forced to move via the load. This process is called discharge, and it converts chemical energy to electrical energy, which powers the device [4].

As science and technology have advanced, the gravimetric specific energy density of LIBs increased from approximately 90 Wh $kg^{-1}$ in the 1990s to over 250 Wh $kg^{-1}$ today [5], mainly arising from the development of new cathode and anode materials. In detail, cathode materials such as $LiCoO_2$, $LiFePO_4$, $LiMn_2O_4$, $LiNi_xCo_yMn_{1-x-y}O_2$, and anode materials like carbonaceous materials, and Si/SiO-C composites appeared successively, improving the electrochemical performances of commercial LIBs [6-8].

However, the fast-growing large-scale smart grids and electric vehicle markets require increasingly better storage solutions. According to a report from World Energy Resource, the net capacity of batteries in electric vehicles is predicted to be 250 GW by 2030, raising the demand for safer and higher energy density along with longer cycle life and lower cost LIBs [1].

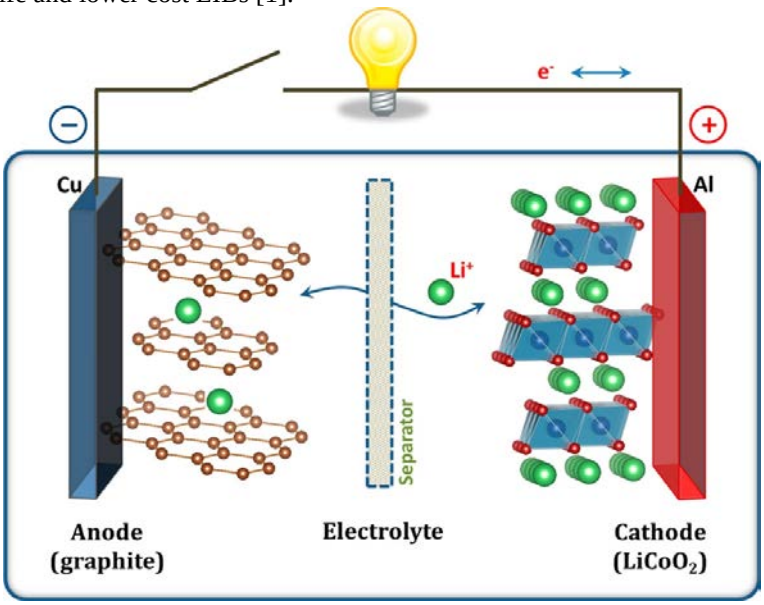


*Fig. 1-1 Schematic illustration of the Li-ion battery. The graphite anode and $LiCoO_2$ cathode are attached to copper and aluminum foils acting as the current collectors, respectively [4].*

Current efforts to improve the safety of batteries mainly focused on developing solid-state electrolytes to replace conventional organic liquid electrolytes. To date, inorganic glass-ceramic/glass-based solid electrolytes are one of the most promising candidates as they show the highest ionic conductivities with $10^{-2}$~$10^{-3}$ S $cm^{-1}$ [9-12]. As for lifting energy density, new anode materials, such as Si, Si@C composites and metal oxides with delicate nanostructures have been extensively investigated. Nonetheless, due to the complicated synthesis procedures, high cost and huge capacity loss during charging and discharging, those anode materials are still far from practical applications [13-17].

Glass materials, as a new branch of electrode materials, have attracted increasing attention from scientists owing to their unique disordered open network structure, lack of grain boundaries, large free volume, etc. [18-20]. These features could provide better cycling stability and higher specific capacity than crystalline counterparts[18, 21]. For example, semiconducting vanadium-tellurite glasses (VT), which exhibit superior cycling stability, i.e., almost no reduction in capacity for 5000 cycles [19], have emerged as promising anode materials for LIBs. Besides the open network, VT

glasses exhibit a strong crystallization tendency upon discharging/charging, leading to the formation of electrochemically active γ-$Li_3VO_4$ nanocrystals. The in-situ growth of nanocrystals in glass not only toughens the glass matrix, thereby increasing the cycling stability, but also provides more space/channels between the crystals and glass matrix to facilitate the transportation of $Li^+$.

Moreover, metal-organic frameworks (MOFs), which are three-dimensional networks composed of metal nodes and organic ligands, have been regarded as one of the most potential candidates to replace the current graphite anode for LIBs. This potential is mainly due to their high specific surface area, abundant active sites, and high porosity, which are beneficial for lithium transport and storage. In 2006, MOF-177 was first reported as anode materials for LIBs, showing a capacity of 400 mA h $g^{-1}$ during the first cycle but a low capacity of 105 mA h $g^{-1}$ in the second cycle. When MOFs are coated with graphene to obtain the MOF/graphene composite anodes, they deliver a reversible capacity up to ~1075 mA h $g^{-1}$ at a current density of 50 mA $g^{-1}$ and 400 mA h $g^{-1}$ at the current density of 100 mA $g^{-1}$ [22, 23]. In 2015, a new family of MOFs, i.e., MOF glass, was first discovered by Yue et al. A few years later, in 2022, MOF glass was first reported as an anode for LIBs, achieving a capacity of 306 mA h $g^{-1}$ after 1000 cycles at 2 A $g^{-1}$, twice that of the MOF crystal [20, 24-27].

In addition to displaying better electrochemical performances than their crystalline counterparts, glass materials pose many other advantages, i.e., tunable composition, simple preparation process, low cost, etc., which are expected to be mass-produced. Furthermore, considering that the best lithium solid-state electrolytes are glass/glass-ceramics, and the interfacial stability between the glassy solid-state electrolyte and the traditional electrode faces a big challenge due to poor compatibility at the interface [11]. It can be anticipated that a glassy electrode could provide better interfacial compatibility with the glassy electrolyte and thus minimize interfacial polarization of the cell.

However, glass anodes still face some challenges, including poor electronic conductivity and low reversible capacity. Furthermore, the lithium storage mechanism of glasses needs to be further understood, and the composition-structure-performance relationship of glasses is still unclear. Solving these problems will help design and develop appropriate glass-based anodes for better LIBs.

## 1.2. OBJECTIVES

The overall goal of this PhD project is to investigate the potential of glasses as anode materials for LIBs, from aspects of specific capacity, cycling stability and structure-performance relationship.

The specific capacity, which is proportional to energy density, can be determined by the amount of lithium that could be accommodated per unit mass/volume of active

material. The cycling stability is the capacity retention rate after a certain number of charge/discharge cycles. These two properties are vital criteria for evaluating the lithium storage performance

The details of this project are summarized below:
1. Explore a method to combine silicon (Si), which exhibits a high theoretical specific capacity (>4000 mA h $g^{-1}$), with inorganic glasses (VT glass) to improve the specific capacity of glasses for lithium storage.
2. Develop a facile method to combine silicon with MOF glasses to improve their capacities and cycling stabilities during charge-discharge processes.
3. Study the composition-structure-process-performance relations of Si-glass composite.
4. Investigate the lithiation/delithiation mechanism of batteries in glassy materials.
5. Develop the potential of glass-based composites as anode materials for LIBs.

## 1.3. THESIS CONTENT

The experiment works of this thesis were conducted at Aalborg University, Qilu University of Technology, Fuzhou University and Wuhan University of Technology. This thesis consists of an overview followed by three scientific papers. The three papers correspond to Chapters 3-5, constituted the main body of the thesis, and will be referred to by their roman numerals.

I. **Yan, J.**, Zhao, T., Shi, N., Zhan, H., Ren, J., Zhang, Y., & Yue, Y., Impact of silicon doping on the structure and crystallization of a vanadium-tellurite glass. Journal of Non-Crystalline Solids, 589, 121651 (2022).

II. **Yan, J.**, Gao, C., Qi, S., Jiang, Z., Jensen, L. R., Zhuang, Y., Zhan, H., Zhang, Y., & Yue, Y., High-performance lithium-ion battery anode based on melt-quenched Si@ZIF composite. Nano Energy, 103, 107779 (2022).

III. **Yan, J.**, Li, X., Shi N., Ren X, Zhou, H., Tao, H., Ren, J., Qiao, A., Zhang, Y., & Yue, Y., Optimizing vanadium-tellurite glass/Si composite as a superior anode for Li-ion batteries by hot pressing (To be submitted).

# CHAPTER 2. EXPERIMENTAL SECTIONS

This chapter presents synthesis methods and characterization techniques of VT/MOF glasses and glass-based composites, i.e., Si/VT glass composites, and Si@MOF glass composites.

## 2.1. SYNTHESIS

All the chemical reagents used for the preparation/synthesis were purchased from the Aladdin or Sigma corporations and used without further modification unless specified. All samples were prepared by the authors in this thesis with assistance from other co-authors.

### 2.1.1. VANADIUM-TELLURITE GLASSES (VT)

The $50V_2O_5$-$50TeO_2$ (in mol. %) glass sample was prepared via the melt-quenching method [18, 19]. In detail, the oxides ($V_2O_5$ and $TeO_2$) were mixed to get a homogenous batch. Then the batch was melted at 800°C for 0.5 h followed by casting onto a brass plate. After becoming solid, the glass was transferred into a furnace and annealed for 2 h at the glass-transition temperature ($T_g$). The $50V_2O_5$-$50TeO_2$ glass powder (VT) with a narrow size distribution between 5 ~ 10 μm was obtained by crushing and sieving the annealing sample.

### 2.1.2. SI/VT COMPOSITES

As for the Si/VT composites, the preparation processes were as follows: commercial nano-silicon (Si) nanoparticles (about 20-60 nm) were doped in the VT glass powder, and then mixed evenly, which is referred to as VTS. In Chapter 3, VTSs with 10 wt.% Si were heat-treated by the conventional method, i.e., heating VTS at 10 K/min to different temperatures under argon followed by cooling to room temperature. In Chapter 4, VTSs with 10 wt.% Si were heated to different temperatures at 10 K/min in vacuum with a pressure of 100 MPa and kept for 30 minutes before cooling, which is called hot-pressing sintering. In addition, VTSs with different fraction of Si, i.e., 10%, 20%, 30%, 40%, were prepared by hot pressing at one temperature (620K). For comparison, VTS containing 10 wt.% Si were prepared by the same heating process as the hot-pressing samples except that it was not pressurized.

### 2.1.3. COBALT-ZIF-62 CRYSTALS/GLASSES

Zeolitic imidazolate framework (ZIF) is a subset of MOF materials. Cobalt-ZIF-62 crystals with the composition of $Co(imidazole)_{1.75}(benzimidazole)_{0.25}$ were synthesized based on a solvothermal method [27-29]. In detail, imidazole (Im, 11.55 mmol, 785.4 mg), benzimidazole (BIm, 1.66 mmol, 196 mg) and Cobalt acetate tetrahydrate (4 mmol, 996 mg) were dissolved in 90 mL N,N-dimethylformamide (DMF) and stirred for 0.5 h. Then, the solution was transferred into the autoclave and heated at 130°C for 48 h. After cooling, the purple product was separated by centrifugation and dried under vacuum at 120°C overnight. To obtain cobalt-ZIF-62 glass, the ZIF-62 crystals were heated at 10 °C $min^{-1}$ in argon to 450°C and calcined at this temperature for 5 minutes then cooled down naturally to room temperature.

### 2.1.4. SI@ZIF-62 COMPOSITES

Si@ZIF-62 composite (SiZC) was prepared via a reflux method. This method involves heating the chemical reaction for a period at a certain temperature, while continually cooling the solvent vapor back into liquid form. In detail, imidazole (Im, 11.55 mmol, 785.4 mg), benzimidazole (BIm, 1.66 mmol, 196 mg), $C_4H_6CoO_4 \cdot 4H_2O$ (4 mmol, 996 mg), and Si nanoparticles with different amounts, i.e., 50-mg, 100-mg, 150-mg Si, account for about 5%, 10%, 15% of the final product by weight, respectively, were added into 90 mL N,N-dimethylformamide (DMF). Then the solution was heated at 130°C for 48 h while refluxing and stirring. After cooling, the SiZC was obtained by centrifugation and vacuum drying. Then, the SiZC was melt-quenched at 450°C for 5 minutes in argon and thus Si@ZIF-62-glass composite (SiZGC) was obtained. The samples are named according to the mass percentage of Si in the composite. For example, 10SiZGC refers to the Si@ZIF-glass composite containing 10 wt.% Si.

## 2.2. CHARACTERIZATION METHODS

The author performed most of the experiments and analyzed almost all results in this thesis except part of the solid-state nuclear magnetic resonance (NMR) results. A co-author contribution is presented in the relevant sections if the experiments or characterizations were not conducted by the author independently.

### 2.2.1. X-RAY DIFFRACTION (XRD)

XRD patterns of fine-grinded samples were collected on a PANalytical diffractometer X-ray using Cu *K*α ($\lambda$ = 1.5406 Å) radiation during the 2$\theta$ range of 5–70° with a step size of 0.013°. The simulated XRD patterns of MOF were obtained from Software Mercury 3.8 with CIF file of corresponding MOF. Crystalline phases were identified by using the X'pert HighScore Plus software.

### 2.2.2. DIFFERENTIAL SCANNING CALORIMETRY (DSC)

The characteristic temperatures of glassy materials, such as glass-transition temperatures, crystallization onset temperatures, melting temperatures, etc., were collected by the differential scanning calorimeter (DSC) (Jupiter 449C, Netzsch) in Aalborg University. Platinum crucibles were used for both samples and the references. The sample mass was usually about 20 mg. All samples were scanned from 40°C to target temperatures at 10 °C $min^{-1}$ in argon and then cooled down at the same rate. Before each test, baselines were collected with the same temperature range, scanning rates, and atmosphere. During the process of recording DSC curves, the thermogravimetric (TG) curves were collected simultaneously.

### 2.2.3. RAMAN SPECTROSCOPY

Raman spectra were obtained via Renishaw In-Via Raman microscopic with an $Ar^+$ laser ($\lambda$ = 532 nm) at 50 × aperture in Aalborg University. To avoid burning the sample, the power was limited to 0.1 W and was used to record the spectra within the range of 200-2000 $cm^{-1}$. All samples were tested three times for error reduction. Raman spectra were collected with the help of Dr. L.R. Jensen from the Department of Materials and Production, AAU.

### 2.2.4. ATTENUATED TOTAL REFLECTION FOURIER TRANSFORM INFRARED SPECTROSCOPY (ATR-FTIR)

Attenuated Total Reflection Fourier transform infrared (ATR-FTIR) spectra measurements were conducted on a Bruker TENSOR II FTIR spectrometer in Aalborg University with Platinum ATR Accessory at room temperature in the range of 400–2000 $cm^{-1}$. For each test, a baseline was measured first, and then sample powders were directly placed on the holder for data collection. All samples were tested three times to reduce error.

### 2.2.5. X-RAY PHOTOELECTRON SPECTROSCOPY (XPS)

To investigate the surface chemistry of samples, X-ray photoelectron spectroscopy (XPS) was performed using an ESCALAB 250Xi spectrometer (ThermoFisher Scientific, USA) with nonmonochromatic Al Ka X-ray (1486.6 eV) at pass energy of 50 eV from Wuhan University of Technology with the help of Professor Ang Qiao. The peaks were deconvoluted using the software Avantage.

### 2.2.6. SOLID-STATE NUCLEAR MAGNETIC RESONANCE (NMR)

Solid-state NMR measurement was conducted with the help of Professor Jinjun Ren, Dr. Tongyao Zhao, and Nian Shi from the Shanghai Institute of Optics and Fine Mechanics, Chinese Academy of Sciences. $^{51}V$, $^{125}Te$, and $^{29}Si$ spectra of vanadium-

tellurite glasses (VT) and Si@vanadium-tellurite glass (VTS) were collected. $^{29}Si$ NMR spectra were measured at a spinning rate of 6.0 kHz with relaxation delays of 200 s. The chemical shift is referenced to Tetrakis (tetramethyl) silicate silane (= -9.7 ppm). $^{51}V$ Hahn echo NMR experiments were performed at a pulse length of 2.4 μs. $^{125}Te$ static wideband uniform-rate smooth truncation QCPMG (WURST-QCPMG) NMR spectra were obtained using the WURST-80 pulse sequence and an 8-step phase cycle with 50-μs excitation and refocusing pulses.

### 2.2.7. SCANNING ELECTRON MICROSCOPY (SEM)

The morphologies and elements distributions of samples were analyzed using field-emission scanning electron microscopy (FE-SEM) (Supra-55, Zeiss Inc.) along with X-ray energy dispersive spectroscopy (EDS) (X-Max, OXFORD Instruments Inc.) from Fuzhou University and Wuhan University of Technology. All samples were vacuum dried at 120°C and then pasted onto the conductive gel before testing

### 2.2.8. TRANSMISSION ELECTRON MICROSCOPY (TEM)

Transmission Electron Microscopy (TEM) images of samples were collected from a Tecnai Talos F200i and elemental mapping analysis was conducted via TEM energy-dispersive X-ray spectroscopy (HAADF-STEM-EDX) in Fuzhou University with the help of Yaxuan Zhuang and Dr. Zhenhuan Zheng. Powder samples were dispersed in ethanol and ultrasonicated for 30 min, and then drop cast onto copper mesh before TEM measurements.

## 2.3. ELECTROCHEMICAL METHODS

The electrochemical performances of the obtained samples were evaluated by coin cells using lithium foil (diameter of 10.0 mm) as the counter/reference electrode. A slurry consisting of 70 wt.% active materials (the glass-based composites), 20 wt.% acetylene black, and 10 wt.% polyvinylidene difluorides (PVDF) were mixed evenly in N-methyl-2-pyrrolidone (NMP) and then pasted onto a copper foil current collector and dried at 110°C in a vacuum oven for 12 h to get working electrodes. The loading amount of active materials was 1~2 mg. The composition of electrolyte was: 1 M $LiPF_6$ dissolved in ethylene carbonate (EC)/diethyl carbonate (DEC)/dimethyl carbonate (DMC) (1:1:1 vol%). The separator was a Celgard 2325 membrane (diameter of 19.0 mm). The cells were assembled in an argon-filled glovebox with both the moisture and the oxygen content below 0.1 ppm and then tested at 25°C. Some of the electrochemical measurements were conducted with the help of Zhenjing Jiang, Shibin Qi and Xiangyu Li from Qilu University of Technology. All electrochemical measurements were repeated with different batches of samples to confirm the reproducibility of their performances.

### 2.3.1. CYCLIC VOLTAMMETRY

Cyclic Voltammetry (CV) curves of samples were obtained to study the lithium storage mechanism in active materials at a scan rate of 0.1 mV $s^{-1}$ in the voltage range from 0.01 to 3 V on a CHI 760e electrochemical working station. For Si@ZIF samples, both the first three cycles and three cycles after 500 charging/discharging cycles were recorded.

### 2.3.2. GALVANOSTATIC CHARGE-DISCHARGE

Galvanostatic charge-discharge (GCD) measurements were conducted to evaluate the specific capacity, cycling stability and rate capability of glass-based materials for LIBs. All samples were measured on a Land battery test system (CT2001A) within the voltage range of 0.01-3V with different current densities for different cycles. The specific capacities of materials were calculated based on their weight and the Coulombic efficiencies of charge-discharge processes were also collected. Besides, the GCD voltage profiles were also obtained to study the lithium insertion/extraction mechanism of electrode materials.

### 2.3.3. ELECTROCHEMICAL IMPEDANCE SPECTROSCOPY

Electrochemical Impedance Spectroscopy (EIS) measurements were performed on CHI 760e electrochemical workstation in the frequency range of 0.1 Hz–100 kHz with an amplitude of 10 mV. By constructing an equivalent circuit and fitting the impedance data, the resistance, i.e., ohmic resistance ($R_e$), solid electrolyte interface resistance ($R_s$) and charge transfer resistance ($R_{ct}$), capacitance (CPE) and diffusion impedance ($Z_w$) of the electrode systems could be obtained.

The line in the low-frequency region corresponds to the diffusion impedance ($Z_w$), which is associated with the diffusion coefficient of $Li^+$ in the electrode material. Warburg factor ($\sigma$) can be determined from the linear relation between impedance $Z'$ and the reciprocal square root of the angular frequency $\omega$. A larger value of $\sigma$ indicates a lower $Li^+$ diffusion coefficient.

# CHAPTER 3. STRUCTRUE AND CRYSTALLIZATION OF VT GLASS AND SI/VT-GLASS COMPOSITES

Since the performances of materials rely on their compositions, structures, process etc., it is important to understand how these parameters affect the electrochemical performance of a material. In this Chapter (based on Paper I), silicon (Si) was added into a vanadium-tellurite glass (VT) and the mixture was heat-treated to different temperatures followed by cooling to room temperature to obtain Si/VT composites (VTSs), which are used as anode materials for lithium-ion batteries. The effects of Si doping on the structure, crystallization, and electrochemical performances of VT glass were studied.

The reasons why chose Si as the element to combine with glasses are as follows: First, it has a high theoretical specific capacity ($>$4000 mA h $g^{-1}$). Second, Si is non-toxic and is the second most abundant element in the earth's crust, exhibiting low average discharge potential vs. $Li^+/Li$ [30]. However, pure Si anode exhibits very poor cycling stability, i.e., capacity retention is only about 50 mA h $g^{-1}$ within 100 cycles [31, 32], due to its enormous volume changes (>300%) and pulverization upon lithiation/delithiation [33]. On the contrary, VT glasses exhibit superior cycling stability due to their unique open structure (more details are shown in Section 1.1) but relatively low specific capacity compared to Si [18, 19]. In addition, glasses show viscous flow above the glass transition temperature ($T_g$) and can act as 'binder' for bonding Si. It is anticipated that the combination of Si and glasses through heat-treatment could pose synergetic effects to achieve better electrochemical performances.

## 3.1. CHARACTERIZATIONS OF VT AND SI/VT COMPOSITES

### 3.1.1. PHASE AND THERMODYNAMIC ANALYSES OF VT AND VTS

10 wt.% Si and 90 wt.% vanadium tellurite glass (VT) powders were mixed evenly, referred to as VTS in this Chapter. Fig. 3-1 shows the DSC upscan curves for both VT and VTS. For these samples, the glass transition temperature ($T_g$ =509K) and crystallization onset temperatures ($T_{c1}$=563K, $T_{c2}$=602K) are the same, while crystallization temperature ($T_{c3}$) at 673K only shows in VT. In addition, the melting temperature (around 760K) of VT glass becomes weaker and shifts to a lower temperature when Si is introduced. These results indicate that doping Si into VT does not change the glass transition but suppresses the crystallization behavior of the glass. The latter phenomenon is anomalous, to the best of my knowledge, doping Si

generally provides more heteronuclear sites, thereby promoting the nucleation and crystallization of VTS compared with pristine VT glass. The opposite results prompted us to further investigate the crystallization behavior of VT and VTS.

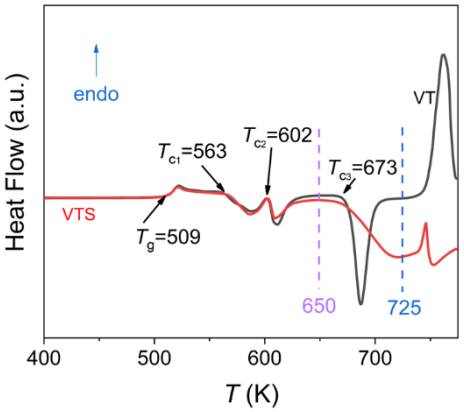


*Fig. 3-1 DSC upscan curves of both VT and VTS, which are obtained at 10 K/min in argon. The characteristic temperatures such as glass transition ($T_g$) and crystallization onset temperatures ($T_{c1}$, $T_{c2}$, and $T_{c3}$) are denoted in the curves.*

Since the crystallization behaviors of VT and VTS are almost the same up to 650K but very different in the temperature range of 673~725K, we conducted several DSC upscans on VT and VTS to 650K and 725K. Fig. 3-2a shows the DSC curves for VT and VTS upscanned to 650K for three times. Fig. 3-2b shows the curves for these samples upscanned to 650K for the first time followed by to 725K for the second and third times. In both Figs. 3-2a and b, the $T_g$s of both VT and VTS shift to higher temperatures from the first to the 2$^{nd}$ upscan due to the crystallization in the first upscan. In the third upscan, $T_g$s remain constant in Fig. 3-2a but disappear in Fig. 3-2b, suggesting that during the second DSC upscan to 725K, the glasses are fully transformed into crystal phase. In addition, for each upscan, VT and VTS show the same $T_g$ value, indicating that the remaining glass phase in VT and VTS after crystallization might have the same composition. New crystallization peaks with onset temperatures of $T_{c3}$ and $T_{c4}$ are observed for VT but not for VTS in Fig. 3-2a. Moreover, $T_{c3}$ (647K) for VT shifts to a higher temperature (662K) for VTS in Fig. 3b. These results verify that the crystallization in VT glass was suppressed by introducing nano-Si.

Figs. 3-3a, 3b show XRD patterns of VT and VTS after each DSC upscan to 650K. According to the number of the DSC upscans, samples are named as VT/VTS-650, VT/VTS-650-2, VT/VTS-650-3, respectively. Clearly, only $V_2O_5$ crystals were precipitated from both VT-650 and VTS-650 samples, as the crystalline Si already exists in VTS.

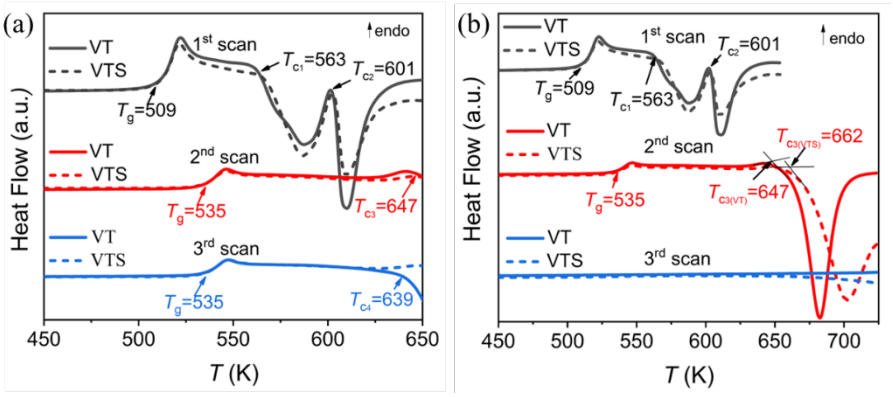


*Fig. 3-2 DSC upscan curves of both VT and VTS, which are obtained at 10 K/min in argon. (a) DSC upscan to 650K for three times. (b) DSC upscan to 650K for the first time and then to 725K for the second and third times. The characteristic temperatures such as glass transition ($T_g$) and crystallization onset temperatures ($T_{c1}$, $T_{c2}$, $T_{c3}$ and $T_{c4}$) are denoted.*

However, samples VT-650-2 and VT-650-3 show sharp diffraction peaks corresponding to $Te_2V_2O_9$ crystals besides $V_2O_5$ peaks, while samples VTS-650-2 and VTS-650-3 still only exhibit peaks associated with $V_2O_5$ and Si. This suggests that by introducing nano-Si into VT glass, the crystallization of $Te_2V_2O_9$ has been suppressed. In addition, this finding also indicates that the compositions of the remaining glass matrices in VT and VTS are different after the 2nd and 3rd DSC upscan, even though these two samples have the same $T_g$ in each upscan curve.

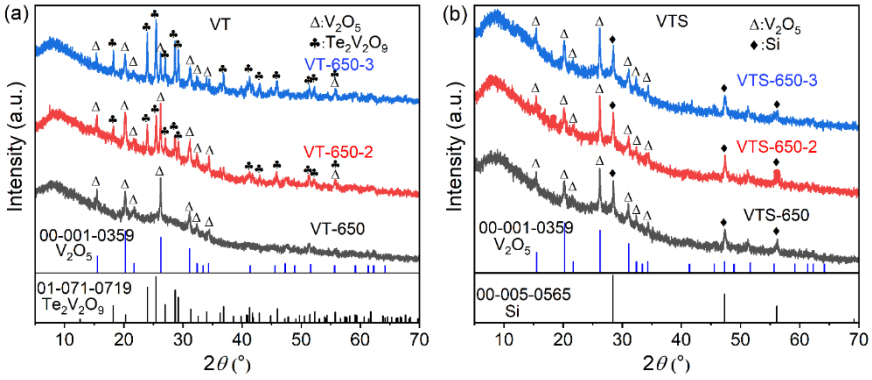


*Fig. 3-3 XRD patterns of (a) VT and (b) VTS after the first, second and third DSC upscans to 650 K at 10 K/min in argon.*

Fig. 3-4 shows the XRD patterns of VT and VTS after two DSC upscans, i.e., first to 650K and then to 725K, which are referred to as VT-650-725 and VTS-650-725, respectively. Clearly, VT-650-725 shows two kinds of crystalline phases, i.e., $V_2O_5$ and $Te_2V_2O_9$, while VTS-650-725 shows four types of crystals, i.e., $V_2O_5$, $Te_2V_2O_9$,

$TeVO_4$, and Si. This indicates that although the crystallization of $Te_2V_2O_9$ in VTS is suppressed, a new crystalline phase ($TeVO_4$) is precipitated during heating VTS to 725K. The formation of $TeVO_4$ could arise from the reaction between VT glass and nano-Si.

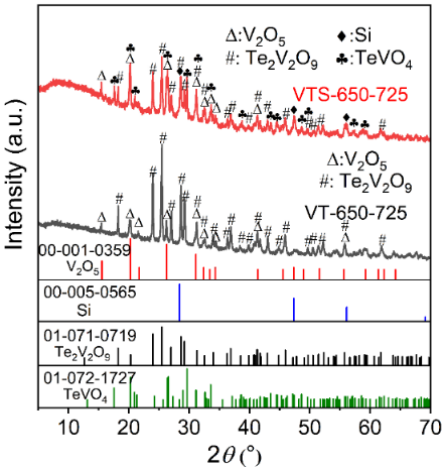


*Fig. 3-4 XRD patterns of VT and VTS after two DSC upscans at 10 K/min in argon. The first upscan was carried out to 650K and the second one was to 725K, which are referred to as VT-650-725 and VTS-650-725, respectively.*

## 3.1.2. STRUCTURAL ANALYSIS OF VT AND VTS

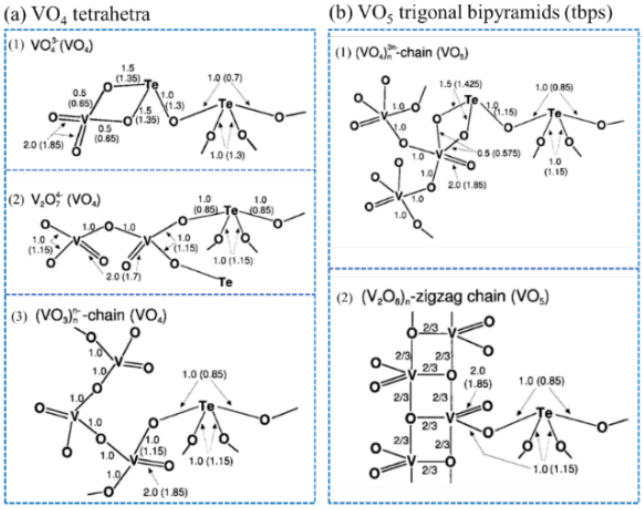


*Fig. 3-5 Possible linkage modes between (a) $VO_4$ tetrahedra, (b) $VO_5$ trigonal bipyramids (tbps) with $TeO_3$ or $TeO_4$ in vanadium-tellurite glasses [34].*

Unlike traditional inorganic glasses with 3D tetrahedral network, the structure of VT contains $VO_4$ tetrahedra and $VO_5$ trigonal bipyramids(tbps) [34]. Fig. 3-5 shows three possible tetrahedra of $VO_4$, including types of $VO_4^{3-}$, $V_2V_7^{4-}$, and $(VO_3)_n^{n-}$-chain and two possible tbps of $VO_5$, i.e., $(VO_4)_n^{3n-}$-chain and $(V_2O_8)_n$-zigzag chain. Clearly, $VO_4$ and $VO_5$ units can be corner-sharing and edge-sharing with $TeO_3$ or $TeO_4$ units.

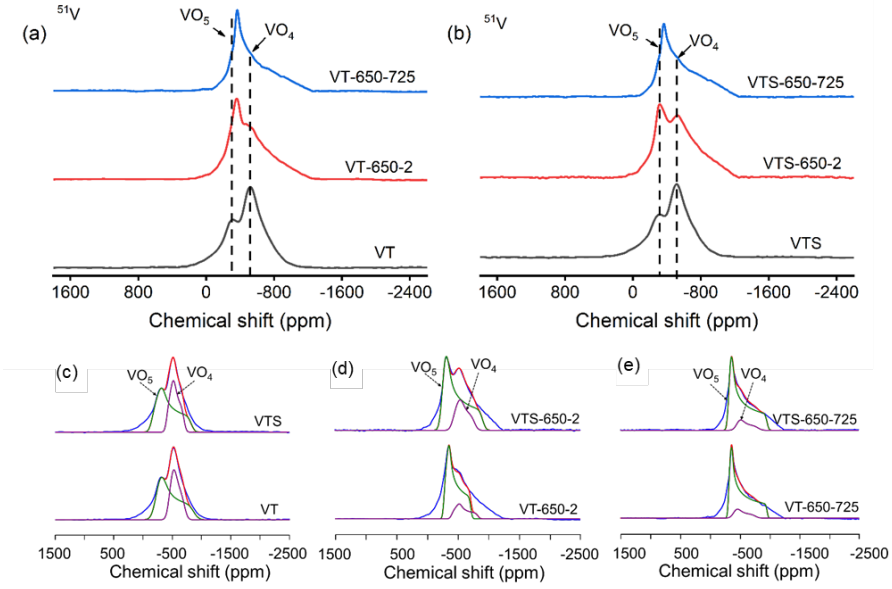


*Fig. 3-6 $^{51}V$ NMR spectra of (a) VT and (b) VTS samples before and after two different DSC upscans at 10 K/min in argon. For VT/VTS-650-2, samples were upscanned to 650K twice, while for VT/VTS-650-725, samples were upscanned to 650K first and then to 725K. The deconvolution of $^{51}V$ NMR spectra for VT/VTS (c), VT/VTS-650-2 (d), and VT/VTS-650-725 (e). Purple and green curves represent the $VO_4$ and $VO_5$ contributions, respectively.*

To further verify the inhibition effect of crystallization in VTS and probe the structural evolution in VT and VTS samples upon different heating processes, NMR characterizations of VT and VTS were performed. Figs. 3-6a, b shows the $^{51}V$ NMR spectra of VT, VTS, VT/VTS-650-2, and VT/VTS-650-725. The spectrum of each sample can be deconvoluted into two peaks (purple and green curves), corresponding to $VO_4$ and $VO_5$, respectively (Figs. 3-6c, d, e). For each sample, the fractions of $VO_4$ and $VO_5$ are shown in Table 3-1. Clearly, as the DSC maximum upscanning temperature ($T_{max}$) rises, the $VO_5/VO_4$ ratio increases for both VT and VTS. In addition, the VT-650-2 shows higher $VO_5/VO_4$ ratio than VTS-650-2. This is due to that the majority of vanadium of $Te_2V_2O_9$ and $V_2O_5$ crystals exist in $VO_5$ units [34-40] and both $Te_2V_2O_9$ and $V_2O_5$ are precipitated in VT-650-2, but only $V_2O_5$ forms in VTS-650-2. The lower $VO_5/VO_4$ ratio in VTS-650-2 compared with that in VT-650-

2 further confirms the inhibiting effects of Si on the crystallization of VT glass. When $T_{max}$ reaches 725K, VT/VTS-650-725 exhibit the same $VO_5/VO_4$ ratio. This is because the two glass samples are fully transformed into crystals, verified by the DSC results in Fig. 3-2b. It is worth noting that although a new $TeVO_4$ phase is precipitated in VTS-650-725 besides $V_2O_5$ and $Te_2V_2O_9$, the majority of vanadium in $TeVO_4$ exists in $VO_5$ [35, 36, 38, 39].

*Table 3-1 The fraction of $VO_5$ and $VO_4$, which were obtained from the deconvoluted $^{51}V$ NMR spectra shown in Fig. 3-6.*

| Samples | $VO_5$ (%) | $VO_4$ (%) | $VO_5/VO_4$ | Samples | $VO_5$ (%) | $VO_4$ (%) | $VO_5/VO_4$ |
|---|---|---|---|---|---|---|---|
| VT | 62.2 | 37.8 | 1.65 | VTS | 62.3 | 37.7 | 1.65 |
| VT-650-2 | 80.9 | 19.1 | 4.24 | VTS-650-2 | 75.8 | 24.2 | 3.13 |
| VT-650-725 | 88.1 | 11.9 | 7.40 | VTS-650-725 | 88.2 | 11.8 | 7.47 |

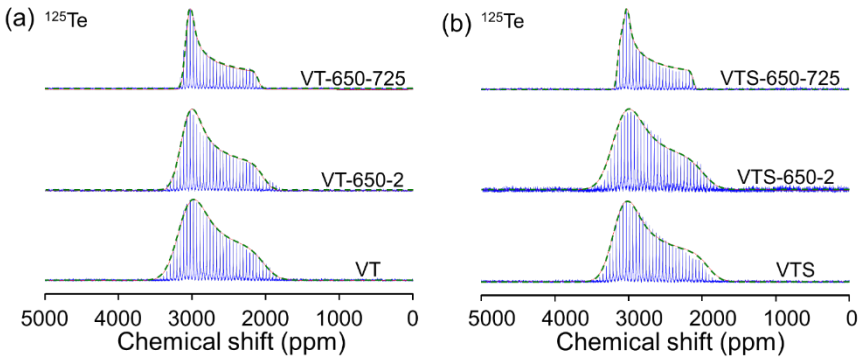


*Fig. 3-7. $^{125}Te$ NMR spectra of (a) VT and (b) VTS samples before and after two different DSC upscans at 10 K/min in argon. For VT/VTS-650-2, samples were upscanned to 650K twice, while for VT/VTS-650-725, samples were upscanned to 650K first and then to 725K. Dashed lines: the fitting curves.*

Fig. 3-7 shows the $^{125}Te$ NMR spectra of VT/VTS, VT/VTS-650-2, and VT/VTS-650-725. Each $^{125}Te$ spectrum can be fitted by one unsymmetric peak, ascribing to 3-coordinated Te. As $T_{max}$ rises, the peak shape becomes sharper, indicating the glass-to-crystal transformation [34]. In addition, VT-650-2 shows a sharper peak than VTS-650-2, suggesting that crystallization of $Te_2V_2O_9$ has been suppressed in VTS.

To reveal the mechanism of the suppressing crystallization in VTS, XPS measurements were conducted on VTS and VTS-650. As shown in Fig. 3-8a, each Si 2p XPS curve can be deconvoluted into two peaks, i.e., 99.5 and 103.1 eV corresponding to Si and $SiO_2$, respectively [41]. More details are shown in Table 3-2. Clearly, the fractions of Si in VTS and VTS-650 are 61.1 and 55.6%, respectively,

implying the oxidation of Si during heat-treatment. Fig. 3-8b shows the V 2p spectra, in which VTS can be deconvoluted into four peaks while VTS-650 can be deconvoluted into five peaks. Peaks at 532.7, 530.6, 524.9, and 517.5eV are ascribed to V-OH, V-O, V $2p_{1/2}$, and V $2p_{3/2}$, respectively. For VTS, peak at 517.5 eV becomes wider after heat-treatment, and the wider peak can be deconvoluted into two peaks, i.e., 517.5 and 516.4 eV, corresponding to $V^{5+}$ and $V^{4+}$, respectively. This indicates a redox reaction occurred between Si and VT during the heating process [42, 43].

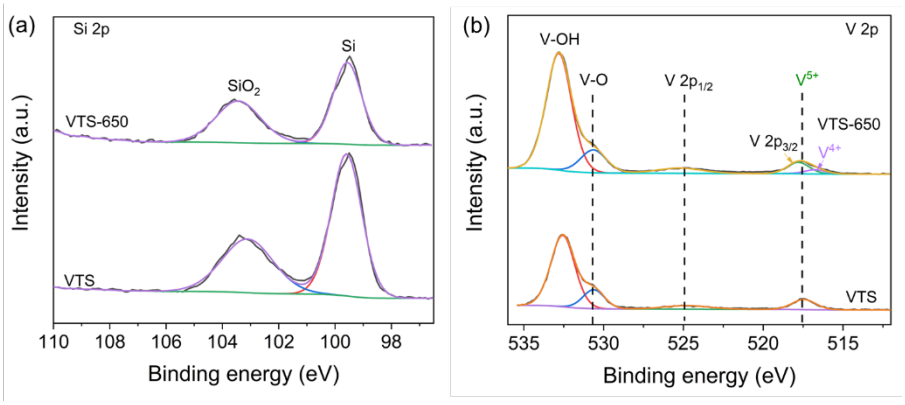


*Fig. 3-8 XPS high-resolution of Si 2p(a) and V 2p (b) spectra for VTS and VTS-650.*

*Table 3-2 The fraction of Si, $SiO_2$ of VTS and VTS-650, which were obtained from the deconvoluted Si 2p XPS spectra shown in Fig. 3-8a.*

| Samples \ Chemical state | Si (%) | $SiO_2$ (%) | Ratio ($Si/SiO_2$) |
|---|---|---|---|
| VTS | 61.1 | 38.9 | 1.6 |
| VTS-650 | 55.6 | 44.4 | 1.2 |

To further study the reaction between Si and VT during heating, systematical NMR analyses were performed on the VTS with different $T_{max}$. As shown in Fig. 3-9a, for $^{29}Si$ NMR spectra, each spectrum can be deconvoluted into three peaks, i.e., at −110 ppm, −85 ppm, and ~ −80 ppm, corresponding to $Q^4$ in amorphous $SiO_2$, amorphous Si (A-Si), and crystalline Si (C-Si) [44], respectively, where Q represents tetrahedron, and 4 is the number of bridging oxygen [45]. With an increase of the $T_{max}$, the peak at ~ −80 ppm becomes weaker, and the peak at ~ −85 ppm decreases and disappears at $1.6T_g$ (815K). In contrast, the peak at ~ −110 ppm increases as the $T_{max}$ rises. These imply the transformation of nano-Si into amorphous $SiO_2$ during the heating process. Fig. 3-9b shows the $^{51}V$ spectrum of VTS after DSC scanning to different temperatures, i.e., $T_g$=509 K, $1.1T_g$ =560 K, $1.2T_g$ =610 K, $1.3T_g$≈650 K, and $1.4T_g$ ≈725 K. Fig. 3-9c shows the deconvolution results, and each spectrum can be deconvoluted into two components, i.e., the purple curve corresponds to $[VO_4]$, while

the green curve is ascribed to [$VO_5$]. Obviously, as $T_{max}$ rises, the fraction of [$VO_5$] increases, while that of [$VO_4$] decreases.

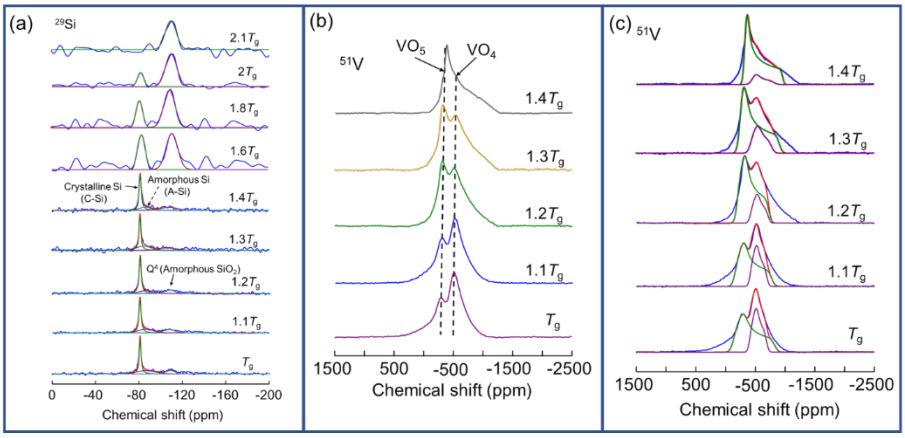


*Fig. 3-9 (a) $^{29}$Si NMR spectra of VTS upscanned in DSC to $T_g$ ~2.1$T_g$ at 10 K/min in argon (b) $^{51}$V NMR spectra of VTS upscanned in DSC to $T_g$~1.4$T_g$ at 10 K/min in argon (c) deconvolution of $^{51}$V NMR spectra shown in (b).*

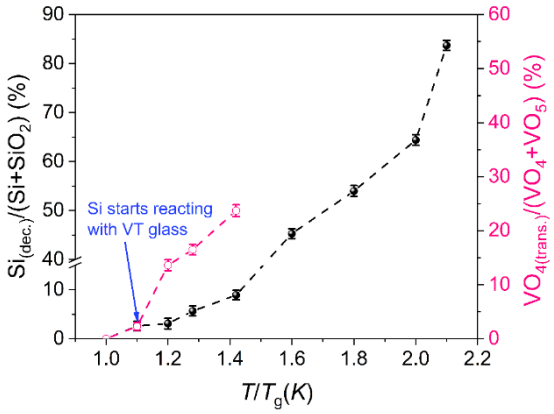


*Fig. 3-10 The dependences of both $Si_{(dec.)}/(Si+SiO_2)$ and $VO_{4(trans.)}/((VO_4+VO_5)$ on the DSC $T_{max}$ for VTS samples. The $T/T_g$ represents the ratio of the $T_{max}$ to the glass transition temperature of VTS.*

Fig. 3-10 is a summary of the $^{29}$Si and $^{51}$V NMR results (Fig. 3-9). By integrating the areas of deconvoluted peaks, the fractions of Si, $SiO_2$, $VO_4$, and $VO_5$ can be determined. $Si_{(dec.)}$ and $VO_{4(trans.)}$ refer to the fractions of Si and $VO_4$ units, which have been oxidized to $Si^{4+}$ or transformed into $VO_5$ during heating. Obviously, as the $T_{max}$ increases, both the fractions of $Si_{(dec.)}$ and $VO_{4(trans.)}$ rise. In detail, when $T_{max}$ is higher

than 1.4$T_g$, the $Si_{(dec.)}/(Si+SiO_2)$ increases dramatically, suggesting that a violent reaction occurs between Si and VT glass. In contrast, the $VO_{4(trans.)}/(VO_4+VO_5)$ increases rapidly from 1.1$T_g$ to 1.4$T_g$. Since the coordination number of stable $V^{4+}$ can only be 5 or 6 while that of stable $V^{5+}$ can be 4, 5 and 6 [46], the increase of $VO_{4(trans.)}$ in VTS-1.1$T_g$ compared to VTS-$T_g$ could partially arise from the transition of $V^{5+}$ to $V^{4+}$. When the $T_{max}$ is above 1.1 $T_g$, the transition of $VO_4$ to $VO_5$ units is ascribed to both the reduction of $V^{5+}$ to $V^{4+}$ and the crystallization of $V_2O_5$, $Te_2V_2O_9$ and $TeVO_4$ (the valence of vanadium is +4). The changes in both $Si_{(dec.)}$ and $VO_{4(trans.)}$ imply that nano-Si starts to react with VT glass at 1.1$T_g$. Thus, the Si-to-$SiO_2$ conversion in VTS can be controlled by varying the heat-treatment temperature.

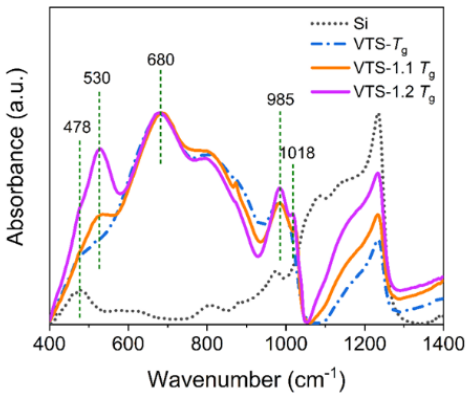


*Fig. 3-11. FTIR spectra of Si and VTS after upscanning in DSC to $T_g$, 1.1$T_g$ and 1.2$T_g$ at 10 K/min in argon.*

Fig. 3-11 shows the FTIR spectra of Si, VTS-$T_g$, VTS-1.1$T_g$, and VTS-1.2$T_g$. Peaks at 478cm$^{-1}$ and 1000~1250 cm$^{-1}$ correspond to Si–O vibrations [47-51], while peaks at 680, 985 and 1018 cm$^{-1}$ are assigned to O–Te–O or Te–O–Te vibrations [48], [$VO_5$] vibrations, and V=O vibrations in [$VO_5$], respectively [48, 50, 52-54]. Moreover, the broad peaks between 750 and 940 cm$^{-1}$ are mainly attributed to V–O–V, [$VO_4$], and [$VO_5$] vibrations[48, 50, 51]. A new peak at 530 cm$^{-1}$ associated with the V–O–V vibrations appears in spectra of VTS-1.1$T_g$ and -1.2$T_g$ samples [55-58]. Clearly, for the Si spectrum, a strong peak in the range of 1000~1250 cm$^{-1}$ is observed, suggesting the existence of $SiO_2$ in commercial nano-silicon particles. For the spectra of the other three samples, as the $T_{max}$ increases, the intensities of peaks at 530, 985, 1018, and 1050~1250 cm$^{-1}$ rise, indicating increases in the numbers of V–O–V bonds, [$VO_5$] units, and Si–O bonds. This is consistent with the NMR results (Fig. 3-9).

The above results reveal that although $SiO_2$ already exists in the pristine commercial nano-silicon particles, during heating process, Si gradually transformed into amorphous $SiO_2$, while $V^{5+}$ converted to $V^{4+}$, and hence a redox reaction should occur

between Si and VT. One possible reaction mechanism is shown in Fig. 3-12. In detail, during the heating process, Si-Si bonds break and each Si gains 4 oxygens from the [$VO_5$] units in VT glass, consequently, forming the tetrahedral [$SiO_4$] network and [$VO_4$] units. Meanwhile, Si reduces $V^{5+}$ in [$VO_5$] to $V^{4+}$ in [$VO_4$] (Fig. 3-12a). However, the [$VO_4$] units containing $V^{4+}$ are not stable [46], and they will rearrange themselves to form [$VO_5$]. Thus, during the heating process to 725K, [$VO_x$] units, which could be the [$VO_4$] units containing $V^{4+}/V^{5+}$ and [$VO_5$] units containing $V^{5+}$, evolve into the ordered structure. Simultaneously, part of [$VO_4$] units transform into [$VO_5$] units by sharing oxygen with other [$VO_4$] units [34] (Fig. 3-12b), generating new V–O–V bonds, verified by NMR and FTIR results.

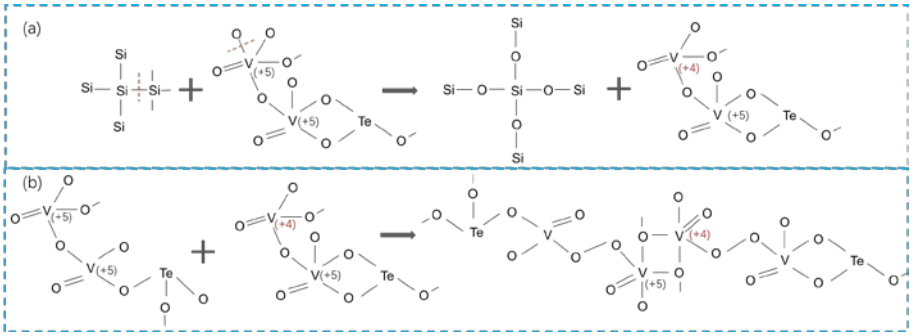


*Fig. 3-12. Schematic diagram of the reaction between Si and VT glass (a), and the evolution of [$VO_4$] to [$VO_5$] (b) when VTS was upscanned by DSC to 725K at 10 K/min in argon.*

Combined with the XRD results (Fig. 3-4), the redox reaction between Si and VT glass can be written as:

$$\frac{1}{2}Si + Te_2V_2O_9(glass) \rightarrow 2TeVO_4(glass) + \frac{1}{2}SiO_2(amorphous) \quad (3\text{-}1)$$

For VTS, during the first DSC upscan to 650K, the thermal energy is mainly used to overcome the energy barrier for $V_2O_5$ formation. When the second DSC upscan to 650K, the thermal energy is preferentially consumed for the above reaction (3-1) but not enough for the precipitation of new crystals. However, when the $T_{max}$ of the second upscan is increased to 725K, the thermal energy is sufficient to not only make this reaction occur but also overcome the energy barriers for both the precipitation of $Te_2V_2O_9$ and $TeVO_4$ crystals. This can be the origin of the suppression effects, i.e., crystallization was suppressed by doping Si in VT.

## 3.2. ELECTROCHEMICAL PERFORMANCES OF VT AND VTS

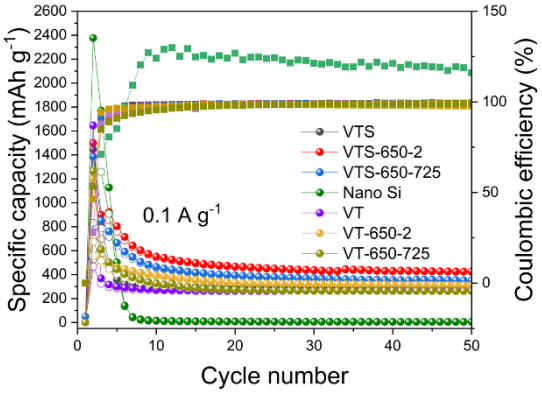


*Fig. 3-13. The cycling performance of anodes based on the VTS, VTS-650-2, VTS-650-725, Nano Si, VT, VT-650-2, VT-650-725 at 0.1 A $g^{-1}$ for 50 cycles.*

Fig. 3-13 shows the cycling performances of VTS, VTS-650-2, VTS-650-725, nano Si, VT, VT-650-2, VT-650-725, which exhibit capacities of 291, 424, 350, 5, 269, 305, and 261 mA h $g^{-1}$, respectively, at a current density of 0.1A $g^{-1}$ after 50 cycles. Clearly, the capacities of VTS after heat-treatment are higher than those of VT after heat-treatment, pristine VT and Si, suggesting VTS-650-2/VTS-650-725 exhibits a synergistic effect of VT and Si to some extent. In addition, the higher capacity of VTS after heat-treatment than that of pristine VTS indicates that the heating process can combine Si with VT and hence leverage the strengths of both materials. Moreover, VTS-650-725 based anode exhibits lower capacity than VTS-650-2, in which the former is fully crystallized while the latter is partially crystallized, verified by the DSC results. This could be due to that on the one hand, VTS-650-2 has more channels for $Li^+$ diffusion as it preserved both open networks of glass and space between crystals and glass matrix. On the other hand, the fraction of inactive $SiO_2$ in VTS-650-2 is lower than that of VTS-650-725, verified by the NMR results. Therefore, introducing Si into glass by heat-treatment and fabricating glass-ceramics, which contain both glass and crystals, could be an approach to enhance the capacity of both VT and VTS. However, the electrochemical performances of VTS need to be further improved. We will explore it further in the next chapter.

## 3.3. SUMMARY

In this chapter, we prepared a composite material composed of nano-Si and $V_2O_5$-$TeO_2$ glass (VT), which could be potentially applied as the anode material for LIBs. The nano-Si particles were evenly mixed with the VT glass, and then the mixture was subjected to different dynamic heat-treatment in argon by DSC. The as-prepared VTS exhibits higher capacity than their VT counterparts. In addition, the crystallization of VTS was suppressed compared with VT during the heating process. We clarified the origin of the suppression effects by using XPS, solid-state NMR, and FTIR

techniques. It was found that the introduction of nano Si in VT glass suppressed the formation of $Te_2V_2O_9$ crystals during heating to 650K but induce the precipitation of $TeVO_4$ during heating to 725K. This can be explained by the redox reaction between nano-Si and the VT glass. That is, when the VTS was heated to 650K, some thermal energy was consumed to overcome the energy barrier for the redox reaction (3-1), thereby making the precipitation of $Te_2V_2O_9$ crystals more difficult. When VTS was heated to 725K, the energy was sufficient for the precipitation of both $TeVO_4$ and $Te_2V_2O_9$ phases. This fundamental research on the structure evolution and crystallization behaviors of VTS upon heating contributes to the design of Si-glass composites for high-performance LIBs.

# CHAPTER 4. OPTIMIZING PERFORMANCES OF SI/VT-GLASS COMPOSITES BY HOT PRESSING

In Chapter 3, we have found that the Si/vanadium-tellurite glass composites (VTSs) can enhance the electrochemical performance compared with the pure Si and VT. However, the capacity of the VTS, which was obtained by the traditional heat treatment method (Chapter 3), still needs to be improved. Since the preparation process is one of the key factors affecting the material properties, in this chapter (based on Paper III), we fabricated Si/VT composites by the hot-pressing method (see Section 2.1.2 for details). The composition-process-structure-electrochemical performance relations were studied.

## 4.1. CHARACTERIZATIONS OF SI/VT COMPOSITES

### 4.1.1. PHASE AND THERMODYNAMIC ANALYSES

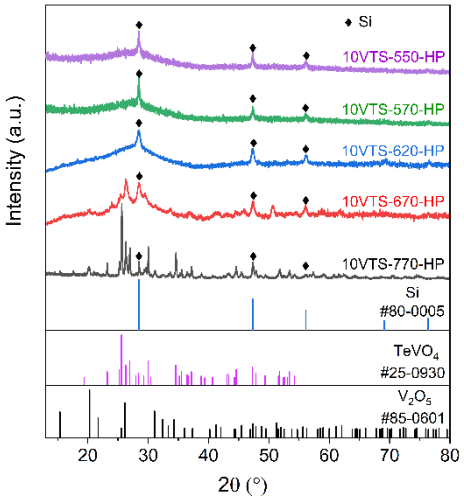


*Fig. 4-1 XRD patterns of 10VTS-550-HP, 10VTS-570-HP, 10VTS-620-HP, 10VTS-670-HP, and 10VTS-770-HP.*

Based on the DSC results of VTS in Fig. 3-1 (Chapter 3), the glass transition temperature ($T_g$), crystallization onset temperatures ($T_{c1}$ and $T_{c2}$), and melting temperature ($T_m$) are observed at 509, 563, 602, and 750K, respectively. To find out a

proper hot-pressing process, we firstly hot pressed 10VTS samples in a vacuum furnace under 100 MPa and kept for 0.5 h at different temperatures, i.e., 550K (above $T_g$), 570K (above $T_{c1}$), 620K (above $T_{c2}$), 670K (below $T_m$), and 770K (above $T_m$), where the number-10 represents the introduction of 10 wt.% Si nanoparticles into VT. According to the hot-pressing temperature, samples are referred to as 10VTS-550-HP, 10VTS-570-HP, 10VTS-620-HP, 10VTS-670-HP, and 10VTS-770-HP, respectively. For comparison, 10VTS was heated to 620K and kept for 0.5 h in the vacuum furnace without pressure, and the obtained sample is named as 10VTS-620.

Fig. 4-1 shows the XRD patterns of the 10VTS-550/570/620/670/770-HP samples. Clearly, in all the samples, Bragg diffraction peaks at 2θ≈28, 47, 56° are detected. These peaks are ascribed to Si crystals, suggesting the preservation of Si after heat-treatment. In addition, samples 10VTS-670-HP and 10VTS-770-HP show $V_2O_5$ and $TeVO_4$ crystals besides Si, while 10VTS-550-HP, 10VTS-570-HP, and 10VTS-620-HP samples only exhibit Si. This indicate that although 10VTS-570-HP and 10VTS-620-HP was heated above the first crystallization onset temperature $T_{c1}$ (563K) shown in DSC, no detectable new crystals were formed in both samples. This could be due to the different heating conditions between the different devices (DSC and furnace).

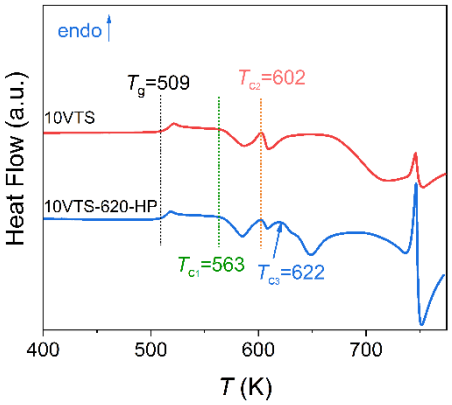


*Fig. 4-2 DSC upscan curves of both 10VTS and 10VTS-620-HP, which are obtained at the rate of 10 K/min in argon. The characteristic temperatures such as glass transition ($T_g$) and crystallization onset temperatures ($T_{c1}$, $T_{c2}$, and $T_{c3}$) are denoted in the curves.*

To study the effect of hot-pressing process on thermal properties of samples, we performed DSC measurements on both 10VTS and 10VTS-620-HP. As shown in Fig. 4-2, both 10VTS and 10VTS-620-HP show the same $T_g$, $T_{c1}$, and $T_{c2}$ values. However, a new crystallization peak ($T_{c3}$=622K) appears in 10VTS-620-HP, indicating the different potential energy and/or structure between those two samples. This is reasonable considering that 10VTS-620-HP has undergone heat-treatment compared to 10VTS. During heating 10VTS to 620K by hot pressing, the thermal energy can be used to increase the potential energy of the composite and overcome energy barrier of

a redox reaction which may occur between Si and VT [59], as shown in Chapter 3. Therefore, 10VTS-620-HP is more likely to precipitate new crystals in the subsequent DSC scan compared to 10VTS.

### 4.1.2. MORPHOLOGICAL AND STRUCTURAL CHARACTERIZATIONS

Fig. 4-3 shows the morphologies and EDS elemental mappings of samples 10VTS-620, 10VTS-620-HP, and 10VTS-670-HP. For 10VTS-620 (Fig. 4-3a), Si nano particles agglomerated and covered the surface of VT, verified by the SEM image and elemental mappings of Si, V, Te, suggesting that Si is only in physical contact with VT when no pressure is applied. In contrast, Si nano particles are embedded in the VT matrix and form Si/VT composites for 10VTS-620-HP (Fig.4-3b) and 10VTS-670-HP (Fig.4-3c). This indicate that compared with traditional heat-treatment, hot pressing method could be a more effective approach to combine Si with VT. Thereby, for hot-pressed samples, the VT is expected to buffer the volume change of Si during cycling.

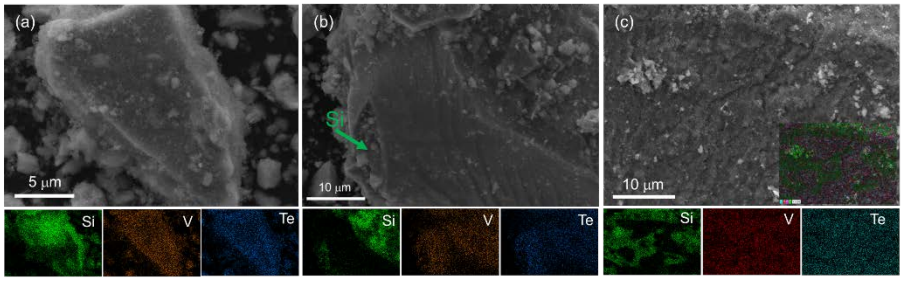


*Fig. 4-3 SEM images and EDS elemental mappings of Si, V and Te. (a) 10VTS-620, (b) 10VTS-620-HP, (c) 10VTS-670-HP, where the number, i.e., 10, represents the introduction of 10 wt.% Si nanoparticles into VT.*

The FTIR spectra of Si, 10VTS, 10VTS-620, and 10VTS-620-HP are shown in Fig. 4-4. Peaks at 478, 530, 680, 982, and 1000~1250 $cm^{-1}$ correspond to Si–O, V–O–V, Te–O–Te or O–Te–O, [$VO_5$], and Si–O vibrations [47-49, 59], respectively. When compared to the pristine 10VTS, the peak intensities at 1000–1250 $cm^{-1}$ for samples 10VTS–620 and 10VTS–620–HP rise, implying that Si was oxidized after heat-treatment. This phenomenon can only be explained by that VT oxidized Si, as the heating process is carried out in a vacuum. Moreover, 10VTS-620 shows a sharp peak at 530 $cm^{-1}$, which is not observed in 10VTS-620-HP. Instead, sample 10VTS-620-HP exhibit sharp peaks at 644 $cm^{-1}$ and 435 $cm^{-1}$, which are attributed to V–O–V/Te–O–Te vibrations [60, 61]. The spectral differences between 10VTS-620 and 10VTS-620-HP suggest that the pressure applied affects the structural evolution of VTS during heating.

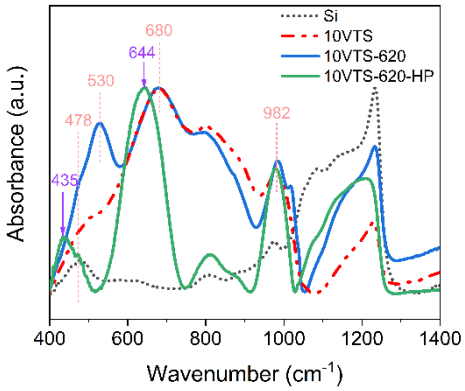


*Fig. 4-4 FTIR spectra of Si, 10VTS, 10VTS-620, 10VTS-620-HP, where the number, i.e., 10, represents the introduction of 10 wt.% Si nanoparticles into VT.*

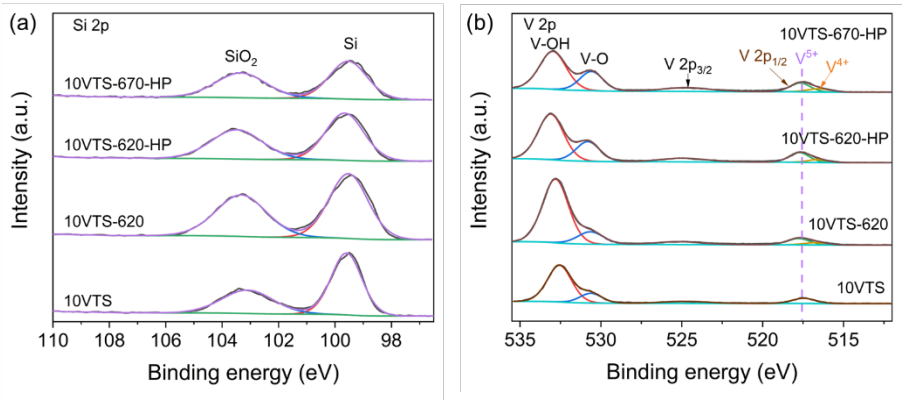


*Fig. 4-5 XPS high-resolution of Si 2p(a) and V 2p (b) spectra for 10VTS, 10VTS-620, 10VTS-620-HP, and 10VTS-670-HP.*

To further study the structural evolution upon heating, XPS measurements of 10VTS, 10VTS-620, 10VTS-620-HP, and 10VTS-670-HP were carried out. Fig. 4-5a shows the Si 2p spectra of samples. Each spectrum can be deconvoluted into peaks at ~99.5 eV (Si) and ~103.1 eV ($SiO_2$) [41]. The deconvolution results are shown in table 4-1. Clearly, more Si converts into $SiO_2$ with the increase of heating temperature. In addition, VTS-620 and VTS-620-HP show the same fractions of Si (~54.5%), indicating that the pressure does not promote the Si-to-$SiO_2$ conversion. Fig. 4-5b shows he high-resolution spectra of V 2p of these four samples. Peaks at 532.7, 530.6, 524.9, and 517.5 eV are ascribed to V-OH, V-O, V $2p_{3/2}$, and V $2p_{1/2}$, respectively [42, 43]. For the spectra of samples after heat-treatment, the V $2p_{1/2}$ peak becomes wider than that of pristine 10VTS. The wider peak can be deconvoluted into two peaks, i.e., $V^{5+}$ at ~517.5 eV and $V^{4+}$ at 516.4 eV, suggesting a redox reaction occurred in 10VTS

during the heating process, i.e., $V^{5+}$ oxidized Si and formed $V^{4+}$ and $SiO_2$. The formation of $V^{4+}$ could facilitate the electrical conductivity in VT glass. This is because during discharging processes, polarons formed due to the electron-phonon interaction, and thus, high electronic conductivity can be realized by polaron-hopping from $V^{4+}$ to $V^{5+}$. However, the formation of $SiO_2$, which is an insulating material, can decrease the electrical conductivity of materials. Therefore, there should be a compromise ratio between $V^{4+}$ and $SiO_2$ to achieve high electrical conductivity.

*Table 4-1 The fraction of Si, $SiO_2$ of VTS, VTS-620, VTS-620-HP, VTS-670-HP, which were obtained from the deconvoluted Si 2p XPS spectra shown in Fig. 4-5.*

| Samples \ Chemical state | Si (%) | $SiO_2$ (%) | Ratio ($Si/SiO_2$) |
|---|---|---|---|
| VTS | 61.1 | 38.9 | 1.6 |
| VTS-620 | 54.5 | 45.5 | 1.2 |
| VTS-620-HP | 54.6 | 45.4 | 1.2 |
| VTS-670-HP | 52.2 | 47.8 | 1.1 |

## 4.2. ELECTROCHEMICAL PERFORMANCES

### 4.2.1. CYCLING PERFORMANCE

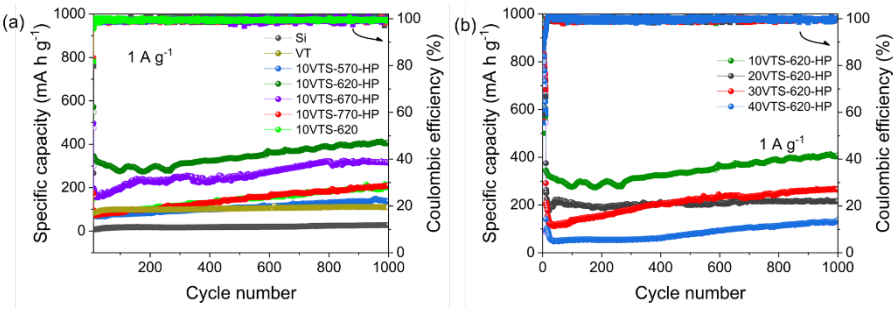


*Fig. 4-6 Cycling performances of anodes based on Si, VT, 10VTS-570-HP, 10VTS-620-HP, 10VTS-670-HP, 10VTS-770-HP, 10VTS-620, 20VTS-620-HP, 30VTS-620-HP, and 40VTS-620-HP.*

Fig. 4-6a shows the cycling performances of Si, VT, 10VTS-570-HP, 10VTS-620, 10VTS-620-HP, 10VTS-670-HP, and 10VTS-770-HP. Obviously, the capacities of 10VTS-620-HP and 10VTS-670-HP reach 408 and 313 mA h $g^{-1}$ at a current density of 1 A $g^{-1}$ up to 1000 cycles, respectively, while those of Si, VT, 10VTS-570-HP, 10VTS-620, 10VTS-770-HP are 28, 110, 136, 206, 205 mA h $g^{-1}$ respectively. The significant capacity enhancement of samples 10VTS-620-HP, 10VTS-670-HP compared with that of pure Si and VT verifies that the hot pressing is an effective

method to combine Si and VT and realize a good synergistic effect. Since 10VTS-620-HP shows higher capacity than the above-mentioned other samples, we increased the fraction of doping Si in VT, i.e., 20%, 30%, 40%, and hot pressed the mixture at the same condition as sample 10VTS-620-HP. According to the Si fraction, the as-prepared samples are referred to as 20VTS-620-HP, 30VTS-620-HP, and 40VTS-620-HP, respectively. The cycling performances of these samples are shown in Fig. 4-6b. Clearly, as the Si fraction increases from 20% to 40%, the capacities of the corresponding samples are 216, 260, and 126 mA h $g^{-1}$, respectively. A higher fraction of Si in VTS leads to a lower capacity than 10VTS-620-HP, indicating that 10 wt.% Si is the optimal doping level.

### 4.2.2. RATE PERFORMANCE

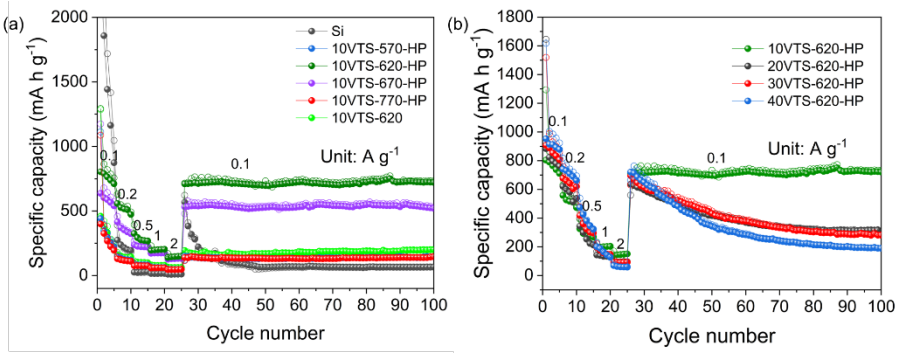


*Fig. 4-7 The rate performances of anodes based on Si, 10VTS-570-HP, 10VTS-620, 10VTS-620-HP, 10VTS-670-HP, 10VTS-770-VTS, 20VTS-620-HP, 30VTS-620-HP, and 40VTS-620-HP at current densities of 0.1, 0.2, 0.5, 1, 2 A $g^{-1}$.*

Fig. 4-7 shows the rate performances of Si, 10VTS-570-HP, 10VTS-620, 10VTS-620-HP, 10VTS-670-HP, 10VTS-770-VTS, 20VTS-620-HP, 30VTS-620-HP, and 40VTS-620-HP samples at the current densities of 0.1, 0.2, 0.5, 1, and 2 A $g^{-1}$. In Fig. 4a, the capacity of Si drops dramatically from 2290 to 774 mA h $g^{-1}$ while capacities of 10VTS-570-HP, 10VTS-620, and 10VTS-770-HP decrease from ~450 to ~200 mA h $g^{-1}$ after 5 cycles at 0.1 A $g^{-1}$. In contrast, the capacities of samples 10VTS-620-HP and 10VTS-670-HP are more stable and deliver average charging/discharging capacities of 725 and 621 mA h $g^{-1}$ after 5 cycles at 0.1 A $g^{-1}$, respectively. With the stepwise increase in the current density, the average capacities of all samples decrease, and among them, 10VTS-620-HP exhibits the highest capacity retention after performing 5 cycles at 0.2 0.5, 1, and 2 A $g^{-1}$. When the current density was decreased back to 0.1 A $g^{-1}$, the capacities of 10VTS-620-HP and 10VTS-670-HP recover to 710 and 532 mA h $g^{-1}$, respectively, and remain stable in the following cycles, while the capacity of Si reaches 568 mA h $g^{-1}$ but decreases rapidly to 67 mA h $g^{-1}$ after 100 cycles in total. The significant capacity decrease of Si is due to its volume change and pulverization during cycling [31, 32]. The enhanced rate capacities in both 10VTS-

620-HP and 10VTS-670-HP compared with pure Si, further confirm the effectiveness of the hot-pressing strategy.

The rate performances of the 10VTS-620-HP, 20VTS-620-HP, 30VTS-620-HP, and 40VTS-620-HP are shown in Fig. 4-7b. The average capacity of the 20VTS-620-HP, 30VTS-620-HP, and 40VTS-620-HP in the first five cycles is 808, 857, and 910 mA h $g^{-1}$, respectively, which is greater than that of the 10VTS-620-HP (725 mA h $g^{-1}$). However, these three samples are sensitive to current density, and the capacity retention decreases rapidly as the current density increases. When the current was decreased back to 0.1 A $g^{-1}$, the capacities of 20VTS-620-HP, 30VTS-620-HP, and 40VTS-620-HP samples are 636, 695, and 720 mA h $g^{-1}$, respectively, and after 100 cycles, the capacities of these three samples are 316, 281, and 189 mA h $g^{-1}$, respectively. This rapid capacity decline in 20VTS-620-HP, 30VTS-620-HP, and 40VTS-620-HP samples could be interpreted that although these three samples contain higher percentages of doped Si than the 10-VTS-620-HP, not all the Si nanoparticles are properly embedded into the VT glass matrix due to the limited storage capability of the glass for Si. A larger fraction of doping may cause more bare Si nanoparticles to aggregate on the surface of the VT particles as opposed to being embedded in the protective glass matrices, resulting in a higher percentage of Si undergoing volume changes and pulverization. Hence a rapid decline in capacity is observed.

### 4.2.3. CYCLIC VOLTAMMETRY CURVE

To study why the 10VTS-620-HP based anode shows higher capacity than other samples with higher Si fraction or higher temperature, Cyclic Voltammetry (CV) measurements of 10VTS-620-HP, 10VTS-670-HP, 30VTS-620-HP, and 40VTS-620-HP were performed (Fig. 4-8). For 10VTS-620-HP (Fig. 4-8a), the reduction peaks at around 1.01 V, 0.66 V, and 0.02 V are observed, which can be attributed to the interaction between $Li^+$ and VT, formation of solid electrolyte interface film (SEI), and the alloying of $Li^+$ with Si, forming $Li_xSi$ phase, respectively [62-64]. Peaks at around 0.34 V and 0.54 V in the delithiation process indicate the extraction of $Li^+$ from $Li_xSi$, while peaks at ~1.26 and ~2.08 attribute to the extraction of $Li^+$ from VT glass matrix [18, 19]. In the subsequent two CV cycles, peaks at 1.01 and 0.66 V disappear and instead, a new strong peak located at ~0.85 V is observed, which arises from the insertion of $Li^+$ into VT [19].

Fig. 4-8b shows the CV curves of 10VTS-670-HP, in which both glass and V/V-Te containing crystals ($V_2O_5$ and $TeVO_4$) are present. In the first cathodic scan, peaks at 1.83 V, 0.97 V, 0.63 and 0.02 V are observed. The former two peaks should correspond to the insertion of $Li^+$ into VT glass-ceramic, while the latter two peaks are ascribed to the formation of SEI and the alloying of $Li^+$ with Si, respectively. The anodic peak positions are similar to those of 10VTS-620-HP, except that the peaks shift from 1.26 and 2.08 V in 10VTS-620-HP to 1.31 and 2.21 V in 10VTS-670-HP.

These two peaks should be attributed to the $Li^+$ extraction from VT glass-ceramic. In the second and third CV curves, new strong peaks at ~0.91 V appear due to the $Li^+$ insertion into VT glass-ceramic. Obviously, peaks corresponding to Si insertion/extraction (0.02, 0.34, and 0.54 V) in 10VTS-670-HP are weaker than those in 10VTS-620-HP (Fig. 4-8a), indicating that the reversible reaction between Si and $Li_xSi$ is reduced. This can be explained by the fact that more Si in the VTS is transformed into $SiO_2$ when the hot-pressing temperature rises, resulting in fewer Si active sites and hence decreased capacity.

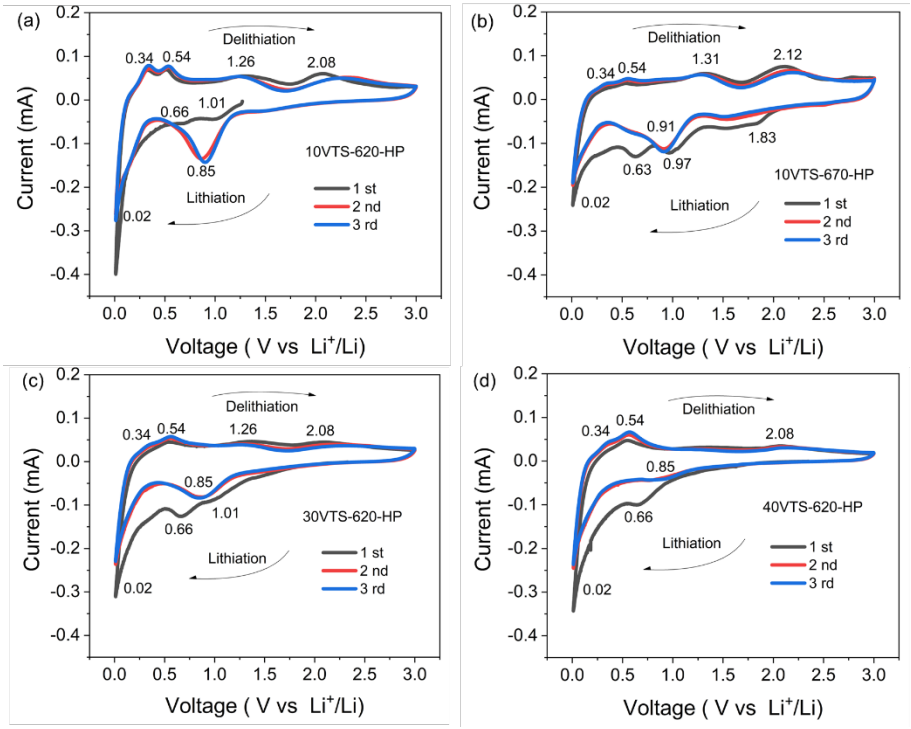


*Fig. 4-8 Cyclic Voltammetry (CV) curves of 10VTS-620-HP(a), 10VTS-670-HP(b), 30VTS-620-HP(c), 40VTS-620-HP(d) within the range from 0.01 to 3.0 V at a scan rate of 0.1 mV $s^{-1}$.*

The CV curves of the 30VTS-620-HP and 40VTS-620-HP are shown in Figs. 4-8c, d. Clearly, the cathodic and anodic peak positions of 30VTS-620-HP (Fig. 4-8c) are identical to those of 10VTS-620-HP (Fig. 4-8a), but peak intensities of the former are weaker. This suggests that in 30 VTS-620-HP, fewer $Li^+$ inserted/extracted into/from both Si/$Li_xSi$ and VT matrix. In contrast to 10VTS-620-HP, 40VTS-620-HP in Fig. 4-8d displays weaker peaks at 0.02, 0.34, and 0.54 eV and no anodic peak at 1.26 eV. Additionally, in 40VTS-620-HP, the peaks at 0.85 and 2.08 eV are essentially undetectable. These results imply that as the fraction of doping Si increases, the reversible reactions decrease, i.e., fewer $Li^+$ inserted/extracted into/from Si or $Li_xSi$

and VT, resulting in a decrease of capacity. This is reasonable considering the limited capability of VT matrix to accommodate Si. When the amount of Si particles exceeds the limitation of the VT glass, the excess Si cannot be embedded into the VT matrix by hot pressing. Instead, Si particles aggregated and covered the surface of VT particles, preventing $Li^+$ from entering the VT matrix. Furthermore, due to volume fluctuations during charge/discharge, the bare Si without the protection of the VT matrix is easily pulverized, resulting in a quick drop in capacity.

### 4.2.4. ELECTROCHEMICAL IMPEDANCE SPECTRA

The electrochemical impedance spectroscopy (EIS) of the 10VTS-620-HP and 10VTS-670-HP is displayed in Fig. 4-9. One semicircle is present at high frequency on each EIS curve, while an inclined line is present at low frequency. The resistance parameters (table 4-2) were obtained from the inset equivalent circuit. Obviously, 10VTS-620-HP shows a smaller charge transfer resistance ($R_{ct}$=161.6 Ω) than 10VTS-670-HP ($R_{ct}$=354.8 Ω), indicating that the former exhibits a higher electrical conductivity, which leads to a better electrochemical performance in 10VTS-620-HP.

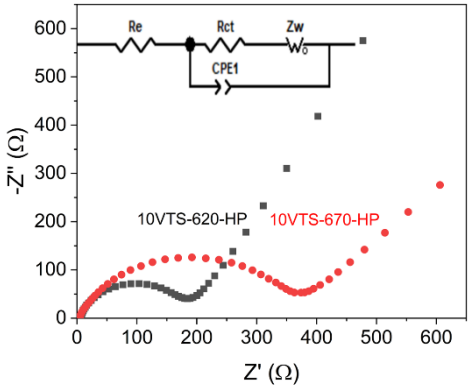


*Fig. 4-9 Nyquist plots of 10VTS-620-HP and 10VTS-670-HP, which were obtained from electrochemical impedance spectra within the frequency range from 0.01 Hz to 100 kHz.*

*Table 4-2 Calculated impedance ($R_e$, $R_{ct}$) of 10VTS-620-HP and 10VTS-670-HP based on EIS equivalent circuit model.*

| Impedance / Samples | $R_e$ (Ω) | $R_{ct}$ (Ω) |
|---|---|---|
| 10VTS-620-HP | 4.4 | 161.6 |
| 10VTS-670-HP | 3.4 | 354.8 |

## 4.3. PROPOSED MECHANISM

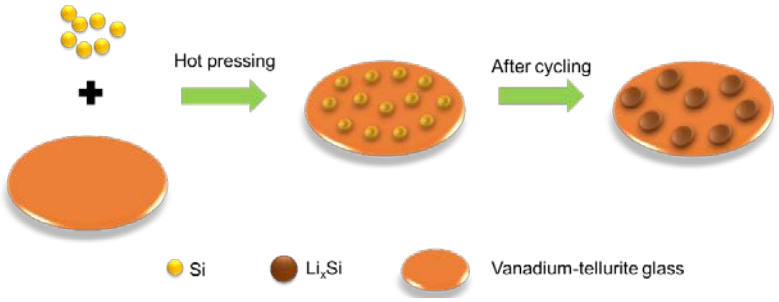


*Fig. 4-10 The protecting role of VT glass matrix, which prolongs the cycling life of Si.*

The structural origin of the electrochemical performance enhancements of VTS after hot pressing is related to the synergistic effects of VT glass matrix and the embedded nano-Si particles in lithium storage. First, the open disordered network structure that VT glass demonstrates is advantageous for $Li^+$ diffusion. Second, the Si was embedded into VT matrix, which confines the volume expansion and buffers pulverization of Si during the insertion of $Li^+$ into the composite, leading to good cycling stability. Specifically, compared with bare Si without the protection of glass, fewer Li-ions reacting with the embedded Si due to that some $Li^+$ ions diffuse and store in the VT glass matrix in the composite during discharging. That is, to some extent, the VT glass matrix suppress the alloying of $Li^+$ with Si. Moreover, the volume expansion of the embedded Si during alloying can be confined by the glass matrix (as shown in Fig. 4-10), leading to a lower degree of volume change and pulverization of Si. Third, the electrical conductivity of VTS can be increased by the production of $V^{4+}$ as a result of the redox reaction between Si and VT during heat-treatment. Therefore, the VTS-HP samples outperform pristine Si, VT, and VTS in terms of reversible capacity and rate capability.

## 4.4. SUMMARY

In this chapter, we used a hot-pressing technique to embed Si nanoparticles into the vanadium-tellurite glass (VT) matrix to create Si/VT composites (VTSs) for lithium storage. By optimizing the hot-pressing temperature and Si fraction, the VTS can yield a strong synergistic effect. The capacity of the anode made from 10VTS-620-HP after 1000 cycles at 1 A $g^{-1}$ is 408 mA h $g^{-1}$, which is 3 times that of VT and 14 times that of pure Si. The significant performance enhancement could be due to that the VT glass with an open disordered network can provide channels for lithium transfer, as well as the glass matrix buffers the volume change of Si. Additionally, the electron transfer in 10VTS-620-HP can be facilitated by the formation of $V^{4+}$ arising from the redox interaction between Si and VT during heat treatment.

# CHAPTER 5. STRUCTURE AND PERFORMANCES OF SI@MOF-GLASS COMPOSITES

Metal-organic frameworks (MOFs), which are constructed by metal ion nodes and organic ligands, have shown great potential to be applied in the fields of energy and environmental technology. This potential is mainly due to their great porosity, huge surface, abundant reaction sites and tunable structures [20]. In this regard, scientists are attempting to develop MOF-based electrodes for lithium-ion batteries (LIBs). Despite some progress, there are still three major barriers for developing superior MOF-based anodes: 1) low capacity; 2) poor cycling stability; 3) limited electronic conductivity.

About 6 years ago, a new family of MOFs, i.e., the MOF glasses via melt-quenching, were discovered by Yue et al. [25]. In contrast to crystalline MOFs, glassy MOFs possess disordered network structures with higher potential energy, and hence, contain larger free volume and more channels for lithium-ion storage and diffusion. These characteristics enable MOF glasses to exhibit better electrochemical performances than their crystalline counterparts [20]. However, it is still challenging to further enhance the capacity of MOF glass anodes owing to the limited $Li^+$ intercalation. Silicon is well known to have high theoretical capacity but poor cycling stability. This inspired us to fabricate composite by combing the advantages of MOF glass and high-capacity Si material to obtain high-performance anodes.

Zeolitic imidazolate framework (ZIF) is a subset of MOFs. In this Chapter (based on Paper II), Si nanoparticles were wrapped into cobalt-ZIF-62 by a reflux method. It should be mentioned that cobalt-ZIF-62 is a type of ZIF with the composition of $Co(imidazole)_{1.75}(benzimidazole)_{0.25}$. After melt-quenching the Si@ZIF composite (SiZC), the Si@ZIF-glass composite (SiZGC) was obtained (see 2.1.4 for details). We investigated the composition-structure-electrochemical performance relations of the SiZGC.

## 5.1. CHARACTERIZATIONS OF SI@ZIF COMPOSITES

### 5.1.1. PHASE AND THERMODYNAMIC ANALYSES

Fig. 5-1 shows the XRD patterns of the ZIF crystal (Z), ZIF glass (ZG), 10Si@ZIF composite (10SiZC), 10Si@ZIF-glass composite (10SiZGC), and the simulated ZIF-62 crystal, where the number, i.e.,10, represents that weight percent of Si nanoparticles introduced into ZIF-62. Samples Z, 10SiZC, and simulated ZIF-62 show

sharp diffraction peaks in the range of 10°~25°, indicating the existence of ZIF crystals in these samples [20]. In contrast, sample ZG and 10SiZGC show no diffraction peaks between 10°~25°, suggesting their amorphous nature. In addition, the Bragg diffraction peaks corresponding to Si crystals were observed in both 10SiZC and 10SiZGC, indicating the existence of Si particles in the composites. Thus, the melt-quenching method only changed the crystal structure of ZIF but did not affect the crystal structure of Si.

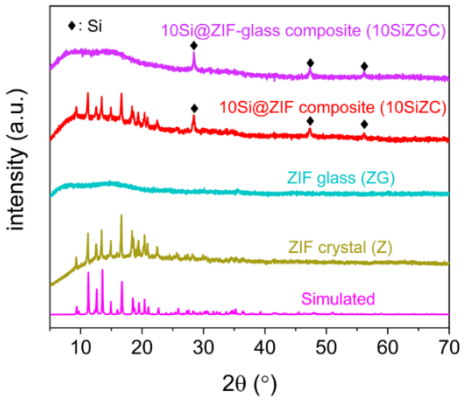


*Fig. 5-1 XRD patterns of the ZIF-62 crystal (Z), ZIF-62 glass (ZG), 10Si@ZIF-62 composite (10SiZC), 10Si@ZIF-62-glass composite (10SiZGC), and the simulated ZIF-62 crystal, where the number, i.e., 10, represents that weight percent of Si nanoparticles introduced into ZIF-62.*

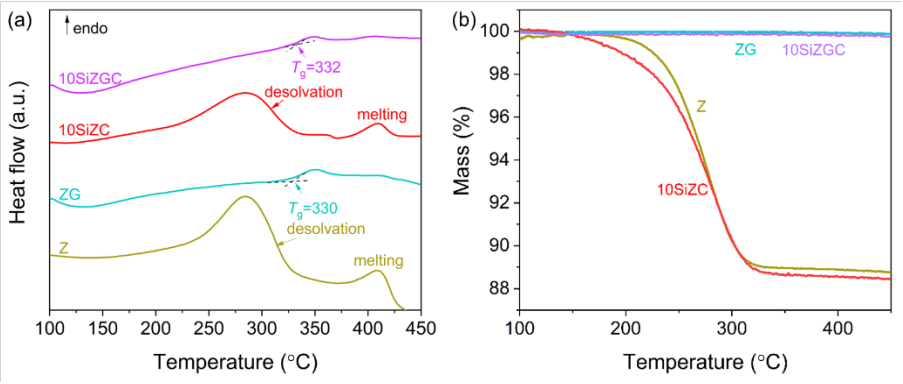


*Fig. 5-2 DSC upscan curves (a) and thermogravimetric curves (b) of the ZIF crystal (Z), ZIF glass (ZG), 10Si@ZIF composite (10SiZC), and 10Si@ZIF-glass composite (10SiZGC), which were obtained at 10 ℃ $min^{-1}$ in argon.*

DSC upscan curves and thermogravimetric (TG) curves of Z, ZG, 10SiZC and 10SiZGC samples are shown in Fig. 5-2. For both Z and 10SiZC, the DSC curves (Fig. 5-2a) exhibit endothermic peaks at around 280°C and 420°C, which are due to the

release of solvent and the melting event, respectively. However, ZG and 10SiZGC samples show a different situation in which the glass transition is observed at ~330°C. This suggests that the vitrification of ZIF in 10SiZC is not affected by the introduction of Si. To evaluate the thermal stability, TG measurements of these four samples are conducted (Fig. 5-2b). Clearly, in the temperature range of 150~300°C, significant mass loss is observed in both Z and 10SiZC while no mass loss occurs in both ZG and 10SiZGC. This is because the solvent (DMF) is released from the former two samples during the heating process.

### 5.1.2. MORPHOLOGICAL AND STRUCTURAL CHRACTERIZATIONS

Fig. 5-3 shows the morphologies of samples 10SiZC and 10SiZGC. For 10SiZC (Fig. 5-3a), the SEM images and EDS elemental mappings of Co, N, and Si verify that Si nanoparticles are wrapped into ZIF layers with a size about 10 µm. In Fig. 5-3b, the morphologies of 10SiZGC are similar to those of 10SiZC, suggesting that the ZIF architectures remain after melt-quenching. In addition, the enlarged image (Fig. 5-3b) indicates that small Si particles are wrapped by ZIF-62 glass. Thus, as expected, SiZC and SiZGC are obtained by the facile reflux and the combination of reflux and melt-quenching methods, respectively.

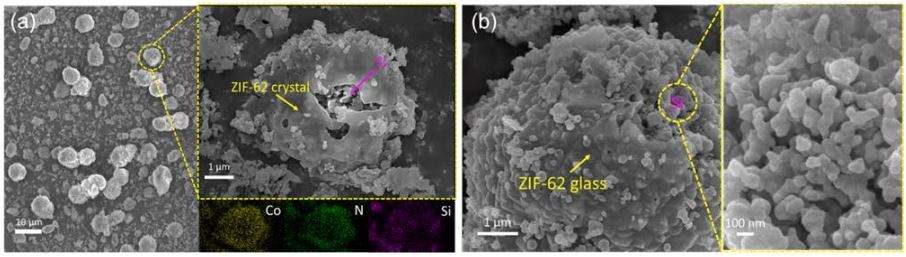


*Fig. 5-3 (a) SEM images of the 10Si@cobalt-ZIF-62composite (10SiZC) (Inset: EDS elemental mappings of Co, N and Si for SZ); (b) SEM images of the 10Si@cobalt-ZIF-62-glass composite (10SiZGC).*

To study the structure of the as-prepared samples, FTIR and Raman measurements were performed. Fig. 5-4a shows the FTIR spectra of Z, ZG, 10SiZC and 10SiZGC. Obviously, these four spectra show similar frequency bands corresponding to the intramolecular vibrations, suggesting that the integrity of organic linkers in ZIFs are preserved during melt-quenching [27]. Peaks at ~430, ~835, 668, and 1082 $cm^{-1}$ are ascribed to the Co-N bonds, in-plane bending of the aromatic ring [20, 65], the ring deformation out-of-plane-bending in the organic ligands, and the C-H bending vibrations, respectively [20]. Clearly, the peaks in the crystal at around 430 and 835$cm^{-1}$ shift to a lower wavenumber after vitrification. The intensity ratio between the 668 and 1082 $cm^{-1}$ peaks increases when the ZIF crystal transform into glass. These indicate that ZG and 10SiZGC exhibit weaker Co-N bonds, aromatic rings, and an increased structure distortion compared with Z and 10SiZC. In addition, peaks at

1383 and 1675 $cm^{-1}$ corresponding to the vibrational mode of C-H and the carbonyl groups of solvent molecules (DMF), respectively, are not observed in the glass-based samples [20, 66]. This indicates that the DMF molecules have escaped from Z or 10SiZC during melt-quenching process, agreeing with the DSC results. Since Si is FTIR-inactive, Si-Si bonds were not detected in FTIR spectra of 10SiZC and 10SiZGC. However, the Raman spectra of these two samples in Fig. 5-4b clearly show Si-Si bonds at ~517 $cm^{-1}$ [67], confirming the existence of Si in the target composites.

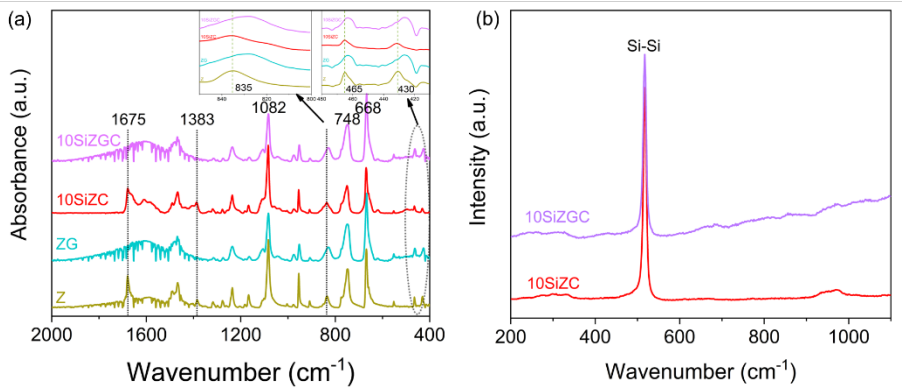


*Fig. 5-4 (a)FTIR spectra of Z, ZG, 10SiZC and 10SiZGC. (b) Raman spectra of 10SiZC and 10SiZGC.*

## 5.2. ELECTROCHEMICAL PERFORMANCES

### 5.2.1. CYCLING PERFORMANCE

The cycling performances of the Si, Z, ZG, 5SiZC, 5SiZGC, 10SiZC, 10SiZGC, 15SiZC, and 15SiZGC based anodes at a current density of 1 A $g^{-1}$ for 500 cycles were shown in Fig. 5-5a. Obviously, the Si-doped composite samples exhibit higher capacities than those of the pristine ZIF crystal/glass and Si. In addition, the capacities of 5SiZGC and 10SiZGC are higher than those of 5SiZC and 10SiZC. In detail, the capacities of 5SiZGC and 10SiZGC based anodes reach 550 and 650 mA h $g^{-1}$ at 1 A $g^{-1}$ after 500 cycles, respectively, while those of 5SiZC and 10SiZC are 380 and 600 mA h $g^{-1}$, respectively. Moreover, the capacity of 10SiZGC based anode is more than three times that of ZG (210 mA h $g^{-1}$), six times that of pristine ZIF crystal (108 mA h $g^{-1}$) and thirty times that of pure Si (20 mA h $g^{-1}$). The above results not only suggest that the Si@ZIF composite gives a synergistic effect (i.e., a combination of high capacity and high cycling stability) compared with pure Si and ZIFs, but also indicate the important role of ZIF glass in protecting Si in the composite. When 10SiZGC was subjected to longer cycling (Fig. 5-5b), the capacity of 10SiZGC peaked at 660 mA h $g^{-1}$ at 570 cycles and then declined to 450 mA h $g^{-1}$ after 1000 cycles. This could be

attributed to the structural evolution of ZIF and the pulverization of Si during lithiation/delithiation.

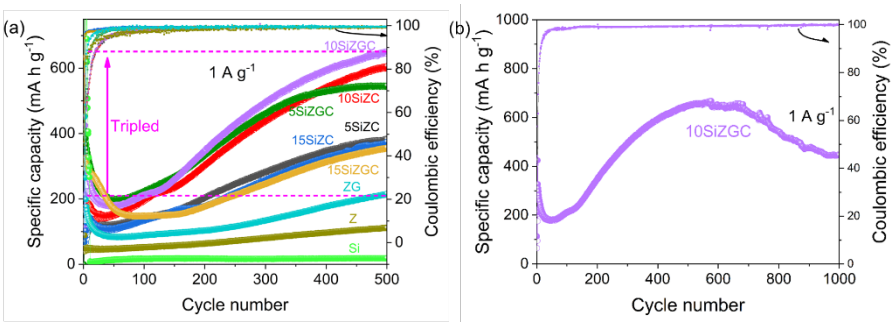


*Fig. 5-5 (a) The cycling performances of anodes based on the ZIF crystal (Z), ZIF glass (ZG), 5Si@ZIF composite (5SiZC), 5Si@ZIF-glass composite (5SiZGC), 10Si@ZIF composite (10SiZC), 10Si@ZIF-glass composite (10SiZGC), 15Si@ZIF composite (15SiZC), and 15Si@ZIF-glass composite (15SiZGC) at 1 A $g^{-1}$ for 500 cycles, and (b) cycling performance of 10SiZGC at 1 A $g^{-1}$ for 1000 cycles.*

## 5.2.2. RATE PERFORMANCE

The rate capabilities of 5SiZC, 10SiZC, 15SiZC, 5SiZGC, 10SiZGC, and 15SiZGC samples are shown in Fig. 5-6. Samples 15SiZGC, 10SiZGC, and 5SiZGC deliver the average capacities of 666, 516, and 482 mA h $g^{-1}$ within the first 10 cycles at 0.1 A $g^{-1}$, respectively, which are higher than their crystalline counterparts. This can be explained that the ZIF glass phase provides more Li-ion intercalation sites arising from increased distortion and defects compared with crystalline ZIF [20]. As the current density increases, the average capacities decrease for all the samples, among which 5SiZGC exhibits the highest capacity retention after cycles at 0.5, 1, 2, and 5 A $g^{-1}$. In contrast, both 15SiZGC and 10SiZGC are sensitive to the current density and show a rapid drop in capacity with an increase of the current density. When the current density was set back to 0.1 A $g^{-1}$, the specific capacity of 5SiZGC recovers to 432 mA h $g^{-1}$ and remains stable in the following cycles, while that of 15SiZGC and 10SiZGC restores to 540 and 440 mA h $g^{-1}$, respectively, but decreases in the subsequent cycles. This could be explained by the fact that, although 15SiZGC and 10SiZGC contain more Si than 5SiZGC, not all the Si nanoparticles in the composite contributed to the capacity increase within the studied 80 cycles. When more Si nanoparticles are introduced into the composite, such as the 10SiZGC, not all Si can be encapsulated into glassy ZIF cages, as shown in Fig. 5-3a. Therefore, due to the absence of the ZIF protection layer, the excess Si particles would aggregate and collapse during lithiation/delithiation, resulting in a decrease in capacity.

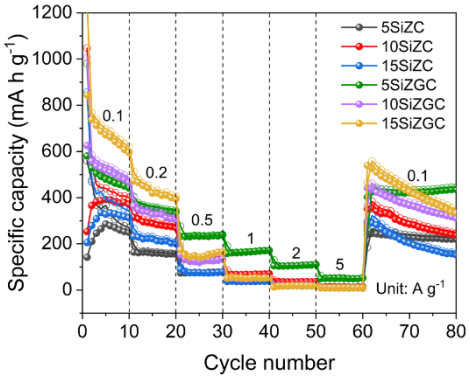


*Fig. 5-6 The rate performances of anodes based on the 5SiZC, 5SiZGC, 10SiZC, 10SiZGC, 15SiZC, and 15SiZGC at current densities of 0.1, 0.2, 0.5, 1, 2, 5 and 0.1A $g^{-1}$.*

## 5.2.3. CYCLIC VOLTAMMETRY CURVE

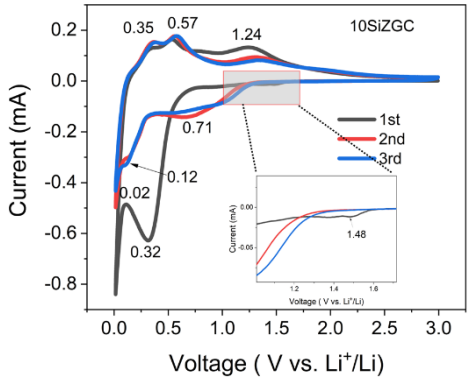


*Fig. 5-7 Cyclic Voltammetry (CV) curves of pristine 10SiZGC within the range from 0.01 to 3.0 V at a scan rate of 0.1 mV $s^{-1}$.*

Fig. 5-7 shows the CV curves of 10SiZGC at a scan rate of 0.1 mV $s^{-1}$. In the first cathodic scan, three reduction peaks at around 1.48 V, 0.32 V, and 0.02 V appear, attributing to the storage of $Li^+$ within ZIF, formation of SEI and $Li_xSi$ phase, respectively [62-64, 68]. Peaks at around 0.35 and 0.57 V in the anodic scan are ascribed to dealloying of $Li_xSi$ to Si, while the peak at ~1.24 V arises from the extraction of $Li^+$ from ZIF glass [20, 64]. In the subsequent two CV cycles, peaks at 1.48 and 0.32 V in the cathodic scan disappeared. Instead, a broad peak at 0.71 V and a small peak at 0.12 V are observed, which correspond to the insertion of $Li^+$ into ZIF glass and the alloying of $Li^+$ with Si, respectively [69].

### 5.2.4. ELECTROCHEMICAL IMPEDANCE SPECTRA

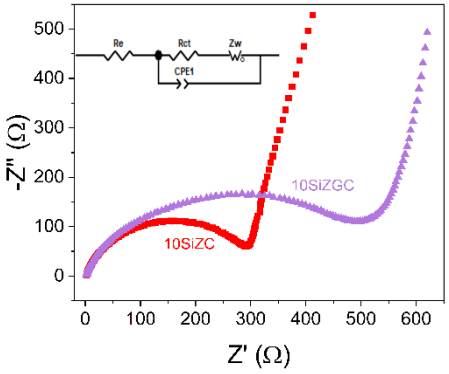


*Fig. 5-8 Nyquist plots of 10SiZC and 10SiZGC before and after cycling obtained from electrochemical impedance spectra within the frequency range from 0.01 Hz to 100 kHz.*

Fig. 5-8 shows the EIS of pristine10SiZC and 10SiZGC. For each sample, the depressed semicircle in the high-frequency region correspond to charger transfer resistance ($R_{ct}$) and interface capacitance ($C_{PE}$), while the inclined line in the low-frequency region is ascribed to diffusion impedance ($Z_w$). [20, 70]. According to fitting results of the equivalent circuit for the Nyquist plots (the inset), the ohmic resistance ($R_e$) of 10SiZC and 10 SiZGC are 2.1 and 1.3 Ω, while the $R_{ct}$ of 10SiZC and 10SiZGC are 290.4 and 405.3 Ω, respectively. This suggests that for pristine composites, 10SiZC shows a higher electrical conductivity than 10SiZGC.

## 5.3. CHARACTERIZATIONS OF SI@ZIF COMPOSITES AFTER CHARGING/DISCHARGING CYCLING

### 5.3.1. STRUCTURAL AND MORPHORLOGICAL CHARACTERIZATIONS

XPS measurements were conducted on both 10SiZC and 10SiZGC before and after cycling (Fig. 5-9). The high-resolution spectra of Co 2p show two main peaks (Fig. 5-9a), i.e., peaks at 796.2 and 781.1eV attributed to the Co $2p_{1/2}$ and Co $2p_{3/2}$, respectively, suggesting the existence of $Co^{2+}$ in both pristine 10SiZC and 10SiZGC [20]. After cycling, the two peaks (796.2 and 781.1 eV) slightly shift to higher binding energy, implying that the chemical environment of cobalt in 10SiZC and 10SiZGC varies upon insertion/extraction of $Li^+$. This could be due to the distortion and breakage of the Co-N [20]. In Fig. 5-9 b, each spectrum of N 1s can be deconvoluted into two peaks, i.e., 398.7 eV (C=N-C) and 400.4 eV (C-N-H) [20, 71]. According to the deconvolution results in Table 5-1, the fraction of the C=N-C bonds is the same (i.e., about 94%) in both pristine 10SiZC and 10SiZGC. However, the C=N-C bond

fractions in both samples decrease to ~73% after cycling, indicating the breakage of C=N-C upon cycling.

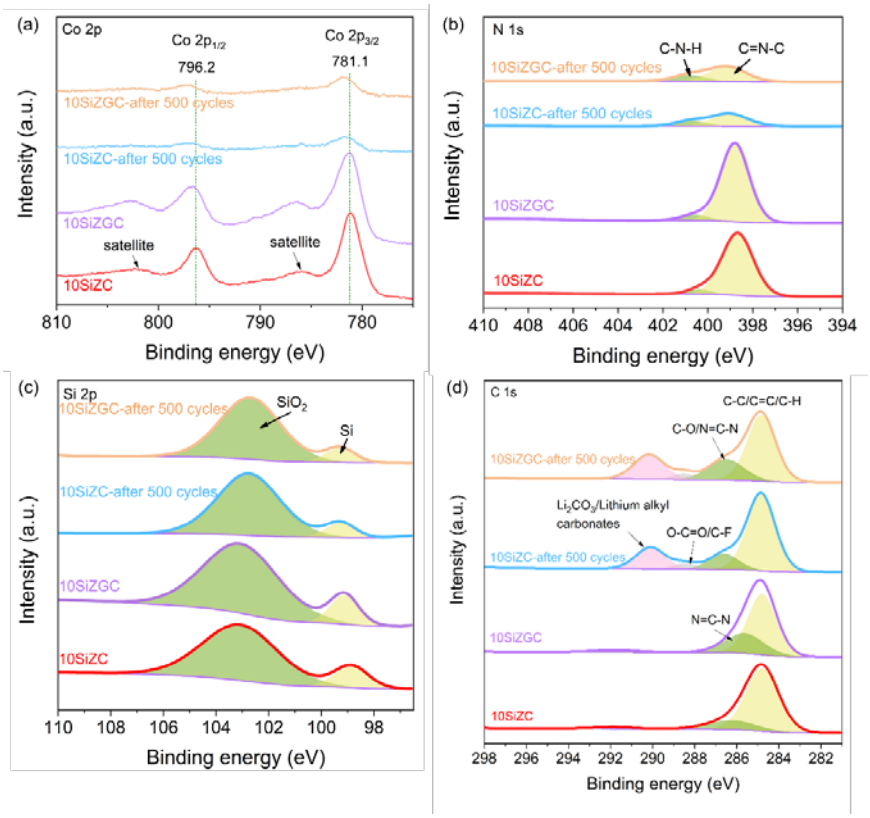


*Fig. 5-9. XPS high-resolution spectra of Co 2p (a), N 1s (b), Si 2p (c) and C 1s (d) for 10SiZC and 10SiZGC before and after cycling.*

*Table 5-1 The fraction of C=N-C, C-N-H of 10SiZC and 10SiZGC before and after cycling, which were obtained from the deconvoluted N 1s XPS spectra shown in Fig. 5-9b.*

| Bonds / Samples | C=N-C (%) | C-N-H (%) | Ratio (C=N-C/C-N-H) |
|---|---|---|---|
| 10SiZC | 94.3 | 5.7 | 16.5 |
| 10SiZGC | 93.1 | 6.9 | 13.5 |
| 10SiZC-after cycling | 73.8 | 26.2 | 2.8 |
| 10SiZGC-after cycling | 72.9 | 27.1 | 2.7 |

For both samples before and after cycling, the XPS spectra of Si (Fig. 5-9c) exhibit similar characteristics. Each spectrum can be deconvoluted into two peaks and the results are shown in Table 5-2. The high fraction of $SiO_2$ in the XPS of the four samples can be explained as follows: Since Si oxidizes easily when exposed to air,

$SiO_2$ forms even at room temperature [72]. In other words, $SiO_2$ is already existing in the as-purchased commercial Si nanoparticles, verified by the FTIR and XPS results in Chapters 3 and 4. However, considering the XPS detection depth limitation, $SiO_2$ is predominant only in the surface layer (< 5 nm). Overall, the fraction of $SiO_2$ in the as-purchased Si is still much smaller than that of Si. For the high-resolution XPS spectrum of C 1s (Fig. 5-9d), the peaks of pristine 10SiZC and 10SiZGC can be deconvoluted into two peaks, i.e., 284.8 eV (C-C/C=C/C-H) and 286 eV (N=C-N). After cycling, the C 1s spectra of 10SiZC and 10SiZGC can be deconvoluted into four peaks. i.e., 284.8, 286.6, 288.5, and 290.1 eV, which are related to C-C/C=C/C-H, C-O/N=C-N, O-C=O/C-F, and $Li_2CO_3$ or lithium alkyl carbonates, respectively. The new deconvoluted peaks arise from the addition of PVDF and the formation of SEI during cycling [20, 73-75].

*Table 5-2 The fraction of Si, $SiO_2$ of 10SiZC and 10SiZGC before and after cycling, which were obtained from the deconvoluted Si2p XPS spectra shown in Fig. 5-9c.*

| Chemical state / Samples | Si (%) | $SiO_2$ (%) | Ratio ($Si/SiO_2$) |
|---|---|---|---|
| 10SiZC | 15.0 | 85.0 | 0.18 |
| 10SiZGC | 13.8 | 86.2 | 0.16 |
| 10SiZC-after cycling | 10.0 | 90.0 | 0.11 |
| 10SiZGC-after cycling | 10.2 | 89.8 | 0.11 |

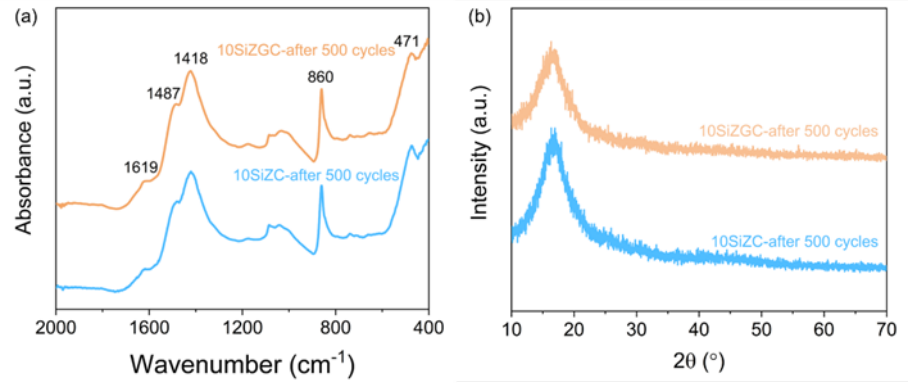


*Fig. 5-10 FTIR spectra (a) and XRD patterns (b) of the 10SiZC and 10SiZGC after cycling.*

Fig. 5-10 shows the FTIR spectra and XRD patterns of 10SiZC and 10SiZGC after cycling. In Fig. 5-10a, the FTIR spectra of 10SiZC and 10SiZGC are almost the same, suggesting that both samples have similar structural features after cycling. In addition, compared with peaks in FTIR spectra of pristine 10SiZC and 10SiZGC(Fig. 5-4a), many peaks disappeared for both samples after cycling, including peaks at around 835, 748, 668, and 430 $cm^{-1}$ attributed to the in-plane-blending of aromatic ring, the

benzene group of imidazole/benzimidazole, the ring deformation out-of-plane-bending in the organic ligands, and the Co-N bonds, respectively [20, 65, 76]. This further verifies breakages of the aromatic rings and Co-N bonds after cycling. The XRD patterns of 10SiZC and 10SiZGC after 500 cycles are shown in Fig. 5-10b. Obviously, no sharp diffraction peak but a broad peak at 2θ≈16° is observed in each XRD pattern, indicating the transformation of crystalline Si in both samples and crystalline ZIF in 10SiZC sample into amorphous materials upon cycling.

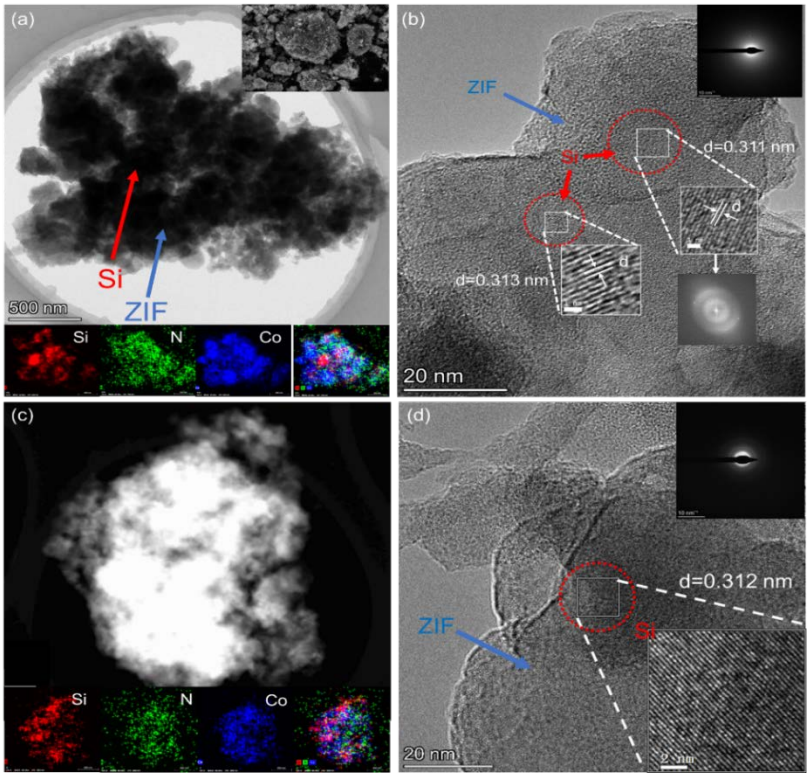


*Fig. 5-11 (a), (c) TEM images and EDS mappings of Si, N, Co for 10SiZGC and 10SiZC after cycling, respectively. (b), (d) HRTEM images and the corresponding SAED patterns of 10SiZGC and 10SiZC after cycling.*

Fig. 5-11 shows the morphologies of 10SiZGC and 10SiZC after 500 cycles at 1 A $g^{-1}$. From the TEM image, EDS mappings, and the upper right inset in Fig. 5-11a, we can see that the overall architecture of ZIF in 10SiZGC after cycling is preserved and Si particles are still encapsulated within ZIF glass. Fig. 5-11b exhibits the HRTEM images and the selected area electron diffraction (SAED) patterns of 10SiZGC after 500 cycles. Clearly, this sample demonstrates a large amount of amorphous phase and a few crystals with a size of 10~20 nm. The lattice fringes with an interplanar spacing of ~0.31 nm is attributed to Si. Figs. 5-11c, d show the TEM image, EDS mappings,

HRTEM image, and the SAED pattern of 10SiZC after 500 cycles. Obviously, the cycled 10SiZC exhibits a similar scenario as 10SiZGC, i.e., a large amount of amorphous phase and a few Si crystals. These results suggest that ZIF crystals in 10SiZC and the majority of Si in both samples are converted into amorphous states after 500 cycles due to the insertion/extraction of $Li^+$.

### 5.3.2. CYCLIC VOLTAMMETRY CURVE

The CV curves of 10SiZGC after 500 charging/discharging cycles are shown in Fig. 5-12. Compared with the redox peaks in the CV curves of pristine 10SiZGC (Fig. 5-7), a new pair of redox peaks, arising from the insertion/extraction of $Li^+$ into/from ZIF glass [77], appear in the cycled sample, i.e., (1.69 vs 1.91 V). This indicates that as the charging/discharging cycle number increases, ZIF glass is gradually activated for lithium storage, contributing to the enhancement of the capacity of the composite. In addition, the peak at 0.12 V corresponding to the alloying of $Li^+$ with Si in the second cathodic curve in pristine 10SiZGC (Fig. 5-7) is not observed in the cycled sample (Fig. 5-12). These results implies that the structure of both ZIF glass and Si changes with cycling.

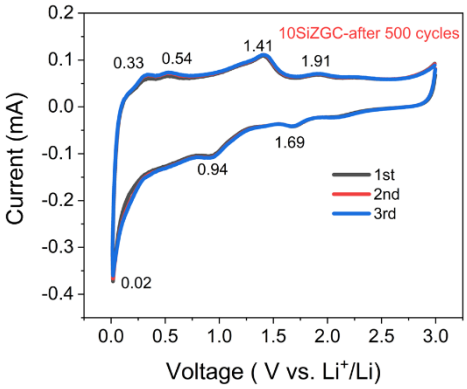


*Fig. 5-12 Cyclic Voltammetry (CV) curves of 10SiZGC after 500 cycles within the range from 0.01 to 3.0 V at a scan rate of 0.1mV $s^{-1}$.*

### 5.3.3 ELECTROCHEMICAL IMPEDANCE SPECTRA

Fig. 5-13a shows the EIS curves of 10SiZC and 10SiZGC after 500 cycles. Clearly, different from the Nyquist plots of 10SiZC and 10SiZGC before cycling (Fig. 5-8), two depressed semicircles arising from $R_s$ along with $C_{PE1}$ and $R_{ct}$ with $C_{PE2}$, respectively, appear in the high-frequency region. The equivalent circuit for the Nyquist plots is given in the inset. The charge transfer resistance ($R_{ct}$) of 10SiZGC and 10SiZC decreases from 405.3 and 290.4 Ω (Fig. 5-8) to 10.8 and 29.7 Ω after 500 cycles, respectively, suggesting the increased electrical conductivity. The diffusion impedance ($Z_w$) and Warburg factor ($\sigma$) can be determined from the inclined line in

the low-frequency region and the linear relation between impedance Z′ and the reciprocal square root of the angular frequency $\omega$, respectively. The $\sigma$ values of 10SiZC and 10SiZGC before and after cycling are shown in Fig. 5-13b. Clearly, upon cycling, the $\sigma$ values of 10SiZC and 10SiZGC drop from 191.78 and 320.88 to 32.36 and 14.16, respectively, suggesting an increased $Li^+$ diffusion coefficient [20, 78]. The EIS results indicate that both the electron transfer rate and $Li^+$ diffusion coefficient of 10SiZC and 10SiZGC are greatly enhanced by cycling.

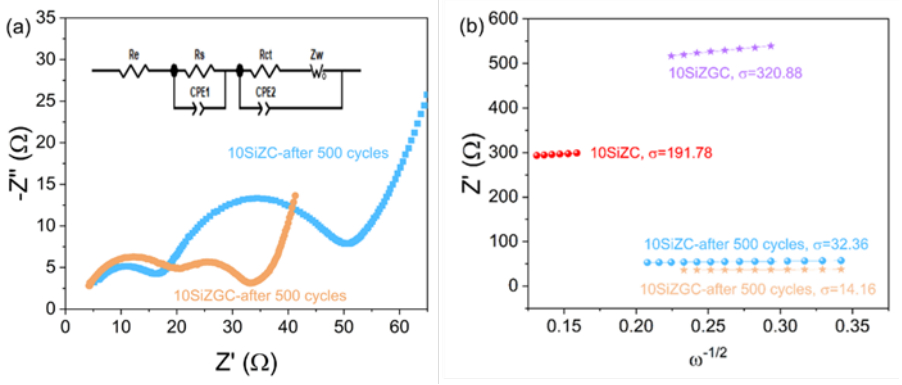


*Fig. 5-13 (a) Nyquist plots of 10SiZC and 10SiZGC after cycling obtained from electrochemical impedance spectra within the frequency range from 0.01 Hz to 100 kHz. (b) The dependence of Z′ on $\omega^{-1/2}$ in the low-frequency region obtained from Nyquist plots in Figs. 5-8, 5-13a.*

## 5.4. PROPOSED MECHANISM

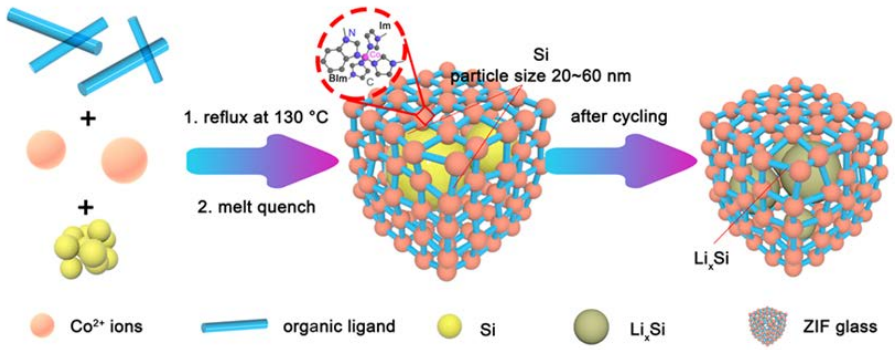


*Fig. 5-14 The protecting role of ZIF glass matrix, which prolongs the cycling life of Si.*

Based on the above results, the enhanced capacity of the Si@ZIF-glass composite compared with pure Si, ZIF crystal/glass and Si@ZIF-crystal composite is associated with the synergistic effects of ZIF glass layer and the wrapped nano-Si particles in

lithium storage. In detail, compared to crystalline counterparts, cobalt-ZIF-62 glass has an open disordered network structure that offers more active sites and channels for $Li^+$ storage and transfer. In addition, the volume changes of the encapsulated Si can be buffered by the ZIF glass layer during charging/discharging process. This is because that on the one hand, ZIF glass layer in the composite stores some $Li^+$ itself, leading to fewer $Li^+$ ions entering the inner surface of ZIF and reacting with wrapped Si, i.e., the alloying of $Li^+$ with wrapped Si is suppressed to some extent. On the other hand, ZIF layer can geometrically confine the volume expansion of Si during alloying, and thereby reducing the degree of pulverization of Si in the composite. Even if the encapsulated Si is pulverized after cycling (as shown in 5-14), a large amount of Si is still attached to the inner surface of ZIF glass, and thus the composite structure can maintain good electrical contact with the copper current collector. Such good contact ensures electron transfer and hence the alloying between $Li^+$ and Si. Moreover, the $Li^+$ insertion/extraction could cause the distortion and breakage of aromatic rings and Co-N in ZIF, increasing structural defects and thus diffusion channels for $Li^+$ [20, 79]. The increased channels lead to more $Li^+$ ions going into ZIF and alloying with Si, thereby enhancing the reversible capacity and rate capability.

## 5.5. SUMMARY

In this chapter, we fabricated Si@ZIF-glass composites for lithium storage by combining the reflux and melt-quenching methods (more detail can be seen in Paper II). The composite based anode yields a strong synergistic effect and delivers a capacity up to 650 mA h $g^{-1}$ at the current density of 1 A $g^{-1}$ after 500 cycles. This capacity is more than three times that of ZIF glass, six times that of ZIF crystal, and thirty times that of pure Si. The structural origin of this enhanced electrochemical performance of composites has been revealed. In detail, first, the open disordered network structure of ZIF glass is beneficial for the transport and storage of $Li^+$. Second, the existence of the ZIF glass layer buffers the volume expansion and pulverization of Si, so that Si can give full play to the advantages of high specific capacity. Third, the composite structure remains in good contact with the current collector, and thus ensures the transport of electrons and reversible reactions during the charge and discharge process. Our approach to constructing hierarchical Si@ZIF-glass composite could be further extended to other types of ZIF glasses and highly active materials for application in electrochemical energy storage.

# CHAPTER 6. GENERAL DISCUSSIONS

Since the electrochemical performances of glass-based materials are associated with their composition, microscopic structure, prepare process, it is critical to understand composition-structure-process-performance relations for different glass systems. For both oxide glass and metal-organic framework (MOF) glass, a different fraction of doping Si affects the performances of Si/vanadium tellurite glass (VT) composites and Si@ZIF-glass (a subset of MOF) composites. By optimizing the Si fraction, i.e., 10 wt.%, Si-glass composite-based anodes exhibit superior capacity, cycling stability, and rate performance.

As one of the most important features of glasses, structural disorder plays a crucial role in their properties and functionalities. The structure of oxide glasses features short-range order, which involves polyhedral units such as $VO_4$, $VO_5$, $TeO_3$, etc., and medium-range order, but long-range disorder. In contrast, the short-range structure of MOF glasses is disordered, since it has a lower rigidity and larger size of the tetrahedral units in MOF compared [20, 26]. The long-range or short-range disordered structures exhibit open networks with larger free volumes than crystals, which are beneficial for lithium-ion diffusion and storage. Therefore Si@ZIF-glass composite (SiZGC) and VTS-620-HP anodes exhibit better electrochemical performances than Si@ZIF-crystal composite (SiZC) and VTS-670/770-HP anodes, respectively. In addition, for VT glass, when the glass was heat-treated above its $T_g$, which is related to glass network connectivity, bond strength etc., glass can act as a binder to combine with Si as it demonstrates viscous fluidity above $T_g$.

The preparation process can affect the composition and structure of materials and thus change the performances. For VT glass system, the introduction of Si and heating of the mixture (VTS) at different temperatures above $T_g$ cause the redox reaction between Si and VT to form $SiO_2$ and $V^{4+}$. The existence of $V^{4+}$ could facilitate the electrical conductivity in VT glass. This is because during the discharging process, polarons formed due to the electron-phonon interaction, and thus efficient charge transfer can be realized by polaron-hopping on medium-range $V^{4+}$–O–$V^{5+}$ chains ($V^{4+}$–O–$V^{5+}$→$V^{5+}$–O–$V^{4+}$) [59]. However, $SiO_2$ can decrease electrical conductivity as it is an insulating material. Therefore, to achieve high electrical conductivity of VTS, a compromise ratio between $V^{4+}$ and $SiO_2$ should be considered. In addition, the redox reaction affects the crystallization of VTS. In detail, on the one hand, the reaction that occurred in VTS suppresses the precipitation of $Te_2V_2O_9$ crystals compared with VT owing to the energy consumed for the redox reaction. On the other hand, new $TeVO_4$ crystals appear due to the redox reaction between Si and VT, leading to compositional variations. The VTS sample with some crystals, namely glass-ceramic, contains both disordered and ordered domains. Although the formation of an ordered zone reduces the open networks of glass, new channels between glass and crystals can be generated for ion diffusion beneficial for electrochemical

performances. Moreover, when using the hot-pressing method to prepare samples, Si nanoparticles were embedded into the VT matrix, which could not be achieved by traditional heat treatment. The insertion of Si into the VT matrix stabilizes the Si particles during lithiation, and hence the VTS composites yield good synergistic effects (a combination of high capacity and good cycling stability).

As for Si@ZIF-glass system, Si nanoparticles were encapsulated into ZIF glass by combining the reflux and melt-quenching methods. As a result, a robust hierarchical structure was constructed, which demonstrates a strong synergistic effect. The unique architecture in ZIF glass prevents the aggregation of nano Si particles and buffers the volume changes of Si, hence promoting the transport kinetics for both electrons and lithium ions. In addition, ZIF glass itself also enhanced the electrochemical performance of Si@ZIF-glass based anode owing to its open network structure that facilitates the $Li^+$ ion diffusion and storage, leading to better performances than pristine Si, ZIF glass, ZIF crystal and Si@ZIF-crystal counterparts.

In short, to obtain glass-based composite anodes with good electrochemical performances, the following aspects should be considered:

1) The glass system and the fraction of doping Si (composition). Choosing glass that is semi-conductive or conductive. This is because good electronic conductivity is essential for anode materials but most inorganic and ZIF glasses show low electronic conductivities. In addition, since both VT glass and ZIF glass show limited accommodation ability of Si, excessive Si can bring negative effects, e.g., extra Si not only cannot be protected by glass matrix but also hinder the transport of $Li^+$ to glasses. Therefore, it is important to find the optimal fraction of doping Si.

2) $SiO_2$ vs. $V^{4+}$, crystals vs. glass (composition and structure). For VTS system, a redox reaction occurred during heating, i.e., Si reduces $V^{5+}$ and form $SiO_2$ and $V^{4+}$. $SiO_2$ and $V^{4+}$–O–$V^{5+}$ chains demonstrate opposite effects on electrical conductivity. Thus, a compromise between $SiO_2$ and $V^{4+}$ content is crucial. In addition, although glass-ceramics generated new channels between glass and crystals for ion diffusion, the glass anodes with disordered networks are superior to their crystal and glass-ceramic counterparts. This is verified by the excellent electrochemical performances of 10VTS-620-HP and 10SZGC, in which the matrices are only glass.

3) Whether Si volume change can be buffered by glass matrix (preparing process and architecture). For VT glass, the strategy to buffer Si volume change is to embed Si into VT matrix. When VTS composites are prepared by traditional heat-treatment, it is difficult to realize this goal. However, Si can be embedded into VT matrix by the hot-pressing method and achieve good performances. For ZIF glass, the approach to buffer Si volume fluctuation is to wrap Si into ZIF glass layers by combing reflux and melt-quenching methods. Using the facile method not only realized the goal but also doubled the yields of ZIF glass.

# CHAPTER 7. CONCLUSIONS AND PERSPECTIVES

## 7.1. CONCLUSIONS

Although glassy materials have received growing attention due to their compositional, structural and performance advantages compared with their crystalline counterparts, their application potential in energy storage, especially in LIBs, are still needed to be fulfilled. There are a few reports about using VT glasses and MOF glasses as anodes for LIBs, exhibiting excellent cycling stability. However, the capacities of these glass anodes need to be improved. To solve this problem, we combined glasses with Si, which has ultrahigh theoretical capacity but poor cycling stability due to the volume expansion during discharging and contraction during charging, to make full use of the advantages of both materials. Therefore, one of the main points of this thesis is to explore how they can combine effectively and yield synergistic effects. In detail, three synthesis methods for combining glasses (VT glass or MOF glass) with Si and forming Si-glass composites are investigated and explored: (1) the Si/VT composites obtained by the conventional heat-treatment method (Chapter 3); (2) the Si/VT composites prepared by hot pressing method (Chapter 4); (3) the Si@ZIF-glass composites synthesized by reflux and melt-quenching method (Chapter 5). Moreover, as another main point of this thesis, the composition-structure-process-performance relations are studied. Highlights are presented as follows:

For the VT glass system, we prepared Si/VT composites through two methods, i.e., conventional heat-treatment and hot-pressing methods. The hot-pressing is verified as an effective approach to combine Si and VT. We investigated the compositions, structures, morphologies, and electrochemical performances of the composites after different heating temperatures. It is found that 10VTS-620-HP sample, i.e., doping 10 wt.% Si into VT matrix and hot pressing at 620K, exhibits better electrochemical performances (408 mA h $g^{-1}$ at 1A $g^{-1}$ after 1000 cycles) than other samples with different Si fraction and hot-pressing temperatures. The origin of the high capacity of this sample was revealed. First, 10 wt.% of doping Si is an optimal fraction to embed into VT matrix as the glass has a limited ability to accommodate Si nanoparticles. Second, the hot-pressing temperature for VTS, i.e., 620K, not only preserves the disordered open network of VT glass, but also ensures a proper amount of $V^{4+}$ generated by the redox reaction between Si and $V^{5+}$, resulting in both good Li-ion diffusion and electron transfer. Third, both the hot-pressing temperature and pressure, i.e., 620K and 100 MPa, guarantee enough viscous fluidity of the glass and sufficient driving force to embed Si into the glass matrix. Therefore, the volume expansion of Si can be buffered by the VT glass matrix during discharging. In summary, a synergistic effect can be achieved of Si and VT by hot-pressing method, leading to better electrochemical performances.

For the ZIF glass system, Si@ZIF-glass composites (SiZGCs) were synthesized by combining the reflux and melt-quenching methods. The 10SiZGC anode demonstrates a capacity of 650 mA h $g^{-1}$ at 1 A $g^{-1}$ after 500 cycles, which is higher than pure ZIF crystal, ZIF glass, Si, and Si@ZIF-crystal composites (SiZCs). The origin of high capacity of 10SiZGC was revealed by performing structural and morphological analyses before and after cycling. First, like VT glass, ZIF glass also has a limited capability to wrap Si, and 10 wt.% of doping Si is proved to be the optimal fraction. Second, ZIF glass possesses an open disordered network structure and weaker Co-N and aromatic rings, which involve more active sites and channels for both storage and transport of $Li^+$ compared to their crystalline counterparts. Third, the volume changes of Si can be buffered by ZIF glass layers during the charging/discharging cycling. Fourth, the insertion/extraction of $Li^+$ could result in the distortion or breakage of Co-N and aromatic rings in ZIF, leading to an increase in structural defects and diffusion channels for the transport and storage of $Li^+$. Finally, the increased channels lead to more $Li^+$ ions going into ZIF and reacting with Si, thereby achieving a strong synergistic effect, and exhibiting excellent reversible capacity, rate capability and cycling stability.

To sum up, we proposed and implemented the effective strategies of combining Si with oxide glass and MOF glass and thereby produced two promising glass-based LIB anode materials, which may have better compatibility with glass/glass-ceramic solid-state electrolytes than traditional anode materials. In addition, our approach could be further extended to other types of oxide and MOF glasses to combine with other highly active materials like Sn and $SnO_2$ for energy storage.

## 7.2. PERSPECTIVES

The outcomes of this thesis shed light on the development of glass-based materials for LIBs, while the following research topics are still in need of further investigation.

The lithium storage mechanism of VT glass is still not fully clarified. Future experiments and analyses are needed to elucidate the process. Some studies have reported the Li-ion storage mechanism of $V_2O_5$ crystals, i.e., Li ions intercalate into the layered space of the $V_2O_5$ crystalline structure forming $Li_xV_2O_5$ ($0<x\leq3$) and then de-intercalate [80, 81]. However, there is still no direct evidence to prove whether the layered space is preserved or partially preserved in vanadium-tellurite glass and the intercalation/deintercalation mechanism [18, 19]. Therefore, more advanced characterization technologies, such as *in-situ* XRD, *in-situ* NMR, etc., are urgently needed to explore the actual lithium storage mechanism in VT glass.

Similarly, the lithium storage mechanisms of MOF crystals and glasses are still uncertain. Scientists have proposed a possible mechanism for MOF crystals that carboxylate group from organic ligands could react with $Li^+$ ions to give reversible capacity [82, 83]. However, there is still no direct evidence to prove this insertion

mechanism. In addition, for Si@MOF composites, it is still unknown the main insertion sites of $Li^+$, i.e., at the interfaces of Si and MOF or Si within MOF layers. Therefore, further experiments and analyses are necessary.

Moreover, the reason why ZIF glass-based anodes exhibit gradually increasing capacity and experience order-disorder transition along with cycling is debatable. In addition, the origin of these growing capacities lacks solid evidence. Thus, the structure-performance relation of ZIFs should be further clarified.

Furthermore, our approaches to combining Si and VT/ZIF glass materials need to be expanded to other highly active materials and glass systems, thereby broadening the application fields of such composites. In addition, as all solid-state batteries are the development trend, it would be attractive to assemble glass-based electrodes with the currently best-performing solid-state electrolytes (glass/glass-ceramic) into all-solid-state batteries.

# BIOGRAPHY

[1] V. Shrivastav, S. Sundriyal, P. Goel, H. Kaur, S.K. Tuteja, K. Vikrant, K.H. Kim, U.K. Tiwari, A. Deep, Metal-organic frameworks (MOFs) and their composites as electrodes for lithium battery applications: Novel means for alternative energy storage, Coord. Chem. Rev. 393 (2019) 48-78.

[2] M.M. Kabir, D.E. Demirocak, Degradation mechanisms in Li-ion batteries: a state-of-the-art review, International Journal Of Energy Research 41(14) (2017) 1963-1986.

[3] S. Chae, S.H. Choi, N. Kim, J. Sung, J. Cho, Integration of graphite and silicon anodes for the commercialization of high-energy lithium-ion batteries, Angew. Chem. Int. Ed. Engl. 59(1) (2020) 110-135.

[4] J.B. Goodenough, K.-S. Park, The Li-ion rechargeable battery: a perspective, J. Am. Chem. Soc. 135(4) (2013) 1167-1176.

[5] Y.S. Tian, G.B. Zeng, A. Rutt, T. Shi, H. Kim, J.Y. Wang, J. Koettgen, Y.Z. Sun, B. Ouyang, T.N. Chen, Z.Y. Lun, Z.Q. Rong, K. Persson, G. Ceder, Promises and challenges of next-generation "beyond Li-ion" batteries for electric vehicles and grid decarbonization, Chem. Rev. 121(3) (2021) 1623-1669.

[6] J. Lu, Z.W. Chen, F. Pan, Y. Cui, K. Amine, High-performance anode materials for rechargeable lithium-ion batteries, Electrochemical Energy Reviews 1(1) (2018) 35-53.

[7] J.B. Goodenough, Cathode materials: A personal perspective, J. Power Sources 174(2) (2007) 996-1000.

[8] Y. Ding, Z.P. Cano, A. Yu, J. Lu, Z. Chen, Automotive Li-ion batteries: current status and future perspectives, Electrochemical Energy Reviews 2(1) (2019) 1-28.

[9] W. Hou, X. Guo, X. Shen, K. Amine, H. Yu, J. Lu, Solid electrolytes and interfaces in all-solid-state sodium batteries: Progress and perspective, Nano Energy 52 (2018) 279-291.

[10] J. Souquet, Glasses as electrolytes and electrode materials in lithium batteries, J. Power Sources 26(1-2) (1989) 33-35.

[11] R. Chen, W. Qu, X. Guo, L. Li, F. Wu, The pursuit of solid-state electrolytes for lithium batteries: from comprehensive insight to emerging horizons, Materials Horizons 3(6) (2016) 487-516.

[12] K. Kaup, J.D. Bazak, S.H. Vajargah, X. Wu, J. Kulisch, G.R. Goward, L.F. Nazar, A lithium oxythioborosilicate solid electrolyte glass with superionic conductivity, Adv. Energy Mater. 10(8) (2020) 1902783.

[13] X. Wu, Z. Wang, L. Chen, X. Huang, Ag-enhanced SEI formation on Si particles for lithium batteries, Electrochem. Commun. 5(11) (2003) 935-939.

[14] Y. Huang, Y. Fang, X.F. Lu, D. Luan, X.W. Lou, $Co_3O_4$ hollow nanoparticles embedded in mesoporous walls of carbon nanoboxes for efficient lithium storage, Angew. Chem. 132(45) (2020) 20086-20090.

[15] Y. Idota, T. Kubota, A. Matsufuji, Y. Maekawa, T. Miyasaka, Tin-based amorphous oxide: a high-capacity lithium-ion-storage material, Science 276(5317) (1997) 1395-1397.

[16] S.-M. Paek, E. Yoo, I. Honma, Enhanced cyclic performance and lithium storage capacity of SnO2/graphene nanoporous electrodes with three-dimensionally delaminated flexible structure, Nano Lett. 9(1) (2009) 72-75.

[17] J. Liu, M. Cheng, T. Han, Q. Lu, H. Zhang, P. Zhou, Y. Ni, J. Li, A novel mechanically robust leaf-shaped tin dioxide Li-ion battery anode and its dynamic structural transformation and electron‐transfer simulation, Energy Technology 8(5) (2020) 1901149.

[18] Y. Zhang, P. Wang, T. Zheng, D. Li, G. Li, Y. Yue, Enhancing Li-ion battery anode performances via disorder/order engineering, Nano Energy 49 (2018) 596-602.

[19] Y.F. Zhang, P.X. Wang, G.D. Li, J.H. Fan, C.W. Gao, Z.Y. Wang, Y.Z. Yue, Clarifying the charging induced nucleation in glass anode of Li-ion batteries and its enhanced performances, Nano Energy 57 (2019) 592-599.

[20] C. Gao, Z. Jiang, S. Qi, P. Wang, L.R. Jensen, M. Johansen, C.K. Christensen, Y. Zhang, D.B. Ravnsbæk, Y. Yue, Metal-organic framework glass anode with an exceptional cycling-induced capacity enhancement for lithium‐ion batteries, Adv. Mater. 34(10) (2022) 2110048.

[21] Y. Jiang, D. Zhang, Y. Li, T. Yuan, N. Bahlawane, C. Liang, W. Sun, Y. Lu, M. Yan, Amorphous $Fe_2O_3$ as a high-capacity, high-rate and long-life anode material for lithium ion batteries, Nano Energy 4 (2014) 23-30.

[22] C. Gao, P. Wang, Z. Wang, S.K. Kær, Y. Zhang, Y. Yue, The disordering-enhanced performances of the Al-MOF/graphene composite anodes for lithium ion batteries, Nano Energy 65 (2019) 104032.

[23] T. Wei, M. Zhang, P. Wu, Y.-J. Tang, S.-L. Li, F.-C. Shen, X.-L. Wang, X.-P. Zhou, Y.-Q. Lan, POM-based metal-organic framework/reduced graphene oxide nanocomposites with hybrid behavior of battery-supercapacitor for superior lithium storage, Nano Energy 34 (2017) 205-214.

[24] X. Li, F. Cheng, S. Zhang, J. Chen, Shape-controlled synthesis and lithium-storage study of metal-organic frameworks $Zn_4O$ (1,3,5-benzenetribenzoate)$_2$, J. Power Sources 160(1) (2006) 542-547.

[25] T.D. Bennett, J.-C. Tan, Y. Yue, E. Baxter, C. Ducati, N.J. Terrill, H.H.-M. Yeung, Z. Zhou, W. Chen, S. Henke, Hybrid glasses from strong and fragile metal-organic framework liquids, Nature Communications 6(1) (2015) 1-7.

[26] R.S. Madsen, A. Qiao, J. Sen, I. Hung, K. Chen, Z. Gan, S. Sen, Y. Yue, Ultrahigh-field $^{67}$Zn NMR reveals short-range disorder in zeolitic imidazolate framework glasses, Science 367(6485) (2020) 1473-1476.

[27] A. Qiao, T.D. Bennett, H. Tao, A. Krajnc, G. Mali, C.M. Doherty, A.W. Thornton, J.C. Mauro, G.N. Greaves, Y. Yue, A metal-organic framework with ultrahigh glass-forming ability, Science advances 4(3) (2018) eaao6827.

[28] L. Frentzel-Beyme, M. Kloß, R. Pallach, S. Salamon, H. Moldenhauer, J. Landers, H. Wende, J. Debus, S. Henke, Porous purple glass–a cobalt imidazolate glass with accessible porosity from a meltable cobalt imidazolate framework, J. Mater. Chem. A 7(3) (2019) 985-990.

[29] R. Banerjee, A. Phan, B. Wang, C. Knobler, H. Furukawa, M. O'Keeffe, O.M. Yaghi, High-throughput synthesis of zeolitic imidazolate frameworks and application to $CO_2$ capture, Science 319(5865) (2008) 939-943.

[30] D.H.S. Tan, Y.-T. Chen, H. Yang, W. Bao, B. Sreenarayanan, J.-M. Doux, W. Li, B. Lu, S.-Y. Ham, B. Sayahpour, J. Scharf, E. A.Wu, G. Deysher, H.E. Han, H.J. Hah, H. Jeong, J.B. Lee, Z. Chen, Y.S. Meng, Carbon-free high-loading silicon anodes enabled by sulfide solid electrolytes, Science 373 (2021) 1494-1499.

[31] Y. Zhang, J. Ren, T. Xu, A. Feng, K. Hu, N. Yu, Y. Xia, Y. Zhu, Z. Huang, G. Wu, Covalent bonding of Si nanoparticles on graphite nanosheets as anodes for lithium-ion batteries using diazonium chemistry, Nanomaterials 9(12) (2019) 1741.

[32] Y. Xu, Y. Zhu, C. Wang, Mesoporous carbon/silicon composite anodes with enhanced performance for lithium-ion batteries, J. Mater. Chem. A 2(25) (2014) 9751-9757.

[33] D.H. Tan, Y.-T. Chen, H. Yang, W. Bao, B. Sreenarayanan, J.-M. Doux, W. Li, B. Lu, S.-Y. Ham, B. Sayahpour, Carbon-free high-loading silicon anodes enabled by sulfide solid electrolytes, Science 373(6562) (2021) 1494-1499.

[34] S. Sakida, S. Hayakawa, T. Yoko, $^{125}$Te and $^{51}$V static NMR study of $V_2O_5$-$TeO_2$ glasses, Journal of Physics-Condensed Matter 12(12) (2000) 2579-2595.

[35] M.I. Aroyo, J.M. Perez-Mato, C. Capillas, E. Kroumova, S. Ivantchev, G. Madariaga, A. Kirov, H. Wondratschek, Bilbao crystallographic server: I. Databases and crystallographic computing programs, Zeitschrift Fur Kristallographie 221(1) (2006) 15-27.

[36] M.I. Aroyo, A. Kirov, C. Capillas, J. Perez-Mato, H. Wondratschek, Bilbao Crystallographic Server. II. Representations of crystallographic point groups and space groups, Acta Crystallogr. Sect. A: Found. Crystallogr. 62(2) (2006) 115-128.

[37] C.J. Fontenot, J.W. Wiench, G.L. Schrader, M. Pruski, $^{17}$O MAS and 3QMAS NMR investigation of crystalline $V_2O_5$ and Layered $V_2O_5 \cdot nH_2O$ Gels, J. Am. Chem. Soc. 124(28) (2002) 8435-8444.

[38] M. Vergniory, L. Elcoro, C. Felser, N. Regnault, B.A. Bernevig, Z. Wang, A complete catalogue of high-quality topological materials, Nature 566(7745) (2019) 480-485.

[39] M.I. Aroyo, J. Perez-Mato, D. Orobengoa, E. Tasci, G. de la Flor, A. Kirov, Crystallography online: Bilbao crystallographic server, Bulg. Chem. Commun 43(2) (2011) 183-197.

[40] B. Bradlyn, L. Elcoro, J. Cano, M. Vergniory, Z. Wang, C. Felser, M. Aroyo, B.A. Bernevig, Topological quantum chemistry, Nature 547(7663) (2017) 298-305.

[41] D.S. Jensen, S.S. Kanyal, N. Madaan, M.A. Vail, A.E. Dadson, M.H. Engelhard, M.R. Linford, Silicon (100)/$SiO_2$ by XPS, Surf. Sci. Spectra 20(1) (2013) 36-42.

[42] G. Silversmit, D. Depla, H. Poelman, G.B. Marin, R. De Gryse, An XPS study on the surface reduction of $V_2O_5$ (0 0 1) induced by $Ar^+$ ion bombardment, Surf. Sci. 600(17) (2006) 3512-3517.

[43] M. Taha, S. Walia, T. Ahmed, D. Headland, W. Withayachumnankul, S. Sriram, M. Bhaskaran, Insulator–metal transition in substrate-independent $VO_2$ thin film for phase-change devices, Scientific reports 7(1) (2017) 1-10.

[44] P. Pena, J.R. Mercury, A. De Aza, X. Turrillas, I. Sobrados, J. Sanz, Solid-state $^{27}Al$ and $^{29}Si$ NMR characterization of hydrates formed in calcium aluminate–silica fume mixtures, J. Solid State Chem. 181(8) (2008) 1744-1752.

[45] J.G. Xu, X.M. Wang, H. Fu, C.M. Brown, X.P. Jing, F.H. Liao, F.Q. Lu, X.H. Li, X.J. Kuang, M.M. Wu, Solid-state $^{29}Si$ NMR and Neutron-diffraction studies of $Sr_{0.7}K_{0.3}SiO_{2.85}$ oxide ion conductors, Inorg. Chem. 53(13) (2014) 6962-6968.

[46] E. Boivin, J.-N. Chotard, C. Masquelier, L. Croguennec, Towards reversible high-voltage multi-electron reactions in alkali-ion batteries using vanadium phosphate positive electrode materials, Molecules 26(5) (2021) 1428.

[47] I. Joni, L. Nulhakim, M. Vanitha, C. Panatarani, Characteristics of crystalline silica ($SiO_2$) particles prepared by simple solution method using sodium silicate ($Na_2SiO_3$) precursor, Journal of Physics: Conference Series, IOP Publishing, 2018, p. 012006.

[48] S. Rada, E. Culea, V. Rus, M. Pica, M. Culea, The local structure of gadolinium vanado-tellurite glasses, J. Mater. Sci. 43(10) (2008) 3713-3716.

[49] W. Yang, W. Huang, Q. Zheng, W. Huang, Z. Chen, High efficiency preparation, structure and properties of silicon nano-crystals by induction plasma method, NanoWorld J 2(3) (2016) 63-68.

[50] Y. Saddeek, I. Yahia, W. Dobrowolski, L. Kilanski, N. Romcevic, M. Arciszewska, Infrared, Raman spectroscopy and ac magnetic susceptibility of $Gd_2O_3$-$TeO_2$-$V_2O_5$ glasses, optoelectronics and advanced materials-rapid communications 3 (2009) 559-564.

[51] K. Shafeeq, V. Athira, C.R. Kishor, P. Aneesh, Structural and optical properties of $V_2O_5$ nanostructures grown by thermal decomposition technique, Appl. Phys. A 126(8) (2020) 1-6.

[52] A. Rahim, A. Arof, Spectroscopic studies of $V_2O_5$–$Bi_2O_3$–$TeO_2$ glasses, Optical and Quantum Electronics 48(4) (2016) 238.

[53] T. Srikumar, C.S. Rao, Y. Gandhi, N. Venkatramaiah, V. Ravikumar, N. Veeraiah, Microstructural, dielectric and spectroscopic properties of $Li_2O$–$Nb_2O_5$–$ZrO_2$–$SiO_2$ glass system crystallized with $V_2O_5$, Journal of Physics and Chemistry of Solids 72(3) (2011) 190-200.

[54] V. Murgia, E.M.F. Torres, J.C. Gottifredi, E.L. Sham, Sol–gel synthesis of $V_2O_5$–$SiO_2$ catalyst in the oxidative dehydrogenation of n-butane, Applied Catalysis A: General 312 (2006) 134-143.

[55] W. Chen, J. Peng, L. Mai, H. Yu, Y. Qi, Synthesis and characterization of novel vanadium dioxide nanorods, Solid State Commun. 132(8) (2004) 513-516.

[56] M.M. Islam, M.A. Rashid, M.P. Ahamed, M.E. Hossain, M.R. Ahsan, M.G. Mortuza, M.H.K. Rubel, Morphogenesis of silicovanadate glasses: investigation of physical properties, Journal of Engineering Advancements (2021) 78-86.

[57] H. Ji, D. Liu, H. Cheng, C. Zhang, L. Yang, D. Ren, Infrared thermochromic properties of monoclinic $VO_2$ nanopowders using a malic acid-assisted hydrothermal method for adaptive camouflage, RSC advances 7(9) (2017) 5189-5194.

[58] X. Wu, Z. Wu, C. Ji, H. Feng, X. Ma, Y. Su, Y. Zhou, J. Wang, Y. Jiang, Influence of infrared optical properties by transformation of the crystal structure in Al-doped vanadium dioxide films, Optical Materials Express 6(11) (2016) 3500-3506.

[59] J. Yan, T. Zhao, N. Shi, H. Zhan, J. Ren, Y. Zhang, Y. Yue, Impact of silicon doping on the structure and crystallization of a vanadium-tellurite glass, J. Non-Cryst. Solids 589 (2022) 121651.

[60] C. O'Dwyer, V. Lavayen, S.B. Newcomb, M.A. Santa Ana, E. Benavente, G. Gonzalez, C.S. Torres, Vanadate conformation variations in vanadium pentoxide nanostructures, J. Electrochem. Soc. 154(8) (2007) K29.

[61] M.D. Kaya, B.C. Sertel, N.A. Sonmez, M. Cakmak, S. Ozcelik, Thickness-dependent physical properties of sputtered $V_2O_5$ films and Ti/$V_2O_5$/n-Si Schottky barrier diode, Appl. Phys. A 126(11) (2020) 1-11.

[62] S. Ashraf, R. Mehek, N. Iqbal, T. Noor, G. Ali, A. Wahab, A.A. Qayyum, A. Ahmad, ZIF 67 derived Co–Sn composites with N-doped nanoporous carbon as anode material for Li-ion batteries, Mater. Chem. Phys. 270 (2021) 124824.

[63] Y. Liu, X. Que, X. Wu, Q. Yuan, H. Wang, J. Wu, Y. Gui, W. Gan, ZIF-67 derived carbon wrapped discontinuous $Co_xP$ nanotube as anode material in high-performance Li-ion battery, Materials Today Chemistry 17 (2020) 100284. ¨

[64] B. Li, F. Yao, J.J. Bae, J. Chang, M.R. Zamfir, D.T. Le, D.T. Pham, H. Yue, Y.H. Lee, Hollow carbon nanospheres/silicon/alumina core-shell film as an anode for lithium-ion batteries, Sci Rep 5 (2015) 7659.

[65] A. Ulu, Metal–organic frameworks (MOFs): a novel support platform for ASNase immobilization, J. Mater. Sci. 55(14) (2020) 6130-6144.

[66] M. Mubashir, R. Ashena, A. Bokhari, A. Mukhtar, S. Saqib, A. Ali, R. Saidur, K.S. Khoo, H.S. Ng, F. Karimi, Effect of process parameters over carbon-based ZIF-

62 nano-rooted membrane for environmental pollutants separation, Chemosphere 291 (2022) 133006.

[67] S. Mala, L. Tsybeskov, D. Lockwood, X. Wu, J.-M. Baribeau, Raman scattering in Si/SiGe nanostructures: Revealing chemical composition, strain, intermixing, and heat dissipation, J. Appl. Phys. 116(1) (2014) 014305.

[68] C. Li, X. Lou, Q. Yang, Y. Zou, B. Hu, Remarkable improvement in the lithium storage property of Co2 (OH) 2BDC MOF by covalent stitching to graphene and the redox chemistry boosted by delocalized electron spins, Chem. Eng. J. 326 (2017) 1000-1008.

[69] W. An, B. Gao, S. Mei, B. Xiang, J. Fu, L. Wang, Q. Zhang, P.K. Chu, K. Huo, Scalable synthesis of ant-nest-like bulk porous silicon for high-performance lithium-ion battery anodes, Nature communications 10(1) (2019) 1-11.

[70] X. Hu, J. Jia, G. Wang, J. Chen, H. Zhan, Z. Wen, Reliable and General Route to Inverse Opal Structured Nanohybrids of Carbon‐Confined Transition Metal Sulfides Quantum Dots for High‐Performance Sodium Storage, Adv. Energy Mater. 8(25) (2018) 1801452.

[71] C. Hu, Y.-C. Huang, A.-L. Chang, M. Nomura, Amine functionalized ZIF-8 as a visible-light-driven photocatalyst for Cr (VI) reduction, J. Colloid Interface Sci. 553 (2019) 372-381.

[72] M. Morita, T. Ohmi, E. Hasegawa, M. Kawakami, M. Ohwada, Growth of native oxide on a silicon surface, J. Appl. Phys. 68(3) (1990) 1272-1281.

[73] I. Muzammil, Y. Li, M. Lei, Tunable wettability and pH-responsiveness of plasma copolymers of acrylic acid and octafluorocyclobutane, Plasma Processes and Polymers 14(10) (2017) 1700053.

[74] X. Chen, X. Wang, D. Fang, A review on C1s XPS-spectra for some kinds of carbon materials, Fullerenes, Nanotubes and Carbon Nanostructures 28(12) (2020) 1048-1058.

[75] S. Jurng, Z.L. Brown, J. Kim, B.L. Lucht, Effect of electrolyte on the nanostructure of the solid electrolyte interphase (SEI) and performance of lithium metal anodes, Energy & Environmental Science 11(9) (2018) 2600-2608.

[76] G. Khandelwal, N.P.M.J. Raj, S.-J. Kim, ZIF-62: a mixed linker metal–organic framework for triboelectric nanogenerators, J. Mater. Chem. A 8(34) (2020) 17817-17825.

[77] Y. Yu, C. Yue, X. Lin, S. Sun, J. Gu, X. He, C. Zhang, W. Lin, D. Lin, X. Liao, ZIF-8 cooperating in TiN/Ti/Si nanorods as efficient anodes in micro-lithium-ion-batteries, ACS Applied Materials & Interfaces 8(6) (2016) 3992-3999.

[78] X.L. Wu, Y.G. Guo, J. Su, J.W. Xiong, Y.L. Zhang, L.J. Wan, Carbon-nanotube-decorated nano-$LiFePO_4$@C cathode material with superior high-rate and low-temperature performances for lithium‐ion batteries, Adv. Energy Mater. 3(9) (2013) 1155-1160.

[79] Y. Lin, Q. Zhang, C. Zhao, H. Li, C. Kong, C. Shen, L. Chen, An exceptionally stable functionalized metal–organic framework for lithium storage, Chem. Commun. 51(4) (2015) 697-699.

[80] N. Wu, W. Du, G. Liu, Z. Zhou, H.-R. Fu, Q. Tang, X. Liu, Y.-B. He, Synthesis of hierarchical sisal-like $V_2O_5$ with exposed stable {001} facets as long life cathode materials for advanced lithium-ion batteries, ACS applied materials & interfaces 9(50) (2017) 43681-43687.

[81] L. Mai, Q. An, Q. Wei, J. Fei, P. Zhang, X. Xu, Y. Zhao, M. Yan, W. Wen, L. Xu, Nanoflakes-assembled three-dimensional hollow-porous $V_2O_5$ as lithium storage cathodes with high-rate capacity, Small 10(15) (2014) 3032-3037.

[82] M. Armand, S. Grugeon, H. Vezin, S. Laruelle, P. Ribière, P. Poizot, J.-M. Tarascon, Conjugated dicarboxylate anodes for Li-ion batteries, Nature materials 8(2) (2009) 120-125.

[83] S. Maiti, A. Pramanik, U. Manju, S. Mahanty, Reversible lithium storage in manganese 1,3,5-benzenetricarboxylate metal–organic framework with high capacity and rate performance, ACS applied materials & interfaces 7(30) (2015) 16357-16363.

# LIST OF PUBLICATIONS

**PUBLICATIONS IN PEER-REVIEW JOURNALS**

(1) **Yan J**, Zhang T, Tao H, Zhan H, Yue Y. Structure, crystallization, and performances of alkaline-earth boroaluminosilicate sealing glasses for SOFCs. *Journal of the American Ceramic Society*, 2021, 104: 2560–2570.

(2) **Yan J**, Zhao T, Shi N, Zhan H, Ren J, Zhang Y, Yue Y. Impact of silicon doping on the structure and crystallization of a vanadium-tellurite glass. *Journal of Non-Crystalline Solids*, 2022, 589: 121651

(3) **Yan J**, Gao C, Qi S, Jiang Z, Jensen LR, Zhan H, Zhang Y, Yue Y. Encapsulation of nano-Si into MOF glass to enhance lithium-ion battery anode performances. *Nano Energy*, 2022, 103: 107779.

(4) **Yan J**, Li X, Shi N, Ren X, Zhou H, Tao H, Ren J, Qiao A, Zhang Y, Yue Y. Optimizing vanadium-tellurite glass/Si composite as a superior anode for Li-ion batteries by hot pressing (to be submitted).

**ORAL AND POSTER PRESENTATIONS AT CONFERENCES**

(1) **Yan J**, Yue Y. Impact of Silicon Doping on the Structure and Crystallization of a Vanadium-Tellurite Glass. **Poster**: The International Year of Glass Symposium, Aalborg, Denmark (2022).

(2) **Yan J,** Yue Y. Structure and Performances of Boroaluminosilicate Sealing Glasses for Solid Oxide Fuel Cells. **Oral**: 26$^{th}$ International Congress on Glass (26 ICG), Berlin, Germany (2022).

(3) **Yan J,** Gao C, Zhang Y, Yue Y. Nano-Si@MOF glass composite for lithium-ion batteries. **Poster**: European Materials Research Society, Warsaw, Poland (2022).

# TEACHING ACTIVITIES

(1) Yue Y, Smedskjær M M, Yu D, **Yan J**. Course: Physical Chemistry of Materials (2021, 5 ECTS). Yan J gave three lectures accounting for 25% of the total class hours.

# Paper I

Journal of Non-Crystalline Solids 589 (2022) 121651

Contents lists available at ScienceDirect

Journal of Non-Crystalline Solids

journal homepage: www.elsevier.com/locate/jnoncrysol

# Impact of silicon doping on the structure and crystallization of a vanadium-tellurite glass

Jiajia Yan [a], Tongyao Zhao [b], Nian Shi [b], Hongbing Zhan [c], Jinjun Ren [b], Yanfei Zhang [d,*], Yuanzheng Yue [a,*]

[a] Department of Chemistry and Bioscience, Aalborg University, Fredrik Bajers Vej 7H, Aalborg DK-9220, Denmark
[b] Key Laboratory of Materials for High Power Laser, Shanghai Institute of Optics and Fine Mechanics, Chinese Academy of Sciences, Shanghai 201800, China
[c] College of Materials Science and Engineering, Fuzhou University, Fuzhou 350108, China
[d] School of Materials Science and Engineering, Qilu University of Technology (Shandong Academy of Sciences), Jinan 250353, China

ARTICLE INFO

*Keywords:*
$V_2O_5$-$TeO_2$ glass
Nano-silicon
Heat treatment
Silicon-glass interaction
Structural change
Crystallization

ABSTRACT

We studied the effect of silicon doping on the structure and crystallization behavior of $50V_2O_5$-$50TeO_2$ (mol%) (VT) glass by performing solid-state nuclear magnetic resonance (NMR), Fourier-transform infrared spectroscopy (FTIR), X-ray diffraction (XRD), and differential scanning calorimetry (DSC). We observed two interesting phenomena. First, when the mixture of glass and Si is heated in argon to 560 K ($1.1T_g$), Si starts to react with VT glass and is oxidized to amorphous silica, being confirmed by NMR and FTIR. Second, Si suppresses the formation of the $Te_2V_2O_9$ phase in VT glass during heating process up to 650 K (about $1.3T_g$), whereas it leads to the formation of the new crystalline phase $TeVO_4$ during heating to 725 K ($1.4T_g$). We discuss the origin of these two phenomena by considering the changes both in glass structure and in the redox reaction.

## 1. Introduction

It is known that silicon (Si) has high initial theoretical capacity (>4000 mA h/g) as anode material in Li-ion batteries (LIBs), but in reality, has not been applied since it undergoes a severe volume change during lithiation/delithiation, leading to a drastic decay of the capacity [1]. It is also known that vanadium-tellurite (VT) glasses are a promising anode material with higher cycling stability for LIBs, although it has lower capacity than Si [2,3]. The reason for the high cycling stability of VT glasses lies in their unique structure feature (e.g., not purely 3D tetrahedral network) that exhibits higher liquid fragility, semiconducting and stronger crystallization tendency upon heating compared to most of the conventional oxide glasses with tetrahedral network. During discharging/charging process, electrons can cause formation of polarons, and thus, high electronic conductivity can be realized by polaron-hopping in $V^{4+}$–O–$V^{5+}$ chains ($V^{4+}$–O–$V^{5+}$→$V^{5+}$–O–$V^{4+}$) [2,4]. The cycling ability of VT glass anode has been attributed to formation of the electrochemically active γ-$Li_3VO_4$ nanocrystals induced by insertion/extraction of Li ions. The nanocrystals lead to toughening of glass matrix and thereby increase the cycling stability. Thus, it is anticipated that the incorporation of nano Si into VT glass could lead to the synergetic effect, i.e., to both enhanced capacity and increased cycling stability of the anode for LIBs.

Here, the key question is whether the VT glass can buffer the volume change of Si during lithiation/delithiation and thereby suppress the decay of the anode performance if the two types of materials are properly combined. To answer this question, we need to investigate how they can be bonded together physically or chemically during heating process, and to find out how the Si-doping affects the crystallization behavior of VT glasses. To the best of our knowledge, such studies have not been reported in literature.

To conduct the above-mentioned investigations, we prepared the mixture of 10 wt% Si and 90 wt% VT glass using the physical mixing and subsequently sintering method. As is known, the heterogeneous nucleation in glass is easier to occur than the homogenous nucleation as the former has a lower nucleation energy barrier [5]. When nano-silicon powder is introduced into glass, the chemical heterogeneity and interfaces are created, and hence, the crystallization tendency is expected to be enhanced. The question is whether this common knowledge also applies to the impact of Si doping on the crystallization of VT glass. To

* Corresponding author.
* Corresponding author.
*E-mail addresses:* zhang-yanfei@hotmail.com (Y. Zhang), yy@bio.aau.dk (Y. Yue).

https://doi.org/10.1016/j.jnoncrysol.2022.121651
Received 19 February 2022; Received in revised form 14 April 2022; Accepted 15 April 2022
Available online 21 April 2022

**Table 1**
The detailed heat-treatment procedures of $50V_2O_5$-$50TeO_2$ glass powder (VT) and $50V_2O_5$-$50TeO_2$ glass doped with Si powder (VTS).

| Sample Name | Heat-Treatment Procedures | | |
|---|---|---|---|
| | 1st DSC upscan | 2nd DSC upscan | 3rd DSC upscan |
| VT-650 or VTS-650 | To 650 K | / | / |
| VT-650-2 or VTS-650-2 | To 650 K | To 650 K | / |
| VT-650-3 or VTS-650-3 | To 650 K | To 650 K | To 650 K |
| VT-650-725 or VTS-650-725 | To 650 K | To 725 K | / |
| VT-650-725-2 or VTS-650-725-2 | To 650 K | To 725 K | To 725 K |

do so, the mixed powder samples were heat-treated to different temperatures in argon (see Experimental section). The crystallization behavior is characterized by using the differential scanning calorimetry (DSC) and X-ray diffraction (XRD). The nature of bonding between Si nano powder and VT glass, as well as the structure changes of VT glass and Si upon crystallization were analyzed by performing the nuclear magnetic resonance (NMR) and Fourier-transform infrared spectroscopy (FTIR). We discussed the mechanism of the crystallization in the Si doped VT glass.

## 2. Experimental

The $50V_2O_5$-$50TeO_2$ (in mol %) glass prepared via the melt-quenching method [2] is chosen as the basic glass to composite with nano-Si. The $50V_2O_5$-$50TeO_2$ glass powder (VT) with a narrow size distribution between 5 and 10 μm was obtained by crushing and sieving the bulk sample. 100 mg commercial nano-silicon powder (about 20-60 nm particle size) was added into 0.9 g glass powder and then mixed thoroughly, which is referred to as VTS.

We conducted dynamic heat-treatment on both VT and VTS samples by the differential scanning calorimeter (DSC) (Jupiter 449C, Netzsch). Specifically, the VT and VTS were firstly subjected to a DSC upscan to 775 K at 10 K/min, respectively, to detect their thermal events, e.g., the glass transition temperature ($T_g$) and the crystallization onset temperature ($T_c$) (see Fig. S1). Based on this result, the new VT and VTS samples are upscanned to 545 K (a temperature just over the glass transition peak) and then downscanned at 10 K/min in argon to eliminate the glass thermal history. After that, different DSC scanning procedures were performed at the same heating and cooling rates of 10 K/min. VTS samples were upscanning to $T_g$ (509 K), $1.1T_g$ (560 K), $1.2T_g$ (610 K), $1.3T_g$ (≈650 K), $1.4T_g$ (≈725 K), $1.6T_g$ (815 K), $1.8T_g$ (916 K), $2T_g$ (1018 K), and $2.1T_g$ (1067 K), in order to study the temperature at which Si starts to react with VT glass. VT and VTS samples after upscanning to 650 K (a temperature between $T_{c2}$ and $T_{c3}$, which is denoted in Fig. S1), referred to as VT-650 and VTS-650, respectively, underwent the second and third DSC upscanning to investigate their crystallization behaviors. In detail, some VT-650 and VTS-650 samples were heat-treated to 650 K for the second and third upscans, others were upscanned to 725 K (a temperature between $T_{c3}$ and the melting peak, which is denoted in Fig. S1) for the second and third times, which are referred to as VT-650-2,VTS-650-2, VT-650-3, VTS-650-3, VT-650-725, VTS-650-725, VT-650-725-2, and VTS-650-725-2, respectively, according to the upscanning temperatures and times. The detailed heat-treatment procedure is given in Table 1.

The crystal phases in VT and VTS after various heat treatment were identified on a PANalytical X-ray diffractometer with Cu Kα (λ = 1.5406 Å) radiation. NMR measurement for VT, VTS were performed on a Bruker Avance III HD 500 M spectrometer (11.7 T). We detected $^{51}V$ and $^{125}Te$ spectra for VT and VTS, and $^{29}Si$ spectra for VTS. The $^{29}Si$, $^{51}V$ and $^{125}Te$ NMR measurements were conducted at the resonance frequencies of 99.4, 131.7 and 159.1 MHz, respectively. $^{29}Si$ MAS NMR spectra were measured at a spinning rate of 6.0 kHz. Relaxation delays of 200 s were used, and chemical shift is referenced to Tetrakis (tetramethyl) silicate silane (= -9.7 ppm). $^{51}V$ Hahn echo NMR experiments were operated at a spinning rate of 0 kHz with the pulse length of 2.4 μs. $^{125}Te$ static wideband uniform-rate smooth truncation QCPMG (WURST-QCPMG) NMR spectra were obtained using the WURST-80 pulse sequence and an 8-step phase cycle, employing 50-μs excitation and refocusing pulses (liquid nutation frequency 8.1 kHz). FTIR spectra of Si and VTS were obtained by a Bruker Invenio S infrared spectrometer in the wavenumber range of 400 to 1400 $cm^{-1}$ at room temperature with a resolution of 4 $cm^{-1}$.

## 3. Results

To investigate how and at which temperature Si and VT glass were

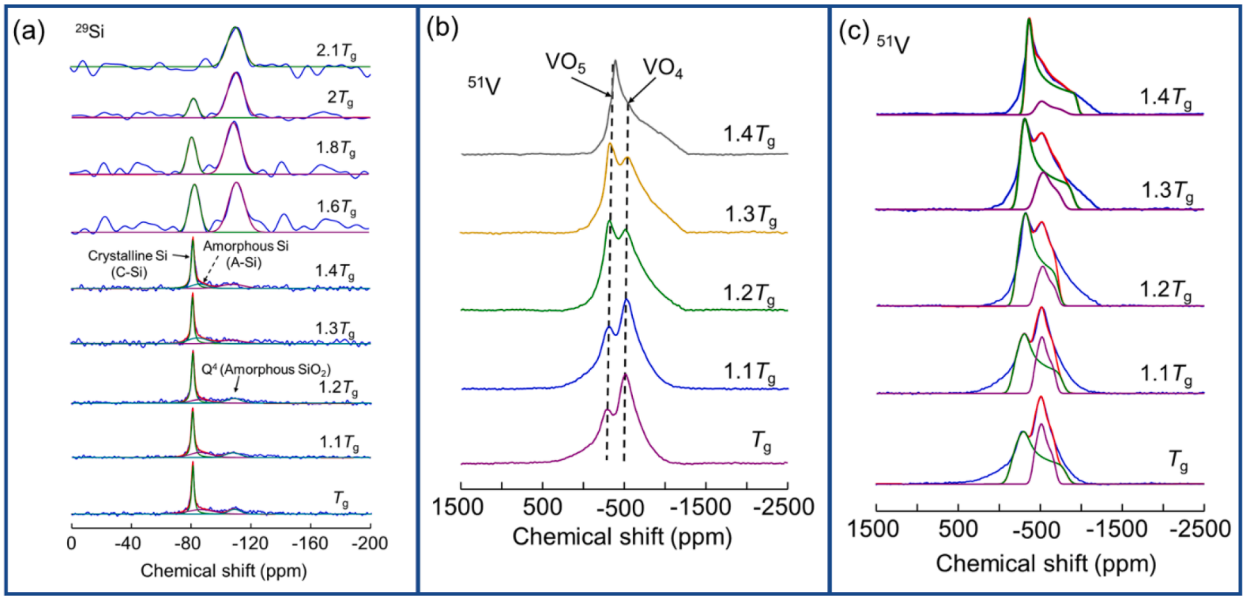


**Fig. 1.** $^{29}Si$ and $^{51}V$ NMR spectra of VTS upscanned in DSC to different temperatures at 10 K/min in argon. (a) $^{29}Si$ NMR spectra of VTS upscanned to $T_g \sim 2.1T_g$, (b) $^{51}V$ NMR spectra of VTS upscanned to $T_g \sim 1.4T_g$, (c) deconvolution of $^{51}V$ NMR spectra shown in (b). Purple and green curves represent the $VO_4$ and $VO_5$ contributions, respectively.

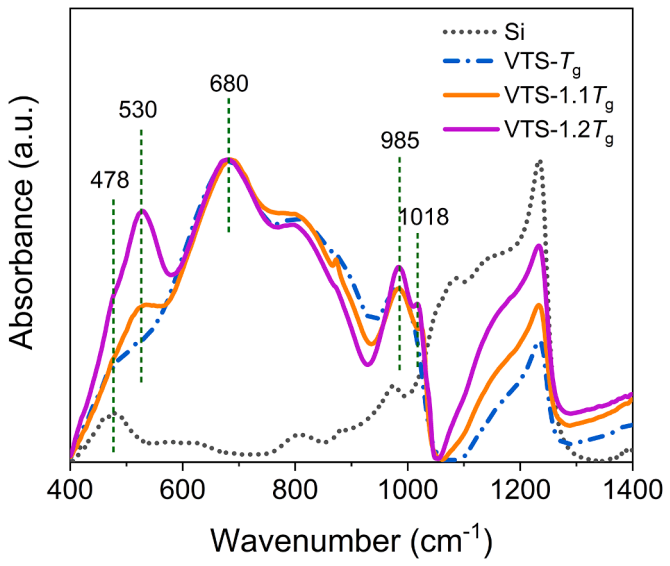


**Fig. 2.** FTIR spectra of Si and VTS after upscanning in DSC to $T_g$, 1.1$T_g$ and 1.2$T_g$ at 10 K/min in argon.

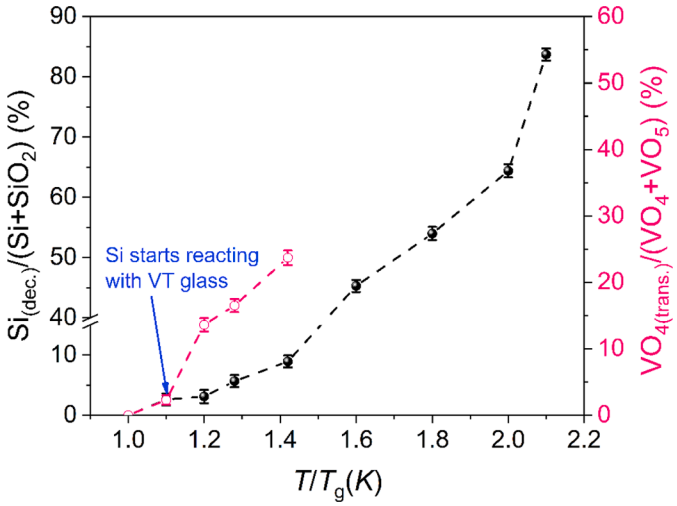


**Fig. 3.** The dependences of both $Si_{(dec.)}/(Si+SiO_2)$ and $VO_{4(trans.)}/((VO_4+VO_5)$ on the maximum DSC upscanning temperatures for VTS samples. The $T/T_g$ represents the ratio of the DSC upscanning temperature to the glass transition temperature of VTS.

bonded together during heating process, NMR analysis was performed on the VTS after upscanning to different temperatures in DSC to probe their local structural changes. Fig. 1a shows the $^{29}$Si spectra of VTS after upscanning to 1.1, 1.2, 1.3, 1.4, 1.6, 1.8, 2 and 2.1$T_g$, respectively, by DSC in argon. Each spectrum can be deconvoluted into three peaks, i.e., at ~ −80 ppm, −85 ppm, and −110 ppm. These three peaks are attributed to crystalline Si (C-Si), amorphous Si (A-Si), and $Q^4$ in amorphous $SiO_2$ [6], respectively, where Q represents tetrahedron, and 4 is the number of bridging oxygen [7]. It can be seen that the peak at ~ −80 ppm becomes broader and weaker with an increase of the maximum upscanning temperature ($T_{max}$). The peak at ~ −85 ppm decreases and disappears at 1.6$T_g$ while the peak at ~ −110 ppm increases gradually. This implies that the nano-Si (both C-Si and A-Si) transformed into amorphous $SiO_2$ during the heating process. Fig. 1b shows the $^{51}$V spectrum of VTS after scanning to different temperatures. The spectrum of each sample is deconvoluted into two components, i.e., purple and green curves, which are ascribed to $[VO_4]$ and $[VO_5]$, respectively, where 4 or 5 are the numbers of oxygen coordinated to each vanadium (in Fig. 1c). For VTS, as $T_{max}$ increases, the fraction of $[VO_5]$ increases, while that of $[VO_4]$ decreases.

To further explore the reaction between Si and VT glass, FTIR spectra for Si, VTS-$T_g$, 1.1$T_g$, 1.2$T_g$ were obtained and normalized by the strongest peak, as shown in Fig. 2. For the Si spectrum (black dash line), the peaks at 478cm$^{-1}$ and at around 1000~1250 cm$^{-1}$ correspond to Si−O vibrations [8,9]. For the spectra of VTS-$T_g$, -1.1$T_g$, and -1.2$T_g$ samples, peaks at 680 cm$^{-1}$ are assigned to O−Te−O or Te−O−Te vibrations [10]. The peaks at around 985cm$^{-1}$ are due to the vibrations of $[VO_5]$ while the peak at 1018 cm$^{-1}$ arises from V=O vibrations in $[VO_5]$ [10–14]. In addition, the broad peaks locating between 750 and 940 cm$^{-1}$ are mainly assigned to V−O−V, $[VO_4]$, and $[VO_5]$ vibrations and the peaks at around 1050~1250 cm$^{-1}$ arise from Si−O vibrations [9,10,12,15]. It should be noted that a new peak at 530 cm$^{-1}$ is associated with the V−O−V vibration in each spectrum of VTS-1.1$T_g$ and -1.2$T_g$ samples, respectively [16–19]. Obviously, the intensities of peaks at 530 cm$^{-1}$, 985 cm$^{-1}$, 1018 cm$^{-1}$, and 1050~1250 cm$^{-1}$ increase with increasing $T_{max}$, indicating an increase in the numbers of V−O−V bonds, $[VO_5]$ units and the Si−O bonds. This is consistent with the NMR results (Fig. 1).

Based on the NMR results in Fig. 1, the fractions of Si, $SiO_2$, $VO_4$, and $VO_5$ are determined by their respective deconvoluted peak areas obtained by integrating the signal intensity over the chemical shift. The fractions of both the decreased Si (i.e., $Si_{(dec.)}/(Si+SiO_2)$) and the $[VO_4]$ transformed into $[VO_5]$ (i.e., $VO_{4(trans.)}/(VO_4+VO_5)$), are used to assess the critical temperature, at which Si starts to react with VT glass. Specifically, $Si_{(dec.)}$ refers to the fraction of Si, which has been oxidized to $Si^{4+}$ during heating. It is obtained by subtracting the fraction of Si in VTS heated to a temperature above $T_g$ from that in VTS heated to $T_g$. $VO_{4(trans.)}$ refers to the fraction of $VO_4$ units that have been transformed into $VO_5$ during heating, which is determined by subtracting $VO_4$ fraction in VTS heated to a temperature above $T_g$ from that in VTS heated to $T_g$. The dependences of both $Si_{(dec.)}/(Si+SiO_2)$ and $VO_{4(trans.)}/((VO_4+VO_5)$ on the $T_{max}$s are shown in Fig. 3. Obviously, $Si_{(dec.)}$ rises with increasing the $T_{max}$, interestingly, it increases drastically when $T_{max}$ is higher than 1.4$T_g$, suggesting that a violent reaction occurs between Si and VT glass. In contrast, $VO_{4(trans.)}$ increases dramatically from 1.1$T_g$ to 1.4$T_g$. The changes in both $Si_{(dec.)}$ and $VO_{4(trans.)}$ imply that nano-Si starts to react with VT glass at 1.1$T_g$. This means that the nano Si-to-$SiO_2$ conversion in VT glass can be controlled by varying the heat-treatment temperature.

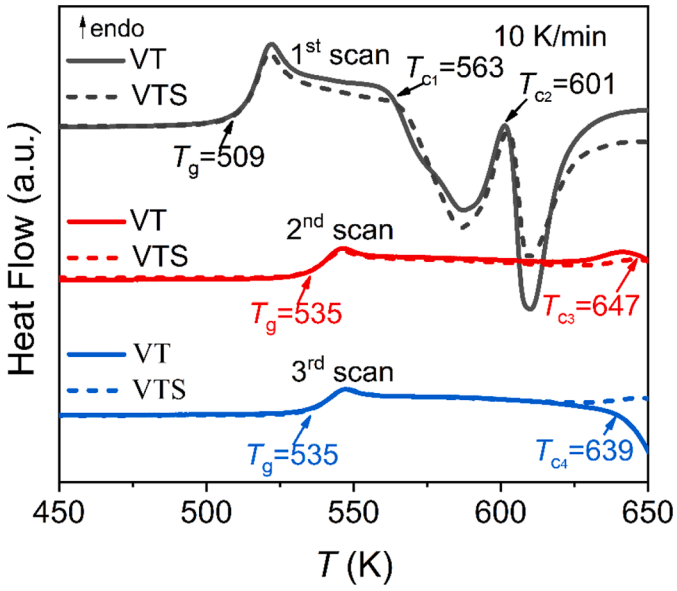


**Fig. 4.** DSC upscan curves of both VT (the solid line) and VTS (the dotted line), which are obtained at 10 K/min in argon. The characteristic temperatures such as $T_g$, $T_{c1}$, $T_{c2}$, $T_{c3}$, and $T_{c4}$for VT and VTS are denoted.

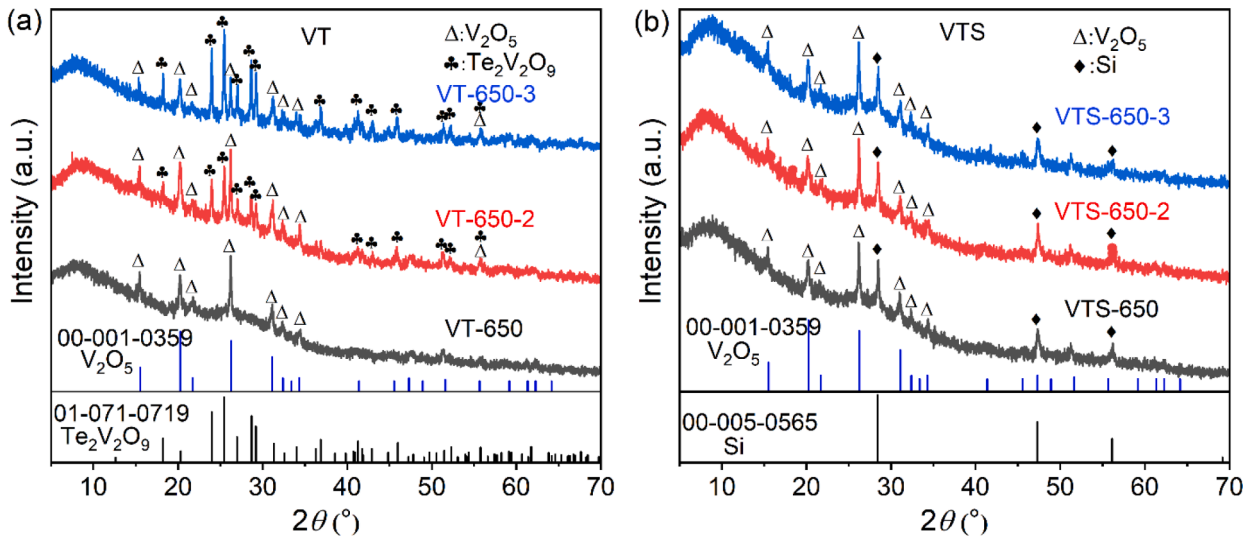


**Fig. 5.** XRD patterns of (a) VT and (b) VTS after the first, second and third DSC upscans to 650 K at 10 K/min in argon.

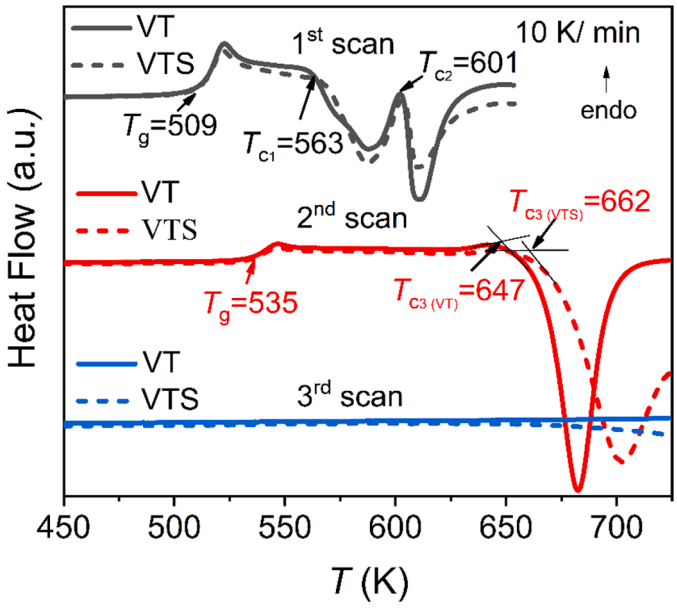


**Fig. 6.** DSC upscan curves of both VT (the solid line) and VTS (the dotted line), which are obtained at 10 K/min in argon. The 1st DSC upscan was performed to 650 K, and the 2nd and 3rd upscans were performed to 725 K. The characteristic temperatures such as $T_g$, $T_{c1}$, $T_{c2}$, and $T_{c3}$ for VT and VTS are denoted.

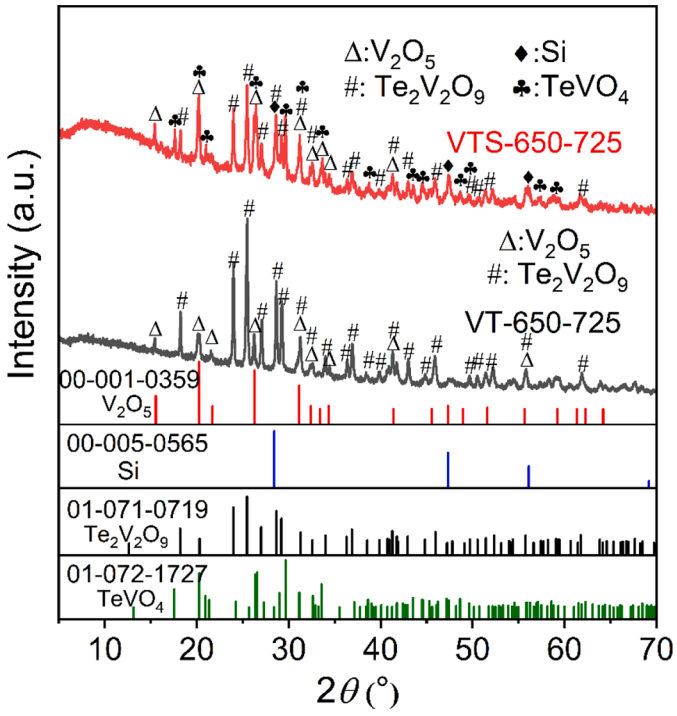


**Fig. 7.** XRD patterns of VT and VTS after two DSC upscans at 10 K/min in argon. The first upscan was performed to 650 K and then the second one was to 725 K, which are referred to as VT-650-725 and VTS-650-725, respectively.

Since Si can react with VT glass during the heating process, it is important to find out whether the Si-doping affects the crystallization behavior of VT glass. Fig. 4 shows the DSC upscan curves of the VT and the VTS to 650 K for three times at 10 K/min, and according to the number of the upscans, the samples are denominated as VT-650, VTS-650, VT-650-2, VTS-650-2, VT-650-3, and VTS-650-3, respectively. The $T_g$ of both VT and VTS shifts to a higher temperature from the first to the 2nd upscan due to the crystallization in the first upscan. Then $T_g$s remain constant in the subsequent upscans. In addition, the $T_g$ of VT is the same as that of VTS at each upscan, implying that the remaining glass phase in VT and VTS after crystallization might have the same composition. The two exothermic peaks with onset temperatures of $T_{c1}$ and $T_{c2}$ (see the first DSC upscans), respectively, do not appear in the 2nd and 3rd DSC upscan curves. However, new crystallization peaks with onset temperatures of $T_{c3}$ and $T_{c4}$ occur for VT but not for VTS, suggesting that the crystallization in VT glass was suppressed by introducing nano-Si.

Fig. 5 shows the XRD patterns of VT and VTS after the first, second and third DSC upscans to 650 K. The VT-650 sample shares the same XRD pattern as that of VTS-650, from which the $V_2O_5$ crystals can be identified. The precipitation of $V_2O_5$ increases the connectivity of the structural network according to a previous study [20], and thereby increasing $T_g$. However, $Te_2V_2O_9$ crystals are found in VT-650-2 and VT-650-3, but not in the corresponding VTS samples. This implies that the crystallization of $Te_2V_2O_9$ has been suppressed by introducing nano-Si into VT glass. In addition, this finding suggests that although the VT and VTS samples have the same $T_g$ for both the 2nd and 3rd upscan curves, the compositions of the remaining glass matrices are different between the two samples.

To further explore the effect of nano-Si on the crystallization of VT

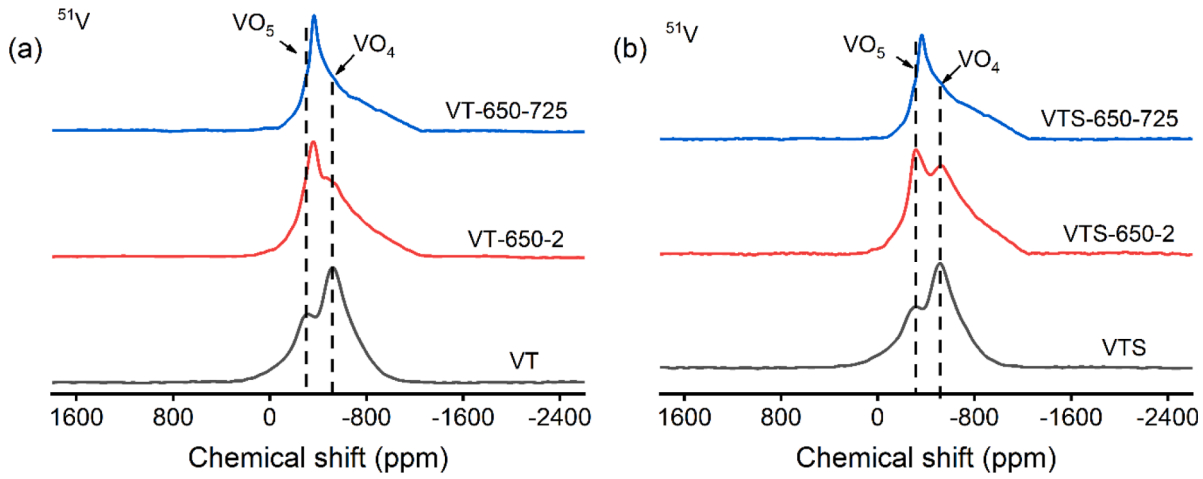


**Fig. 8.** $^{51}$V NMR spectra of (a) VT and (b) VTS samples before and after two different DSC upscan protocols at 10 K/min in argon. One is to upscan VT and VTS to 650 K twice (VT-650-2, VTS-650-2), the other is to upscan VT and VTS to 650 K first and then to 725 K (VT-650-725, VTS-650-725).

**Table 2**
The fraction of $VO_5$ and $VO_4$, which were obtained from the deconvoluted $^{51}$V NMR spectra shown in Fig. S2.

| Sample Name | $VO_5$ (%) | $VO_4$ (%) | $VO_5$/ $VO_4$ | Sample Name | $VO_5$ (%) | $VO_4$ (%) | $VO_5$/ $VO_4$ |
|---|---|---|---|---|---|---|---|
| VT | 62.2 | 37.8 | 1.65 | VTS | 62.3 | 37.7 | 1.65 |
| VT-650-2 | 80.9 | 19.1 | 4.24 | VTS-650-2 | 75.8 | 24.2 | 3.13 |
| VT-650-725 | 88.1 | 11.9 | 7.40 | VTS-650-725 | 88.2 | 11.8 | 7.47 |

glass, VT and VTS were upscanned to 650 K firstly and then to 725 K for the 2$^{nd}$ and 3$^{rd}$ times as shown in Fig. 6. Like the results in Fig. 4, the $T_g$s of both VT and VTS increase from the first to the second DSC upscan. However, the $T_{c3}$ (662 K) of VTS-650-725 sample is higher than that (647 K) of VT-650-725, further confirming that the crystallization corresponding to $T_{c3}$ is suppressed by introducing nano-Si into VT glass. In addition, the glass transitions do not occur in both VT-650-725-2 and VTS-650-725-2, implying that the glasses are fully transformed into crystal phase during the second DSC upscan.

Fig. 7 shows the XRD patterns of VT-650-725 and VTS-650-725, respectively. The Bragg peaks in the XRD pattern of VT-650-725 are attributed to $V_2O_5$ and $Te_2V_2O_9$. Besides these two crystalline phases, another crystalline phase, i.e., $TeVO_4$ is identified in the VTS-650-725. In other words, although the crystallization of $Te_2V_2O_9$ in VT glass is suppressed to some extent by introducing nano-Si, a new crystalline phase ($TeVO_4$) is precipitated during this process. The formation of $TeVO_4$ could be caused by the reaction of VT glass and nano-Si.

To probe the microstructural evolution in VT and VTS samples after different DSC scans, $^{51}$V and $^{125}$Te NMR measurements were performed. The deconvolutions of $^{51}$V and $^{125}$Te spectra were conducted based on chemical shift anisotropy (CSA) model [21]. Fig. 8 shows the $^{51}$V NMR spectra of VT, VTS, VT-650-2, VTS-650-2, VT-650-725, and VTS-650-725, respectively. The spectrum of each sample is deconvoluted into two components (purple and green curves), which are ascribed to $VO_4$ and $VO_5$, respectively (Fig. S2). The fractions of $VO_4$ and $VO_5$ in each sample are shown in Table 2. As $T_{max}$ increases, the $VO_5/VO_4$ ratio increases for both VT and VTS. Moreover, the $VO_5/VO_4$ ratio is higher in VT-650-2 than that in VTS-650-2. This is due to the fact that both $Te_2V_2O_9$ and $V_2O_5$ crystals, in which the majority of vanadium exist in $VO_5$ [22–28], are precipitated in VT-650-2, while only $V_2O_5$ forms in VTS-650-2. The lower $VO_5/VO_4$ ratio in VTS-650-2 further confirms the inhibiting effects of Si on the crystallization of VT glass when the sample was heat-treated to 650 K ($\approx 1.3T_g$). When $T_{max}$ reaches 725 K ($\approx 1.4T_g$), the $VO_5/VO_4$ ratio in VTS-650-725 is almost the same as that in VT-650-725. This is because the two glass samples are fully transformed into crystalline phase, as verified in Fig. 6. Although a new $TeVO_4$ phase is precipitated in VTS-650-725 besides $V_2O_5$ and $Te_2V_2O_9$, the majority of vanadium in $TeVO_4$ exists in $VO_5$ [24–27].

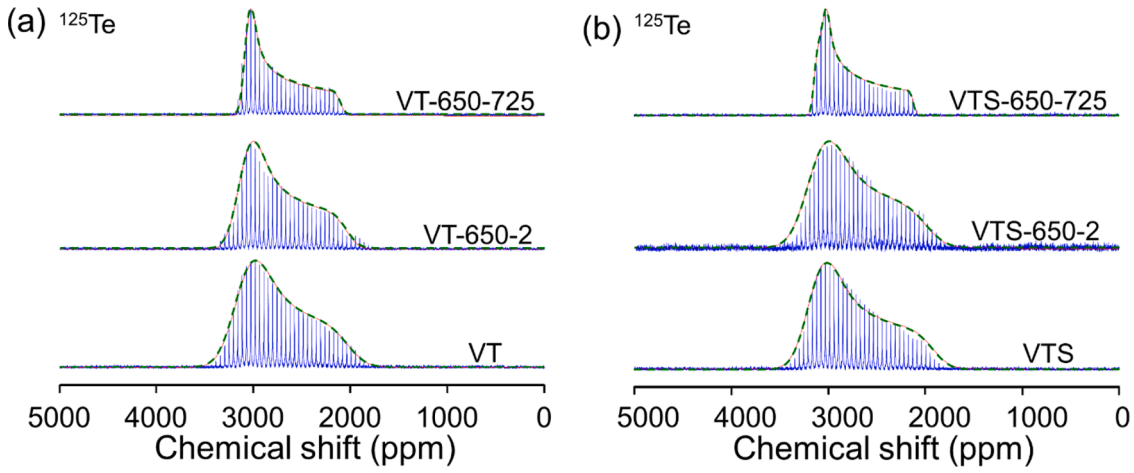


**Fig. 9.** $^{125}$Te NMR spectra of (a) VT and (b) VTS samples before and after two different DSC upscan protocols at 10 K/min in argon. One is to upscan VT and VTS to 650 K twice (VT-650-2, VTS-650-2), the other is to upscan VT and VTS to 650 K first and then to 725 K (VT-650-725, VTS-650-725). Dashed lines: the fitting curves.

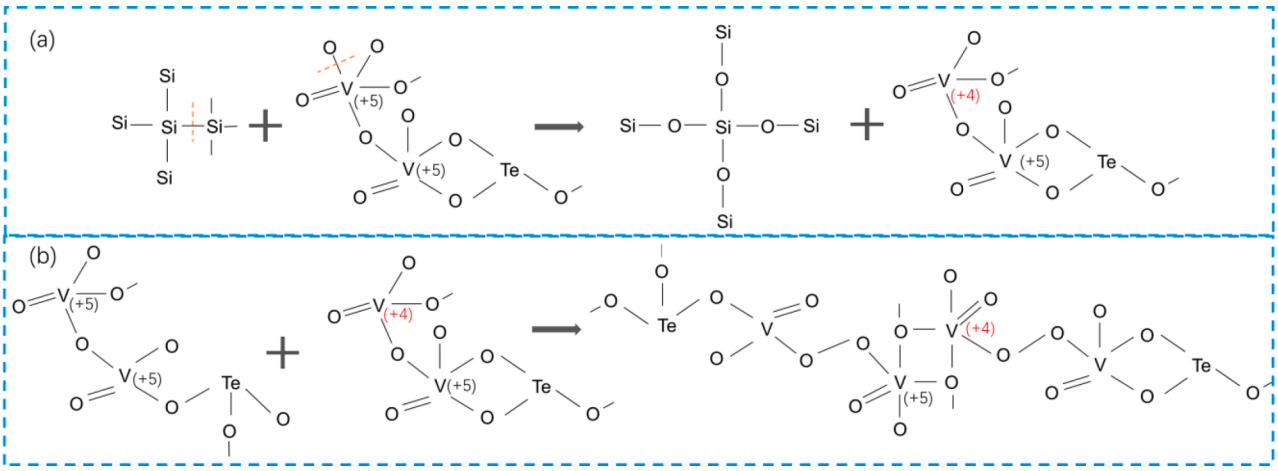


**Fig. 10.** Schematic diagram of the reaction between Si and VT glass (a), and the evolution of [$VO_4$] to [$VO_5$] (b) when VTS was upscanned by DSC above its $T_g$ at 10 K/min in argon.

Fig. 9 shows the $^{125}$Te NMR spectra of VT, VTS, VT-650-2, VTS-650-2, VT-650-725, and VTS-650-725. Each $^{125}$Te spectrum can be represented by one unsymmetric peak, which should be ascribed to 3-coordinated Te, considering the chemical shift anisotropy (CSA) values (approximately 640-820) and the asymmetry parameters ($\eta_{CS}$) (0.1-0.2) (see Table S1) [29,30]. The peak shape of $^{125}$Te spectrum becomes sharper as $T_{max}$ rises, suggesting the transformation of glass into Te-containing crystals [23]. The sharper peak in VT-650-2 compared to that in VTS-650-2 also indicates that crystallization of $Te_2V_2O_9$ has been suppressed in VTS.

## 4. Discussion

As shown above, an increase of $T_{max}$ leads to a pronounced increase both in the $Si_{(dec.)}/(Si+SiO_2)$, $VO_{4(trans)}/(VO_4+VO_5)$ ratios and in the number of V−O−V bonds and this indicates that the doped Si does react with VT glass. It should be mentioned that two exothermic peaks (with onset temperatures, $T_{c1}$ and $T_{c2}$, respectively) consecutively occur in the 1$^{st}$ DSC upscan curve of VTS when heating to 650 K (Fig. 4), but only one crystalline phase ($V_2O_5$) is identified from the XRD pattern (Fig. 5). This could be explained by the possible scenario where the first and the second peak could be caused by the surface crystallization and the bulk crystallization (i.e., $V_2O_5$ formation), respectively. In addition, as shown in Fig. 6, a new crystallization peak with the onset temperature ($T_{c3}$) of 662 K for VTS appears, which is much larger than that for VT. This can be ascribed to the precipitation of two crystal phases $Te_2V_2O_9$ and $TeVO_4$, while only $Te_2V_2O_9$ precipitated in VT sample, as evidenced by the XRD patterns in Fig. 7. This means that two phases ($V_2O_5$ and $Te_2V_2O_9$) exist in VT-650-725, whereas, besides Si, three phases ($V_2O_5$, $Te_2V_2O_9$, and $TeVO_4$) occur in VTS-650-725 (Fig. 7).

Based on the NMR results in Fig. 1, the reaction of Si with oxygen leads to formation of amorphous $SiO_2$, where Si is tetrahedrally bonded to 4 bridging oxygen, during heating the VTS sample. One possible reaction mechanism is that Si bonds to 4 oxygens and each oxygen is provided by one [$VO_5$] unit in VT glass, consequently, the tetrahedral [$SiO_4$] network locally forms and [$VO_4$] units appear. Meanwhile, Si reduces $V^{5+}$ to $V^{4+}$. Then, the remaining [$VO_x$] units rearrange themselves to the ordered structure, i.e., crystals form during the heating process to a temperature of 662 K, and simultaneously part of [$VO_4$] units are transformed into [$VO_5$] units by sharing oxygen with other [$VO_4$] units. Thus. the chain-like [$VO_4$] structure are converted into zigzag [$VO_5$] structure (Fig. 10) [23], generating new V−O−V bonds as verified by NMR and FTIR results shown in Fig. 2.

In addition, introducing nano-Si into VT glass has only a minor effect on formation of $V_2O_5$, but can suppress the crystallization of $Te_2V_2O_9$ during the first and second DSC upscans to 650 K. When the $T_{max}$ is increased to 725 K, both $Te_2V_2O_9$ and $TeVO_4$ crystals formed for VTS (Fig. 7). However, the onset temperature ($T_{c3}$) of the crystallization peak for VTS glass is higher than that of VT glass (see Fig. 6). This means that the nano-Si has the suppressing effect on crystallization of VT glass. To uncover the crystallization-suppressing mechanism of Si on VT glass, it is important to clarify the redox reaction between Si and VT glass. In this regard, we need to derive the redox reaction equation for $n$ moles of VT glass. During the first upscan to 650 K, since only a small amount of Si particles has reacted with VT glass, the moles of the original glass can be approximately considered to be $n$ moles. After the first upscan to 650 K, $k$ moles $V_2O_5$ crystals are assumed to precipitate from the glass matrix. Thus, the chemical formula of the remaining glass (R-glass) is expressed as $Te_nV_{2(n-k)}O_{7n-5k}$ (n>$k$, $n$>0, $k$>0). Assuming that the molar amounts of the reacted Si and R-glass are $x$ and $y$, respectively, during the second DSC scan, then the reaction can be written as:

$$xSi + yTe_nV_{2(n-k)}O_{7n-5k} \rightarrow yTe_nV_{2(n-k)}O_{7n-5k-2x} + xSiO_2(amorphous) \quad (1)$$

Among the four types of elements in the VTS sample, only vanadium is polyvalent, since it can exist as $V^{5+}$ and $V^{4+}$. Therefore, considering the charge balance of the reaction, Si reduces $V^{5+}$ to $V^{4+}$. Thus, we get the equations:$4x = 2y(n-k)$, then $x = \frac{y(n-k)}{2}$. In addition, owing to the conservation of oxygen ions, the relation $y(7n-5k) = y(7n-5k-2x) + 2x$ should be valid, from which y is found to be 1. Since the new crystal ($TeVO_4$) is precipitated from VTS-650-725, the values of $n$ and $k$ can be 2 and 1, respectively. Hence, reaction (1) can be rewritten as:

$$\frac{1}{2}Si + Te_2V_2O_9(glass) \rightarrow Te_2V_2O_8(2TeVO_4)(glass) + \frac{1}{2}SiO_2(amorphous) \quad (2)$$

During the first and second DSC upscan to 650 K, in addition to the energy used to overcome the energy barrier for $V_2O_5$ formation, the remaining energy is preferentially consumed for the reaction (2). However, when increasing $T_{max}$ of the second upscan to 725 K, the thermal energy is sufficient for overcoming the energy barrier for both the precipitation of $Te_2V_2O_9$ and $TeVO_4$ crystals and that for reaction (2).

## 5. Conclusions

We prepared a composite material that is composed of nano-Si and $V_2O_5$-$TeO_2$ glass (VT) to be potentially applied as the anode material for advanced LIBs. The nano-Si is physically mixed with the VT glass, and then the mixture was subjected to different dynamic heat-treatment in argon. By using both solid-state NMR and FTIR techniques, we clarified

both the reaction mechanism of nano-Si with VT glass and their crystallization behavior. The nano-Si reacted with VT glass at $\geq 1.1T_g$ (560 K), leading to formation of amorphous $SiO_2$. The nano Si-to-$SiO_2$ conversion in VTS glass can be controlled by designing the heating protocol.

Moreover, it was found that introducing nano Si into VT glass could suppress the formation of $Te_2V_2O_9$ crystals during heating to 650 K ($1.3T_g$) but induce the formation of $TeVO_4$ during heating to a higher temperature 725 K ($1.4T_g$). This was explained by the redox reaction between nano-Si and the remaining glass after $V_2O_5$ precipitation. That is, during the heating of VTS sample, $V_2O_5$ was precipitated. After that, nano-Si reacted with $Te_2V_2O_9$ glass phase, leading to formation of amorphous $SiO_2$ and $TeVO_4$ glass phase. Differing from the crystallization in VT glass under the same heating condition, the crystallization in VTS glass requires more thermal energy to overcome the energy barrier for redox reaction (2), thereby making the formation of $Te_2V_2O_9$ crystals more difficult. When VTS was heated to a higher temperature 725 K ($1.4T_g$), the energy is sufficient for formation of both $TeVO_4$ and $Te_2V_2O_9$ phases. This work helps design Si-oxide glass composites for a specific application, e.g., in high performance LIBs.

## CRediT authorship contribution statement

**Jiajia Yan:** Investigation, Methodology, Data curation, Writing – original draft. **Tongyao Zhao:** Investigation, Data curation. **Nian Shi:** Investigation, Data curation. **Hongbing Zhan:** Writing – review & editing. **Jinjun Ren:** Methodology, Data curation, Writing – review & editing. **Yanfei Zhang:** Conceptualization, Methodology, Writing – review & editing. **Yuanzheng Yue:** Supervision, Methodology, Conceptualization, Writing – review & editing.

## Declaration of Competing Interest

The authors declare that they have no known competing financial interests or personal relationships that could have appeared to influence the work reported in this paper.

## Acknowledgments

Authors would like to acknowledge support by National Natural Science Foundation of China (Nos. U1732155, 51672045, 51772223), China Scholarship Council (201906650022), Taishan Youth Scholar Project of Shandong Province (tsqn202103098), and Shandong Provincial Natural Science Foundation (ZR2020ME025).

## Supplementary materials

Supplementary material associated with this article can be found, in the online version, at doi:10.1016/j.jnoncrysol.2022.121651.

## References

[1] D.H. Tan, Y.T. Chen, H. Yang, W. Bao, B. Sreenarayanan, J.M. Doux, W. Li, B. Lu, S. Y. Ham, B. Sayahpour, Carbon-free high-loading silicon anodes enabled by sulfide solid electrolytes, Science 373 (2021) 1494–1499.
[2] Y.F. Zhang, P. Wang, T. Zheng, D. Li, G. Li, Y. Yue, Enhancing Li-ion battery anode performances via disorder/order engineering, Nano Energy 49 (2018) 596–602.
[3] Y.F. Zhang, P.X. Wang, G.D. Li, J.H. Fan, C.W. Gao, Z.Y. Wang, Y.Z. Yue, Clarifying the charging induced nucleation in glass anode of Li-ion batteries and its enhanced performances, Nano Energy 57 (2019) 592–599.
[4] J. Kjeldsen, Y. Yue, C.B. Bragatto, A.C. Rodrigues, Electronic conductivity of vanadium-tellurite glass-ceramics, J. Non Cryst. Solids 378 (2013) 196–200.
[5] X. Liu, Heterogeneous nucleation or homogeneous nucleation? J. Chem. Phys. 112 (2000) 9949–9955.
[6] P. Pena, J.R. Mercury, A. De Aza, X. Turrillas, I. Sobrados, J. Sanz, Solid-state $^{27}Al$ and $^{29}Si$ NMR characterization of hydrates formed in calcium aluminate–silica fume mixtures, J. Solid State Chem. 181 (2008) 1744–1752.
[7] J. Xu, X. Wang, H. Fu, C.M. Brown, X. Jing, F. Liao, F. Lu, X. Li, X. Kuang, M. Wu, Solid-state $^{29}Si$ NMR and Neutron-diffraction studies of $Sr_{0.7}K_{0.3}SiO_{2.85}$ oxide ion conductors, Inorg. Chem. 53 (2014) 6962–6968.
[8] I. Joni, L. Nulhakim, M. Vanitha, C. Panatarani, Characteristics of crystalline silica ($SiO_2$) particles prepared by simple solution method using sodium silicate ($Na_2SiO_3$) precursor, J. Phys. Conf. Ser. 1080 (2018), 012006.
[9] W. Yang, W. Huang, Q. Zheng, W. Huang, Z. Chen, High efficiency preparation, structure and properties of silicon nano-crystals by induction plasma method, NanoWorld J. 2 (2016) 63–68.
[10] S. Rada, E. Culea, V. Rus, M. Pica, M. Culea, The local structure of gadolinium vanado-tellurite glasses, J. Mater. Sci. 43 (2008) 3713–3716.
[11] A. Rahim, A. Arof, Spectroscopic studies of $V_2O_5$–$Bi_2O_3$–$TeO_2$ glasses, Opt. Quantum Electron. 48 (2016) 238.
[12] Y. Saddeek, I. Yahia, W. Dobrowolski, L. Kilanski, N. Romcevic, M. Arciszewska, Infrared, Raman spectroscopy and ac magnetic susceptibility of $Gd_2O_3$-$TeO_2$-$V_2O_5$ glasses, Optoelectron. Adv. Mater. Rapid Commun. 3 (2009) 559–564.
[13] V. Murgia, E.M.F. Torres, J.C. Gottifredi, E.L. Sham, Sol gel synthesis of $V_2O_5$–$SiO_2$ catalyst in the oxidative dehydrogenation of n-butane, Appl. Catal. A Gen. 312 (2006) 134–143.
[14] T. Srikumar, C.S. Rao, Y. Gandhi, N. Venkatramaiah, V. Ravikumar, N. Veeraiah, Microstructural, dielectric and spectroscopic properties of $Li_2O$–$Nb_2O_5$–$ZrO_2$–$SiO_2$ glass system crystallized with $V_2O_5$, J. Phys. Chem. Solids 72 (2011) 190–200.
[15] K. Shafeeq, V. Athira, C.R. Kishor, P. Aneesh, Structural and optical properties of $V_2O_5$ nanostructures grown by thermal decomposition technique, Appl. Phys. A 126 (2020) 1–6.
[16] W. Chen, J. Peng, L. Mai, H. Yu, Y. Qi, Synthesis and characterization of novel vanadium dioxide nanorods, Solid State Commun. 132 (2004) 513–516.
[17] M.M. Islam, M.A. Rashid, M.P. Ahamed, M.E. Hossain, M.R. Ahsan, M.G. Mortuza, M.H.K. Rubel, Morphogenesis of silicovanadate glasses: investigation of physical properties, J. Eng. Adv. (2021) 78–86.
[18] H. Ji, D. Liu, H. Cheng, C. Zhang, L. Yang, D. Ren, Infrared thermochromic properties of monoclinic $VO_2$ nanopowders using a malic acid-assisted hydrothermal method for adaptive camouflage, RSC Adv. 7 (2017) 5189–5194.
[19] X. Wu, Z. Wu, C. Ji, H. Feng, X. Ma, Y. Su, Y. Zhou, J. Wang, Y. Jiang, Influence of infrared optical properties by transformation of the crystal structure in Al-doped vanadium dioxide films, Opt. Mater. Express 6 (2016) 3500–3506.
[20] S. Chakraborty, P. Boolchand, M. Malki, M. Micoulaut, Designing heavy metal oxide glasses with threshold properties from network rigidity, J. Chem. Phys. 140 (2014), 014503.
[21] M. Bak, J.T. Rasmussen, N.C. Nielsen, SIMPSON: a general simulation program for solid-state NMR spectroscopy, J. Magn. Reson. 213 (2011) 366–400.
[22] C.J. Fontenot, J.W. Wiench, G.L. Schrader, M. Pruski, $^{17}O$ MAS and 3QMAS NMR investigation of crystalline $V_2O_5$ and layered $V_2O_5{\cdot}nH_2O$ Gels, J. Am. Chem. Soc. 124 (2002) 8435–8444.
[23] S. Sakida, S. Hayakawa, T. Yoko, $^{125}Te$ and $^{51}V$ static NMR study of $V_2O_5$-$TeO_2$ glasses, J. Phys. Condens. Matter. 12 (2000) 2579.
[24] M.I. Aroyo, A. Kirov, C. Capillas, J. Perez-Mato, H. Wondratschek, Bilbao Crystallographic Server. II. Representations of crystallographic point groups and space groups, Acta Crystallogr. Sect. A Found. Crystallogr. 62 (2006) 115–128.
[25] M.I. Aroyo, J.M. Perez-Mato, C. Capillas, E. Kroumova, S. Ivantchev, G. Madariaga, A. Kirov, H. Wondratschek, Bilbao crystallographic server: I. Databases and crystallographic computing programs, Z. Kristallogr. 221 (2006) 15–27.
[26] M. Vergniory, L. Elcoro, C. Felser, N. Regnault, B.A. Bernevig, Z. Wang, A complete catalogue of high-quality topological materials, Nature 566 (2019) 480–485.
[27] M.I. Aroyo, J. Perez-Mato, D. Orobengoa, E. Tasci, G. de la Flor, A. Kirov, Crystallography online: bilbao crystallographic server, Bulg. Chem. Commun. 43 (2011) 183–197.
[28] B. Bradlyn, L. Elcoro, J. Cano, M. Vergniory, Z. Wang, C. Felser, M. Aroyo, B. A. Bernevig, Topological quantum chemistry, Nature 547 (2017) 298–305.
[29] S. Sakida, S. Hayakawa, T. Yoko, Part 2 $^{125}Te$ NMR study of $M_2O$–$TeO_2$ (M= Li, Na, K, Rb and Cs) glasses, J. Non Cryst. Solids 243 (1999) 13–25.
[30] Z. Jiang, T. Zhao, J. Ren, Y. Zhang, Y. Yue, NMR evidence for the charge-discharge induced structural evolution in a Li-ion battery glass anode and its impact on the electrochemical performances, Nano Energy 80 (2021), 105589.

# Supplementary Materials for

# Impact of silicon doping on the structure and crystallization of a vanadium-tellurite glass

Jiajia Yan[a], Tongyao Zhao[b], Nian Shi[b], Jinjun Ren[b], Hongbing Zhan[c], Yanfei Zhang[d]*, Yuanzheng Yue[a]*

**This file includes:**

Figs. S1, S2

Table S1

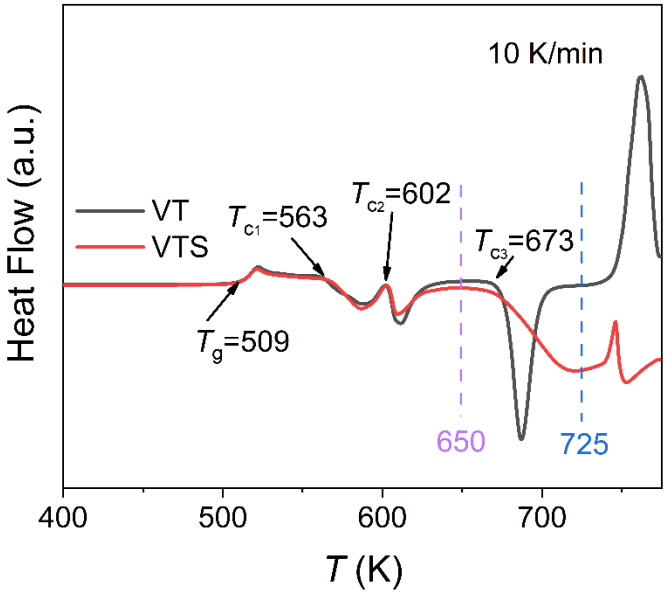


**Fig. S1.** DSC upscan curves of both VT (the dark line) and VTS (the red line), which are obtained at the rate of 10 K/min in argon. The characteristic temperatures such as glass transition ($T_g$) and crystallization onset temperatures ($T_{c1}$, $T_{c2}$, and $T_{c3}$) are denoted in the curves.

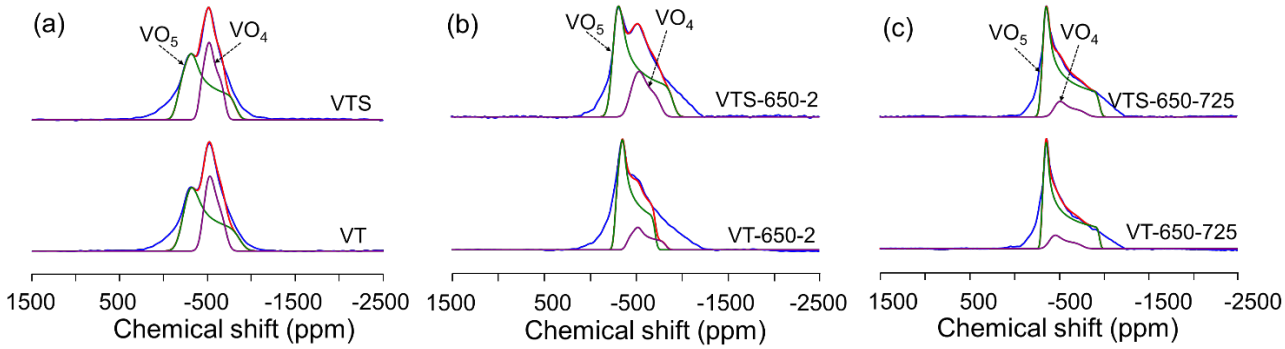


**Fig. S2** $^{51}$V NMR spectra of VT and VTS before and after DSC upscans to different temperatures at the rate of 10 K/min in argon. (a) $^{51}$V NMR spectra of VT and VTS without DSC scans. (b) $^{51}$V NMR spectra of VT and VTS after DSC upscans to 650 K twice. (c) $^{51}$V NMR spectra of VT and VTS after the first DSC upscans to 650 K and the second upscans to 725 K. Purple and green curves represent the $VO_4$ and $VO_5$ contributions, respectively.

**Table S1** Position, chemical shift anisotropy (CSA) and asymmetry parameter ($\eta_{CS}$) of $^{125}$Te NMR spectra of VT and VTS before and after two different DSC upscan protocols at the rate of 10 K/min in argon. One is to upscan VT/VTS to 650 K twice (VT/VTS-650-2), the other is to upscan VT/VTS to 650 K first and then to 725 K (VT/VTS-650-725).

| Sample Name | Position (ppm) | CSA | $\eta_{CS}$ |
|---|---|---|---|
| VT | 2739.3 | –720.9 | 0.20 |
| VT-650-2 | 2739.3 | –700.9 | 0.20 |
| VT-650-725 | 2739.3 | –640.8 | 0.10 |
| VTS | 2721.0 | –820.7 | 0.20 |
| VTS-650-2 | 2739.9 | –757.6 | 0.20 |
| VTS-650-725 | 2759.3 | –640.8 | 0.20 |

# Paper II

Nano Energy 103 (2022) 107779

Contents lists available at ScienceDirect

Nano Energy

journal homepage: www.elsevier.com/locate/nanoen

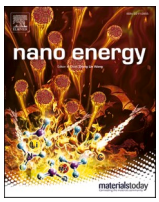

# Encapsulation of nano-Si into MOF glass to enhance lithium-ion battery anode performances

Jiajia Yan [a,1], Chengwei Gao [b,1], Shibin Qi [c], Zhenjing Jiang [c,d], Lars Rosgaard Jensen [e], Hongbing Zhan [f], Yanfei Zhang [c,*], Yuanzheng Yue [a,*]

[a] Department of Chemistry and Bioscience, Aalborg University, DK-9220 Aalborg, Denmark
[b] Laboratory of Infrared Material and Devices, Advanced Technology Research Institute, Ningbo University, Ningbo 315211, China
[c] School of Materials Science and Engineering, Qilu University of Technology (Shandong Academy of Sciences), Jinan 250353, China
[d] SEU-FEI Nano-Pico Center, Key Laboratory of MEMS of Ministry of Education, Southeast University, Nanjing 210096, China
[e] Department of Materials and Production, Aalborg University, 9220 Aalborg, Denmark
[f] College of Materials Science and Engineering, Fuzhou University, Fuzhou 350108, China

ARTICLE INFO

*Keywords:*
Metal-organic framework glass
Silicon
Anode
Lithium-ion batteries

ABSTRACT

Although metal-organic framework (MOF) glasses have exhibited high potential to be applied as anode materials for lithium-ion batteries (LIBs), their electrochemical performances still need to be greatly improved to match the rapid development of green energy technologies. Silicon is a promising candidate for the next generation of LIB anode but suffers from vast volume fluctuations upon lithiation/delithiation. Here, we present a strategy to in situ grow a kind of MOF, namely, cobalt-ZIF-62 ($Co(imidazole)_{1.75}(benzimidazole)_{0.25}$) on the surface of Si nano particles, and then to transform the thus-derived material into Si@ZIF-glass composite (SiZGC) through melt-quenching. The robust hierarchical structure of the SiZGC based anode exhibits the specific capacity of ~650 mA h $g^{-1}$, which is about three times that of pure ZIF glass and about six times that of pristine ZIF crystal at 1 A $g^{-1}$ after 500 cycles. The origin of this huge enhancement is revealed by performing structural analyses. The ZIF glass phase can not only contribute to lithium storage, but also buffer the volume changes and prevent the aggregation of Si nano particles during lithiation/delithiation processes.

## 1. Introduction

Lithium-ion batteries (LIBs) are still the main energy storage devices to meet the demand for clean and sustainable energy. The anode material in commercial LIBs is primarily graphite, which can accommodate lithium ions and exhibit a theoretical gravimetric capacity of 372 mA h $g^{-1}$ [1]. However, the capacity of graphite cannot meet the market demand for large-scale applications with high energy/power density and operation reliability. Therefore, it is vital to develop new anode materials with high capacity, low charging/discharging potential, and low production cost.

Concerning the specific capacity, silicon (Si) is potentially the best alternative anode material for LIBs, as it has a theoretical specific capacity of > 4000 mA h $g^{-1}$. In addition, Si is non-toxic and is the second most abundant element in earth crust, exhibiting low average discharge potential vs. $Li^+$/Li. However, pure Si anode exhibits very poor cycling stability, i.e., capacity retention is only about 50 mA h $g^{-1}$ within 100 cycles [2,3] due to the enormous volumetric expansion (> 300%) upon lithiation [4]. Furthermore, the low intrinsic electronic conductivity of Si leads to the sluggish electrochemical kinetics and causes severe polarization, limiting the utilization of Si anodes. To solve the aforementioned critical problems, significant efforts have been devoted to modifying Si morphology in nanoscale [5] and compositing Si with conducting and/or stress-relief buffer matrix to accommodate volume expansion [5–7]. For example, Cui et al. reported a silicon-nanolayer-embedded graphite anode for LIBs [8]. Thus, a delicate structure design based on Si for anode material is necessary to achieve outstanding battery performances.

Metal-organic frameworks (MOFs), which are three-dimensional networks constructed by metal nodes and organic ligands, have been receiving much attention owing to their promising applications, e.g., in catalyst, drug delivery, energy harvest, conversion and storage.

* Corresponding authors.
*E-mail addresses:* zhang-yanfei@hotmail.com (Y. Zhang), yy@bio.aau.dk (Y. Yue).
[1] These authors contributed equally to this work

https://doi.org/10.1016/j.nanoen.2022.107779
Received 11 August 2022; Received in revised form 5 September 2022; Accepted 6 September 2022
Available online 8 September 2022

Considering the ultrahigh specific surface area for contacting with collector, abundant active sites for $Li^+$ ions storage, as well as the tunable pores for migration of the $Li^+$ ions, MOFs are regarded as one of the most potential candidates to replace current graphite anode for LIBs [9,10]. Crystalline MOF-177, first used as anode materials by Chen et al. shows a high irreversible initial capacity of 400 mA h $g^{-1}$ but low capacity of 100 mA h $g^{-1}$ after 2 discharging/charging cycles [10]. To tackle the problem of poor electronic conductivity of MOF anodes, MOFs are coated with graphene to obtain the MOF/graphene composite anode, and thereby deliver a reversible capacity up to ~1075 mA h $g^{-1}$ at a current density of 50 mA $g^{-1}$ [11] and 400 mA h $g^{-1}$ at the current density of 100 mA $g^{-1}$ [9]. However, their reversible capacities at higher current densities still need further improvement to meet the soaring demands from modern electronic devices and electric vehicles.

As a promising method for improving the performances of anodes, vitrification of MOFs provides additional channels for $Li^+$ ion diffusion and storage due to the increased distortion and local breakage of the Co-N coordination bonds. Note that zeolitic imidazolate frameworks (ZIFs) are a subset of MOFs. It was recently reported that the anode based on cobalt-ZIF-62 glass exhibits high lithium storage capacity, i.e., 306 mA h $g^{-1}$ after 1000 cycles at 2 A $g^{-1}$, high cycling stability, and superior rate performance compared with both crystalline and amorphous ones (prepared by high-energy ball-milling) [12]. It should be mentioned that cobalt-ZIF-62 is a type of ZIF with the composition of Co(imidazole)$_{1.75}$(benzimidazole)$_{0.25}$. However, the ZIF glass anode still faces a main challenge, e.g., the limited reversible capacity. This inspired us to fabricate composite by combing the advantages of MOF glass and high-capacity Si materials to obtain high-performance anodes.

Recent progress in developing Si@MOF composite has dramatically enlarged the design space for anode materials [13–16]. Although crystalline MOFs have been utilized in fabricating the Si@MOF composites, the glassy MOF/Si composites have not been reported to the best of our knowledge [13,14]. In this work, we first applied a reflux technique (see Experimental section) to prepare Si nano particles@cobalt-ZIF-62 composites. Then we heated them to 450 °C, at which cobalt-ZIF-62 was melted and subsequently quenched to glass state, and thus the Si@calbolt-ZIF-62-glass composites (SiZGC) were obtained. This fabrication process involves wrapping Si nano particles into ZIF-62 and melt quenching treatment. We chose ZIF-62 as the precursor since it can be easily melt-quenched to glass state with a disordered open network, benefiting to the Li-ion storage and transfer [12,17,18]. Si nano-particles increased the yield of ZIF-62 by providing heterogeneous nucleation sites for ZIF crystal formation. Thus, a synergistic effect was achieved for the composite-based anode, which led to a rather high reversible capacity (650 mA h $g^{-1}$ at 1 A $g^{-1}$ after 500 cycles). This capacity is about 3 times higher than that of ZIF glass, 6 times that of ZIF crystal, and 30 times that of pure Si-based anodes. The strategy used in this work not only buffered the volume expansion and the aggregation of Si nano particles during cycling, but also made full use of ZIF-62 glass for lithium storage. We clarified the structural origin of the enhancement of the capacity in the derived composite-based anodes.

## 2. Experimental section

### 2.1. Synthesis of samples

Cobalt-ZIF-62 crystal (Z) was synthesized by conventional solvothermal method [18–20]. The cobalt-ZIF-62 glass (ZG) was obtained by heating the Z at 10 °C·$min^{-1}$ in argon to 450 °C and calcined at this temperature for 5 mins followed by cooling naturally to room temperature [12]. Instead of using the solvothermal method, Si@cobalt-ZIF-62 composite (SiZC) was prepared via a reflux method, which involves: 1) heating the chemically reacting solution for a period at a certain temperature; 2) condensing the vapor to liquid state via a pipe. In detail, imidazole (Im, 11.55 mmol, 785.4 mg), benzimidazole (BIm, 1.66 mmol, 196 mg), $C_4H_6CoO_4$•$4H_2O$ (4 mmol, 996 mg), and Si nanoparticles with different amounts (50, 100, 150 mg, accounting for about 5%, 10%, 15 wt% of the final product, respectively), were added to 90 mL *N,N*-dimethylformamide (DMF). Then the solution was heated at 130 °C for 48 hrs while refluxing and stirring. After cooling naturally to room temperature, the SiZC was obtained by centrifugation and vacuum drying. The SiZC was melt-quenched using the same procedure as that vitrifying the Z to obtain Si@cobalt-ZIF-62-glass composite (SiZGC), in which Si remains crystalline. The samples are named according to the weight percentage of Si in composite. For example, 5SiZGC refers to the SiZGC containing 5 wt% Si. The detailed preparation procedures are given in Table 1.

### 2.2. Materials characterizations

The phases of the samples were identified on a PANalytical X-ray diffractometer with Cu Kα (λ = 1.5406 Å) radiation during the 2θ range of 5–70° with a step size of 0.013°. To investigate the characteristic temperature of glassy material, i.e., glass-transition temperature, the differential scanning calorimeter (DSC) (Jupiter 449 C, Netzsch) measurements were conducted at 10 °C·$min^{-1}$ in argon to 450 °C. The Raman spectroscopy measurements were conducted via Renishaw In-Via Raman microscopic with an $Ar^+$ laser (λ = 532 nm). Fourier transform infrared (FTIR) spectra were recorded on a Bruker TENSOR II FTIR spectrometer with Platinum ATR Accessory at room temperature in the range of 400–4000 $cm^{-1}$. To study the chemical environment of Co, Si, C, N, O in anodes before and after discharging/charging cycling, X-ray photoelectron spectroscopy (XPS) measurements were performed using ESCALAB 250Xi spectrometer (ThermoFisher Scientific, USA) with nonmonochromatic Al Ka X-ray (1486.6 eV) at pass energy of 50 eV. The morphologies and element distributions of samples were analyzed using field-emission scanning electron microscopy (FE-SEM) (Supra-55, Zeiss Inc.), transmission electron microscopy (TEM) (JEOL Ltd., Japan) and X-ray energy dispersive spectroscopy (EDS) (X-Max, OXFORD Instruments Inc.).

### 2.3. Cell assembly and electrochemical evaluation

The electrochemical performances of the obtained samples were evaluated by using CR2032 coin cells with lithium foil (diameter of 10.0 mm) as the counter/reference electrode. A uniform slurry consisting of 70 wt% active materials (the as-prepared ZIFs or Si@ZIFs), 20 wt% acetylene black, and 10 wt% polyvinylidene difluorides (PVDF) were prepared in N-methyl-2-pyrrolidone (NMP) and then pasted onto a copper foil substrate via a doctor blade and dried at 110 °C in a vacuum oven for 12 h to obtain working electrodes. The loading amount of active materials was 1~2 mg. 1 M $LiPF_6$ in ethylene carbonate (EC)/diethyl carbonate (DEC)/dimethyl carbonate (DMC) (1:1:1 vol%) and a Celgard 2325 membrane (diameter of 19.0 mm) were used as the electrolyte and separator, respectively. The cells were assembled in an argon-filled glovebox with both the moisture and the oxygen content lower than 0.1 ppm and then the cells were tested at 25 °C. The galvanostatic charging/discharging tests of the samples were conducted on a Land battery test system (CT2001A) within the voltage range 0.01–3 V. Cyclic voltammetry (CV) curves were obtained in the voltage range of 0.01–3 V

**Table 1**
The preparation procedures of the cobalt-ZIF-62 crystal (Z), cobalt-ZIF-62 glass (ZG), Si@cobalt-ZIF-62 composite (SiZC), and Si@cobalt-ZIF-62-glass composite (SiZGC).

| Sample Names | Preparation Procedures | | Melt-Quenching |
|---|---|---|---|
| | Solvothermal | Reflux | |
| Z | √ | – | – |
| ZG | √ | – | √ |
| SiZC | – | √ | – |
| SiZGC | – | √ | √ |

at the scanning rate of 0.1 mV $s^{-1}$. EIS spectra were recorded in the frequency range of 0.1 Hz–100 kHz on CHI 760e electrochemical workstation. All electrochemical measurements were repeated with different batches of samples to confirm the reproducibility of their performances.

## 3. Results and discussion

Scheme 1 illustrates the fabrication process of the Si@cobalt-ZIF-62-glass composite (SiZGC). First, the raw materials including organic ligand, metal ions, and Si nano-powder, were dispersed in the DMF, and then reflux at 130 °C for 2 days to precipitate the Si@ZIF-62 composite (SiZC) (see Experimental section). The Si nanoparticles act as hetero-nucleation sites for growing ZIF layer. Second, the obtained SiZC was heated to 450 °C at 10 °C·$min^{-1}$ in argon and then cooled down naturally, leading to the SiZGC formation. Finally, Si nanoparticles with a size distribution of 20~60 nm were encapsulated in ZIF glass matrix, resulting in a robust structure that buffers the volume changes of Si during lithiation/delithiation processes.

The morphologies and microstructures of samples 10SiZC and 10SiZGC were examined using field emission scanning electron microscopy (FE-SEM), as shown in Fig. 1. For 10SiZC (Fig. 1a), ZIF particles with a size of ~10 μm are observed, in which Si nanoparticles are wrapped, as verified by EDS elemental mappings of Co, N, and Si. Thus, SiZC was obtained by the facile reflux method. The SEM image of 10SiZGC (Fig. 1b) reveals that the ZIF cages remain owing to the high viscosity of ZIF melt, and hence, the morphologies of 10SiZGC are similar to those of 10SiZC. In addition, the enlarged image (Fig. 1b) indicates that small Si particles are covered by ZIF-62 glass.

To obtain the crystallographic information on the studied samples, X-ray diffraction (XRD) measurements were conducted (Fig. 2a). In the XRD patterns of Z and 10SiZC, sharp diffraction peaks can be seen in the range of 10°~25°, coinciding with those in the simulated ZIF-62 [12]. Moreover, the Bragg diffraction peaks associated with Si were also observed in 10SiZC, further confirming the wrapping of nano Si particles by crystalline ZIF-62. In contrast, the XRD patterns of sample ZG show no diffraction peaks, indicating its amorphous nature. While the diffraction peaks for Si crystals also appear in the XRD pattern of 10SiZGC sample. Thus, ZIF-62 becomes amorphous while Si remains crystalline in 10SiZGC upon melt-quenching. That is, the melt-quenching method did not affect the crystal structure of Si.

Fig. 2b shows the DSC upscan curves of Z, ZG, 10SiZC and 10SiZGC samples obtained at 10 °C $min^{-1}$ in argon. For both Z and 10SiZC, the DSC curve of each sample exhibits an endothermic peak at around 280 °C due to the release of solvent, followed by another endothermic peak at 420 °C associated with the melting event. However, a different scenario is observed for both ZG and 10SiZGC samples, i.e., the glass transition occurs at ~330 °C, implying that the vitrification of ZIF in 10SiZC is not affected by introducing Si. To evaluate the thermal stability, thermogravimetry (TG) curves of Z, ZG, 10SiZC, and 10SiZGC were collected. As shown in Fig. S1, significant mass loss occurs in both Z and 10SiZC in the temperature range of 150–300 °C owing to the solvent (DMF) release, while no mass loss is seen in both ZG and 10SiZGC as the solvent was already released during the glass preparation process.

The FTIR spectra of Z, ZG, 10SiZC and 10SiZGC in Fig. 2c show the similar frequencies of intramolecular vibrations, indicating that the integrity of organic linkers in ZIFs are preserved during melt-quenching [19]. However, structural changes take place during transformation of crystal into glass (Fig. 2c). First, the peaks at around 430 and 835 $cm^{-1}$ correspond to Co-N bonds and the in-plane bending of aromatic rings, respectively [12,21], and both peaks shift to a lower wavenumber after vitrification, suggesting that both Co-N bonds and aromatic rings become weaker in ZG and 10SiZGC. Second, the intensity ratio between the 668 and 1082 $cm^{-1}$ peaks increases and the two peaks are attributed to the ring deformation out-of-plane-bending in the organic ligands and the C-H bending vibrations, respectively [12]. This implies an increased distortion in glass samples. Third, the peaks at 1383 and 1675 $cm^{-1}$ arising from vibrational mode of C-H and the carbonyl groups of solvent molecules (DMF) disappear upon vitrification [12,22]. This indicates that the DMF molecules have escaped from Z or 10SiZC during melt-quenching, agreeing with the DSC results. It is worth noting that the Si-Si bonds were not detected in FTIR spectra for 10SiZC and 10SiZGC since Si is FTIR-inactive. However, the strong peak at ~517 $cm^{-1}$ assigned to Si-Si bonds [23] was observed in Raman spectra (Fig. 2d) for those two samples, verifying the existence of Si in the target composites.

To evaluate the anode performances of the Si@ZIF composites, the cycling experiments of the commercial nano-Si, Z, ZG, 5SiZC, 5SiZGC, 10SiZC, 10SiZGC, 15SiZC, and 15SiZGC based anodes were performed at a current density of 1 A $g^{-1}$ (Fig. 3a). The specific capacity of almost every sample decays distinctly within about 50 cycles and then increases dramatically, except for the Si and Z based anodes which deliver rather low capacities. Specifically, the Si-doped composite samples exhibit remarkably higher capacities than those of the corresponding pure ZIF-crystal/glass and Si. This implies that the co-existence of ZIF layer and Si leads to a synergistic effect that benefits both Li-ion storage and transport. Specifically, the ZIF layer can protect Si from pulverization by buffering the volume changes during charging/discharging cycles, while Si provides large specific capacity. In addition, the ZIF glass-containing composites show higher capacities than the samples with ZIF crystal, except for the samples doped with 15 wt% Si. The capacity of 650 mA h $g^{-1}$ of 10SiZGC based anode can be reached at 1 A $g^{-1}$ after 500 cycles, i.e., it is more than three times that of ZG (210 mA h $g^{-1}$), six times that of pristine ZIF crystal (108 mA h $g^{-1}$), and 30 times that of pure Si (20 mA h $g^{-1}$). This is a remarkable enhancement, considering that the specific capacities are calculated based on the mass of the total

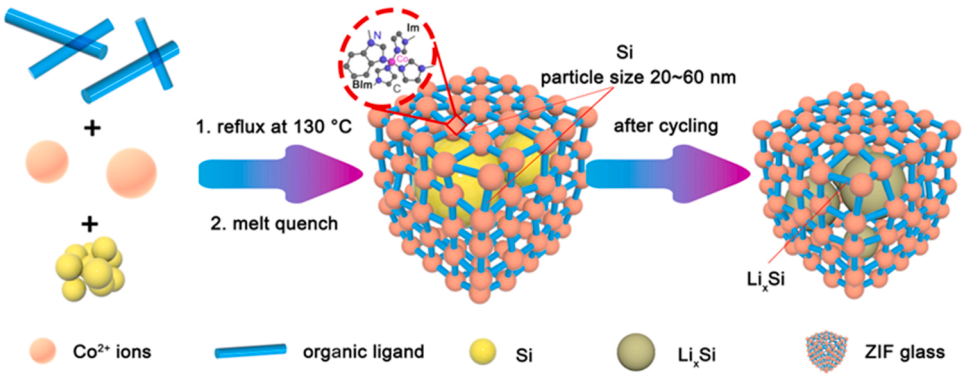


**Scheme 1.** Schematic illustration of the synthesis process of the Si@cobalt-ZIF-62-glass composite (SiZGC) and the protecting role of ZIF glass matrix, which prolongs the cycling life of Si.

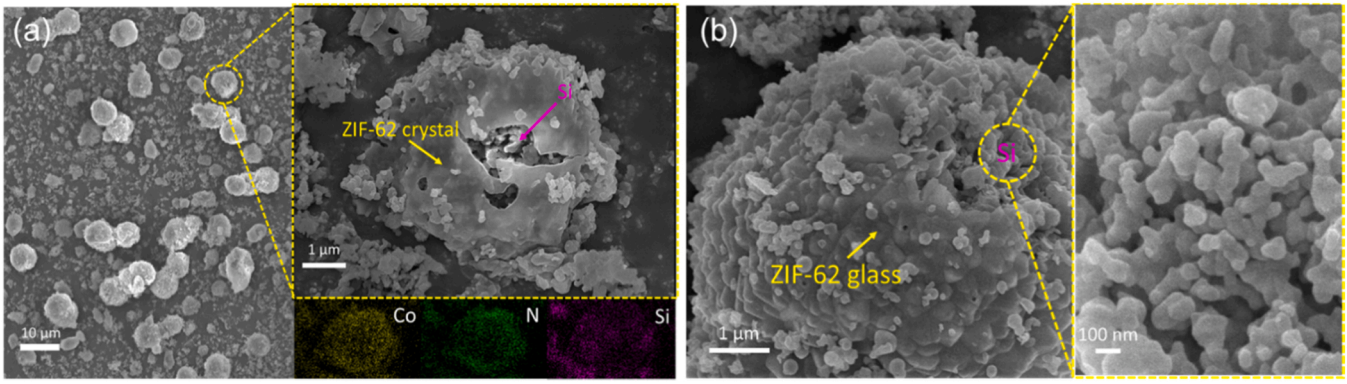


**Fig. 1.** Microscopic characterizations. (a) SEM images of the 10Si@cobalt-ZIF-62 composite (10SiZC) (Inset: EDS elemental mappings of Co, N and Si for SZ), where the number, i.e., 10, represents the introduction of 10 wt% Si nanoparticles into ZIF-62; (b) SEM images of the 10Si@cobalt-ZIF-62-glass composite (10SiZGC).

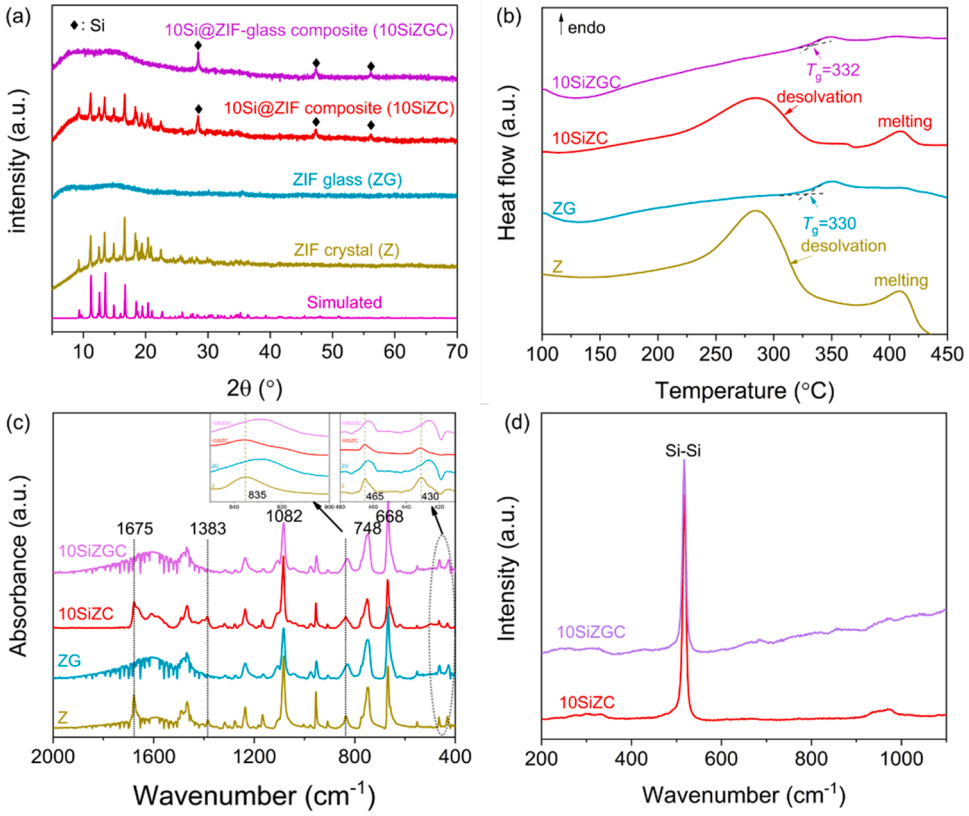


**Fig. 2.** Phase, thermal and structure analyses of the ZIF crystal (Z), ZIF glass (ZG), 10Si@ZIF composite (10SiZC), and 10Si@ZIF-glass composite (10SiZGC). (a) XRD patterns along with that of simulated ZIF-62. (b) DSC upscan curves which were obtained at 10 °C min$^{-1}$ in argon. (c) FTIR spectra. (d) Raman spectra of 10SiZC and 10SiZGC.

active material - Si@ZIF composite, and only ~10 wt% of Si exists in the active material for 10SiZGC. This means that 10 wt%Si contributes around 400 mA h g$^{-1}$ to the total capacity, which almost reaches the theoretical capacity of 10%Si as that of pure Si is ~4000 mA h g$^{-1}$. In addition, 10SiZC and 5SiZGC also show high capacities, reaching 600 and 550 mA h g$^{-1}$ after 500 cycles at 1 A g$^{-1}$, respectively. All these results not only suggest that the Si@ZIF composite exhibits a synergistic effect (i.e., a combination of high capacity and high cycling stability) compared with pure Si and ZIFs [2,12], but also indicate the important role of ZIF glass in protecting Si in the composite. Fig. S2 shows the cycling performance of 10SiZGC after 1000 cycles at 1 A g$^{-1}$. Apparently, the capacity of 10SiZGC did not rise all the way but peaked at 660 mA h g$^{-1}$ after 570 cycles and then declined to 450 mA h g$^{-1}$ after 1000 cycles. This could be attributed to structural evolution of ZIF and the pulverization of Si during lithiation/delithiation.

To probe the electrochemical performances of 5SiZC, 10SiZC, 15SiZC, 5SiZGC, 10SiZGC, and 15SiZGC samples, we also investigated their rate capabilities (Fig. 3b). The results suggest the excellent kinetics of the SiZGC-based anodes at different current densities up to 5 A g$^{-1}$. As expected, 15SiZGC, 10SiZGC, and 5SiZGC manifested outstanding high-rate capability compared with other samples, delivering the favorable average capacities of 666, 516, and 482 mA h g$^{-1}$ after 10 cycles at 0.1 A g$^{-1}$, respectively. This can be explained in terms of the amounts of doping Si and the effects of ZIF glass. The glass phase provides more Li-ion intercalation sites arising from increased distortion and defects compared with crystalline ZIF [12]. With a stepwise increase in the

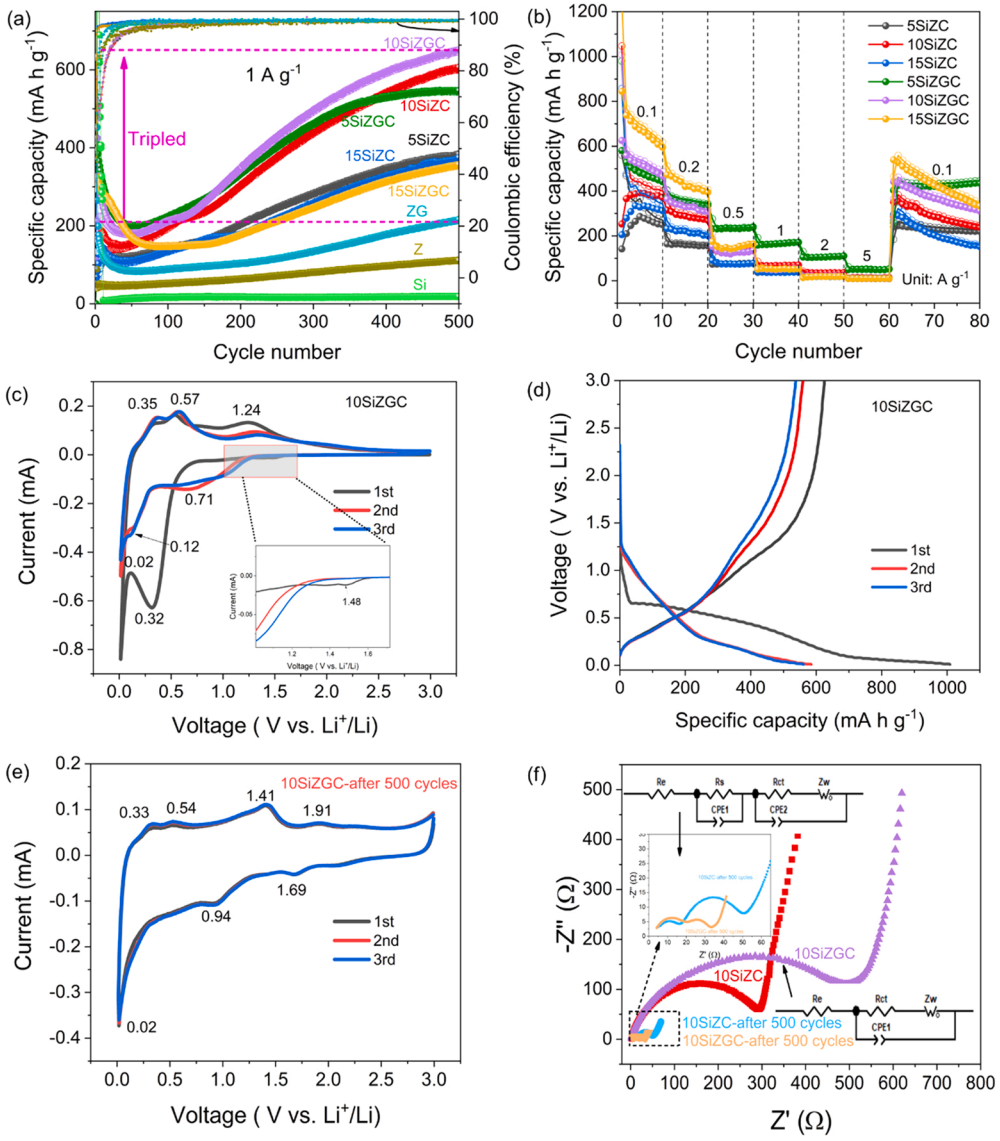


**Fig. 3.** Electrochemical Performances. (a) The cycling performance of anodes based on the ZIF crystal (Z), ZIF glass (ZG), 5Si@ZIF composite (5SiZC), 5Si@ZIF-glass composite (5SiZGC), 10Si@ZIF composite (10SiZC), 10Si@ZIF-glass composite (10SiZGC), 15Si@ZIF composite (15SiZC), 15Si@ZIF-glass composite (15SiZGC), where the numbers, i.e., 5, 10, 15, represent that weight percent of Si nanoparticles introduced into ZIF-62, respectively, at 1 A $g^{-1}$ for 500 cycles. (b) Rate performance of 5SiZC, 5SiZGC, 10SiZC, 10SiZGC, 15SiZC, and 15SiZGC at current densities of 0.1, 0.2, 0.5, 1, 2, 5 and 0.1 A $g^{-1}$. (c) Cyclic Voltammetry (CV) curves of pristine 10SiZGC within the range from 0.01 to 3.0 V at a scan rate of 0.1 mV $s^{-1}$. (d) Galvanostatic charge-discharge voltage profiles of 10SiZGC for three cycles at the current density of 0.1 A $g^{-1}$. (e) Cyclic Voltammetry (CV) curves of 10SiZGC after 500 cycles within the range from 0.01 to 3.0 V at a scan rate of 0.1 mV $s^{-1}$. (f) Nyquist plots of 10SiZC and 10SiZGC before and after cycling obtained from electrochemical impedance spectra within frequency range from 0.01 Hz to 100 kHz.

current density, the average capacity decreases for all the samples, among which 5SiZGC exhibits the highest capacity retention after cycles at 0.5, 1, 2, and 5 A $g^{-1}$. In addition, when the current density was set back to 0.1 A $g^{-1}$, the specific capacity of 5SiZGC can recover to 432 mA h $g^{-1}$ and remains stable in the following cycles, indicating a superior rate performance. In contrast, both 15SiZGC and 10SiZGC are sensitive to the current density and show a rapid decline in capacity retention rate with an increase of the current density. When the current density was switched back to 0.1 A $g^{-1}$, the capacities of 15SiZGC and 10SiZGC restore to 540 and 440 mA h $g^{-1}$, respectively, and decrease slowly in the following cycles. This could be explained as follows. Although the Si content in 15SiZGC and 10SiZGC is higher than that in 5SiZGC, not all the Si nanoparticles in the composite contributed to the capacity increase within the studied 80 cycles in the test of rate capability. When introducing more Si into the composite, e.g., 10SiZGC, the glassy ZIF cages simply cannot accommodate all Si, as shown in Fig. 1a. The additional Si particles will aggregate and collapse during lithiation/delithiation because no ZIF protection layer exists, resulting in a capacity decline.

The cyclic voltammetry (CV) measurements of 10SiZGC at a scan rate of 0.1 mV $s^{-1}$ were carried out to investigate the electrochemical reaction, as shown in Fig. 3c. In the first cathodic scan, there are three distinct reduction peaks at around 1.48, 0.32, and 0.02 V, which are attributed to the storage of $Li^+$ within ZIF, formation of solid electrolyte interface film (SEI), and formation of $Li_xSi$ phase, respectively [24–27]. During the anodic reaction, the peaks at around 0.35 and 0.57 V are ascribed to dealloying of $Li_xSi$ to Si, while the peak at ~1.23 V comes from the extraction of $Li^+$ from ZIF glass [12,27]. In the subsequent two CV curves, the pair of redox peaks (~0.71 versus ~1.24 V) arises from reversible insertion or extraction of $Li^+$ into/from ZIF glass, whereas both the 0.12 vs 0.57 V pair and the 0.02 vs 0.35 V pair are associated with the alloying-dealloying processes of Si/$Li_xSi$ [28]. Fig. 3d shows the typical galvanostatic discharge/charge voltage profiles in the first three cycles of 10SiZGC anode at 0.1 A $g^{-1}$. The observed plateau voltage in the profiles is consistent with the peak voltage in the CV curves. The initial discharge and charge capacities were 1010 and 627 mA h $g^{-1}$, respectively, giving the first Coulombic efficiency of 62%, and the irreversible capacity loss may be due to the formation of the SEI layer and other irreversible reactions [29].

To clarify why the capacity of 10SiZGC continuously increases during 500 cycles, three CV cycling of 10SiZGC after 500 charging/discharging cycles were performed (Fig. 3e). Remarkably, compared with the redox peaks in the CV profiles of the fresh battery (Fig. 3c), a new couple of redox peaks appear, i.e., (1.69 vs 1.91 V), which can be

ascribed to the reversible insertion/extraction of $Li^+$ into/from ZIF glass [30]. This indicates that the ZIF glass is gradually activated for lithium storage as a result of the charging/discharging cycling, which contributed to the enhancement of the capacity. Moreover, the redox peaks located at ~0.71 and ~1.24 V in Fig. 3c shift to higher voltages, i.e., ~0.94 and ~1.41 V (Fig. 3e). The peak at 0.12 V in the second cathodic curve in Fig. 3c does not appear in Fig. 3e, implying the gradual structural changes in both ZIF glass and Si with cycling. In addition, the overlapping of three CV curves in Fig. 3e indicates the reversibility of 10SiZGC after 500 cycles.

To understand the origin of the electrochemical performance enhancement in 10SiZGC upon cycling, the electrochemical impedance spectroscopy (EIS) measurements of 10SiZC and 10SiZGC before and after 500 cycles were performed (Fig. 3 f). All the Nyquist plots consist of one or two depressed semicircles in the high frequency region and an inclined line in the low frequency region. The equivalent circuit for the Nyquist plots is given in the inset of Fig. 3 f, where $R_e$, $R_s$, $R_{ct}$, $C_{PE}$ and $Z_w$ represent the ohmic resistance, SEI resistance, charge transfer resistance, interface capacitance and diffusion impedance of the half-cell systems, respectively [12,29]. The fitted parameters are shown in Table S1. It is seen that the charge transfer resistance ($R_{ct}$) of 10SiZC and 10SiZGC decreases from 290.4 and 405.3 Ω to 29.7 and 10.8 Ω after 500 cycles, respectively, indicating the increased electrical conductivity. In addition, the depressed semicircle in each EIS curve of 10SiZC and 10SiZGC splits into two consecutive ones after cycling. The semicircle in the higher frequency region arises from the SEI impedance ($R_s$ and $C_{PE1}$). The line inclined at approximately 45° in the low frequency region corresponds to the Warburg impedance ($W$), which is associated with the diffusion coefficient of $Li^+$ in the electrode material. Warburg factor ($\sigma$) can be determined from the linear relation between impedance Z′ and the reciprocal square root of the angular frequency $\omega$ (Fig. S3). As shown in Fig. S3, the $\sigma$ values of 10SiZC and 10SiZGC before and after cycling are 191.78, 320.88, 32.36, and 14.16, respectively. The declined σ value after cycles suggests a larger $Li^+$ diffusion coefficient [12,31].

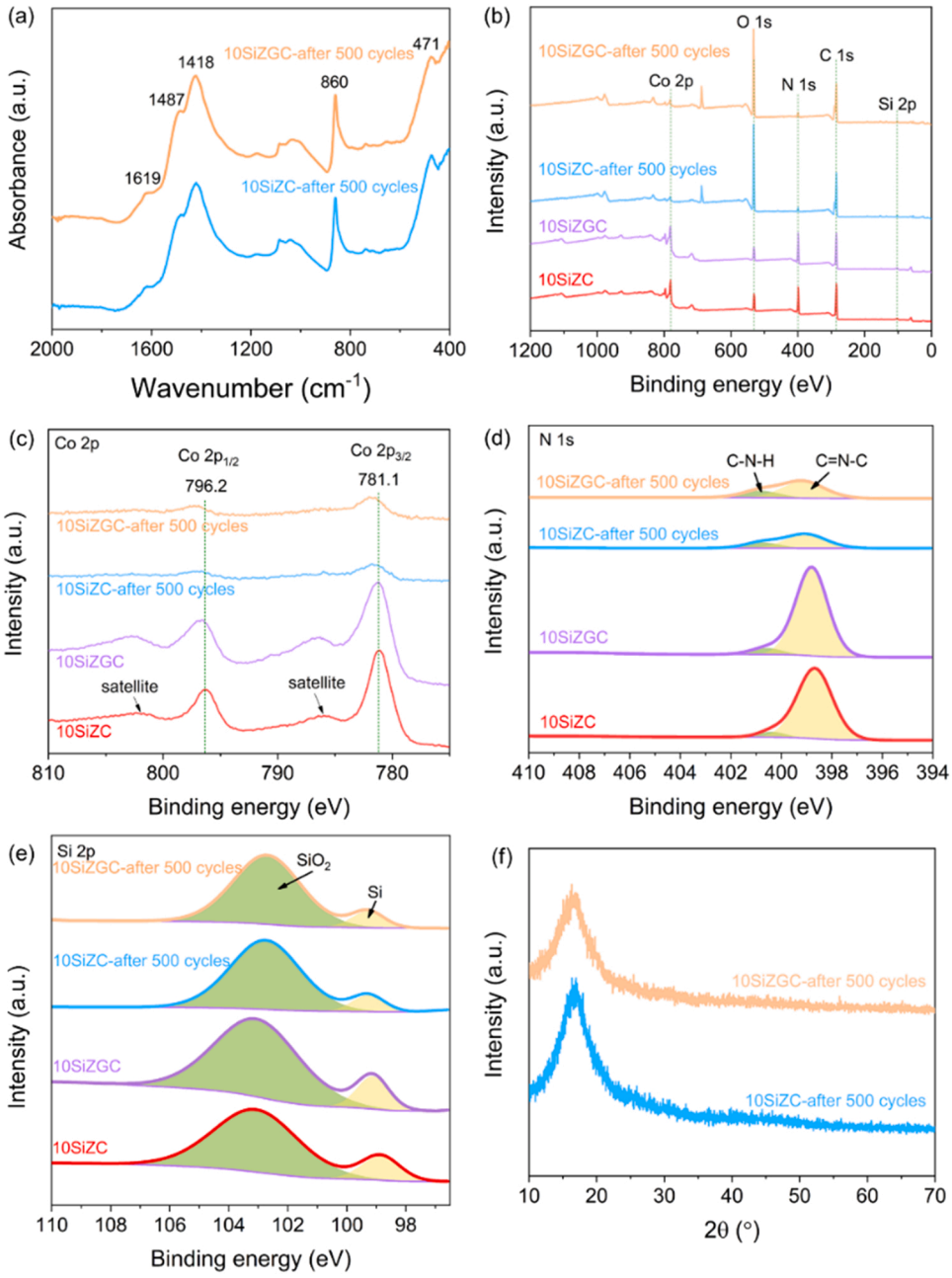


**Fig. 4.** Structure and phase analyses. (a) FTIR spectra of the 10Si@ZIF composite (10SiZC) and 10Si@ZIF-glass composite (10SiZGC) after cycling, where the number (10) represents that 100-mg Si nanoparticles were added into ZIF-62, accounting for about 10% of the final product by weight. (b)~(e) XPS survey spectra and high-resolution core level of Co 2p, N 1 s, Si 2p spectra for 10SiZC and 10SiZGC before and after cycling, respectively. (f) XRD patterns of 10SiZC and 10SiZGC after 500 cycles.

The above EIS results indicate that both the electron transfer rate and $Li^+$ diffusion coefficient of 10SiZC and 10SiZGC are greatly enhanced by cycling.

To investigate the structural evolutions of 10SiZC and 10SiZGC after cycling, FTIR spectra were collected. As shown in Fig. 4a, 10SiZC exhibits similar FTIR spectrum to that of 10SiZGC, indicating that both samples have similar structural features after cycling. It is known that the peaks at around 430, 668, 748 and 835 $cm^{-1}$ for the pristine 10SiZC and 10SiZGC (Fig. 2c) are attributed to the Co-N bonds, the ring deformation out-of-plane-bending in the organic ligands, the benzene group of imidazole/benzimidazole, and the in-plane-blending of aromatic ring, respectively [12,21,32]. However, these peaks disappeared in the spectra of the two samples after 500 cycles. This suggests the breakages of the Co-N bonds and rings in the organic ligand after cycling. In addition, the peaks at 471, 860, and 1418 $cm^{-1}$ are ascribed to aromatic C-H bonds, isolated aromatic H vibrations, and ring stretch of organic ligands, respectively [21,33–35], while the peaks at 1487 and 1619 $cm^{-1}$ are attributed to stretching of C-C in the benzimidazole aromatic ring (Fig. 4a) [36].

The surface elemental analyses of 10SiZC and 10SiZGC before and after cycling are carried out by the X-ray photoelectron spectroscopy (XPS) survey spectrum (Fig. 4b), and thereby the existence of Co, N, Si, C and O elements is confirmed, agreeing with the EDS results (Fig. 1). It is seen that the O 1 s signal of the samples after cycling become stronger, and this mainly originate from the SEI (products from electrolyte decomposition). Fig. 4c exhibits the high-resolution spectrum of Co 2p, in which the Co $2p_{1/2}$ and Co $2p_{3/2}$ peaks of both 10SiZC and 10SiZGc samples are located at 796.2 and 781.1 eV with two satellite peaks at 802.1 and 786.0 eV, suggesting the existence of $Co^{2+}$ in both samples. After cycling, these two peaks (796.2 and 781.1 eV) slightly shift to higher binding energy compared with those of pristine samples, implying that the chemical environment of cobalt in 10SiZC and 10SiZGC varies upon insertion/extraction of $Li^+$ and this could be due to the distortion and local breakage of the Co-N [12]. In Fig. 4d, the peak of N 1 s in the XPS spectrum is deconvoluted into two peaks at 398.7 and 400.4 eV, which are attributed to C═N-C and C-N-H bonds, respectively [12,37]. The fractions of the two bonds are shown in Table S2. 10SiZC shares a similar fraction of the C═N-C bonds (i.e., about 94%) with that in 10SiZGC before cycling. However, the C═N-C bond fractions in both samples dramatically decrease to around 73% after cycling, implying the breakage of C═N-C upon insertion/extraction of $Li^+$. This agrees well with the FTIR results (Fig. 4a). For the high-resolution XPS spectrum of C 1 s (Fig. S4), the peaks of pristine 10SiZC and 10SiZGC can be deconvoluted into two peaks assigned to C-C/C═C/C-H at 284.8 eV and N═C-N at 286 eV, respectively. In contrast, the C 1 s spectra of 10SiZC and 10SiZGC vary significantly upon cycling, which can be deconvoluted into four peaks. Besides the peak at 284.8 eV, three new peaks appear at 286.6, 288.5, and 290.1 eV, which are related to C-O/N═C-N, O-C═O/C-F, and $Li_2CO_3$ or lithium alkyl carbonates, respectively, as consequences of both the addition of PVDF as anode binder and the formation of SEI during cycling [12,38–40]. Fig. 4e shows the core level spectra of Si 2p in 10SiZC and 10SiZGC before and after cycles, which exhibit similar characteristics. The peak deconvolution results are shown in Table S3. The XPS peak associated with $SiO_2$ can be observed in all the composite samples, implying the existence of $SiO_2$. However, $SiO_2$ is predominant only in the surface layer (< 5 nm) considering the detection depth limit of XPS. The formation of the thin $SiO_2$ layer is due to the high tendency of Si to be oxidized when exposed to air, even at room temperature [41]. The existence of $SiO_2$ was also verified by the FTIR results (Fig. S5). Overall, the fraction of $SiO_2$ in the as-purchased Si is still much smaller than that of Si. Fig. 4f shows the XRD patterns of 10SiZC and 10SiZGC after 500 cycles. A broad peak at $2\theta \approx 16^\circ$ appears in each pattern, implying the transformation of crystalline ZIF in 10SiZC sample and crystalline Si in both samples into amorphous materials upon cycling.

To detect the morphologies of 10SiZGC and 10SiZC after 500 cycles at 1 A $g^{-1}$, SEM and HRTEM measurements were conducted (Fig. 5 and Fig. S6). The overall skeleton of ZIF in 10SiZGC after cycling is preserved and Si particles are still wrapped within ZIF glass, and this is confirmed by the upper right inset, TEM image and EDS mappings in Fig. 5a. The HRTEM image and the selected area electron diffraction (SAED) patterns demonstrate the existence of a large amount of amorphous phase and few crystals with a size of 10∼20 nm in 10SiZGC after cycling, as shown in Fig. 5b. The lattice fringes with an interatomic spacing of ∼0.31 nm is attributed to Si, implying that the insertion/extraction of $Li^+$ ions results in the majority of Si in 10SiZGC converting to an amorphous state after 500 cycles. In addition, Fig. S6 shows that the cycled 10SiZC exhibits a similar scenario as 10SiZGC, i.e., a large amount of amorphous phase and few Si crystals, suggesting that not only Si crystals, but also ZIF crystals in 10SiZC transform into amorphous phases upon cycling.

The above results clearly demonstrate the enhanced capacity and rate performance of SiZGC as an anode material for lithium storage [9,12], and this is achieved by designing and fabricating the Si@ZIF-62 glass composite, in which nano Si is wrapped and protected by porous ZIF glass phase. First, cobalt-ZIF-62 glass possesses an open disordered network structure, which provides more active sites and channels for both storage and transport of $Li^+$ compared to their crystalline counterparts. Second, the ZIF glass encapsulates Si nano particles to buffer the volume fluctuations of Si during the charging/discharging cycling, thereby realizing excellent cycling performances. In detail, the ZIF glass layer not only stores $Li^+$ ions, but also suppresses the alloying of $Li^+$ with wrapped Si to some extent, and also reduces volume change of Si via confinement, and thereby lowers the degree of pulverization of Si in the composite. Even if the wrapped Si nanoparticles are pulverized after cycling (as shown in Scheme 1), a substantial amount of Si is still attached to the inner surface of ZIF glass, and thus the composite structure can remain in a good electrical contact with the copper current collector. Such good contact can facilitate the electron transfer to ensure the alloying process between $Li^+$ and Si. Third, the insertion/extraction of $Li^+$ could result in the distortion or breakage of Co-N, and aromatic rings in ZIF, leading to an increase in structural defects and diffusion channels for the transport and storage of $Li^+$ [12,42]. Moreover, the increased channels lead to more $Li^+$ ions going into ZIF and reacting with Si, thereby highly enhancing the reversible capacity and rate capability.

## 4. Conclusions

We designed and fabricated the Si@ZIF-glass composite compromising interior high-capacity Si nano particles and exterior ZIF glass phase for lithium storage, which yields a strong synergistic effect. Such a unique architecture in ZIF glass buffers the volume changes of Si and thus prevents its pulverization, and hence promotes the transport kinetics for both electrons and lithium ions. In addition, ZIF glass itself also enhanced the electrochemical performance of Si@ZIF-glass based anode owing to its open network structure that facilitates the $Li^+$ ion diffusion and storage. As a consequence, 10SiZGC based anode exhibits the capacity of 650 mA h $g^{-1}$, which is about three times and six times as high as that of ZIF glass and ZIF crystal at the current density of 1 A $g^{-1}$ after 500 cycles, respectively. Our findings paved a new avenue for developing anode material for the next generation of high-performance LIBs. Moreover, our approach to construct hierarchical Si@ZIF-glass composite could be further extended to other types of ZIF glasses to combine with highly active materials like Sn and $SnO_2$ for application in electrochemical energy storage.

## CRediT authorship contribution statement

**Jiajia Yan**: Conceptualization, Methodology, Investigation, Data curation, Writing – original draft. **Chengwei Gao**: Conceptualization, Methodology, Data curation, Writing – review & editing. **Shibin Qi**: Data curation, Validation. **Zhenjing Jiang**: Data curation. **Lars**

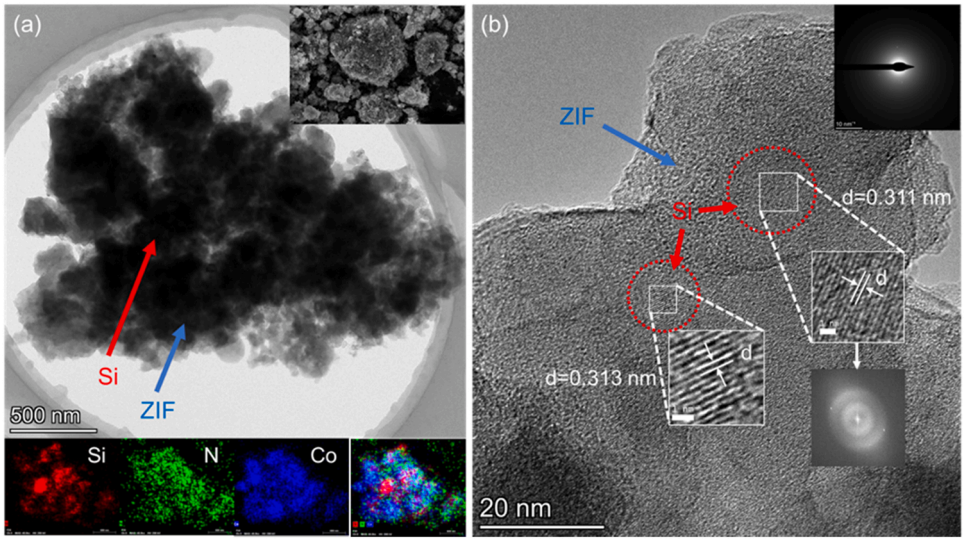


**Fig. 5.** Microscopic characterization. (a) SEM image (the upper right inset), TEM image and EDS mappings of Si, N, Co for 10SiZGC after cycling. (b) HRTEM image and the corresponding SAED patterns of 10SiZGC after cycling.

**Rosgaard Jensen**: Data curation. **Hongbing Zhan**: Data curation. **Yanfei Zhang**: Data curation, Supervision, Writing – review & editing. **Yuanzheng Yue**: Conceptualization, Project administration, Supervision, Writing – review & editing.

## Declaration of Competing Interest

The authors declare that they have no known competing financial interests or personal relationships that could have appeared to influence the work reported in this paper.

## Data availability

Data will be made available on request.

## Acknowledgments

Authors would like to acknowledge support by China Scholarship Council (201906650022). Y.F.Z. would like to acknowledge support by Taishan Youth Scholar Project of Shandong Province (tsqn202103098) and the Shandong Provincial Natural Science Foundation (ZR2020ME025). Authors would also like to thank Prof. H.Z. Tao and Prof. A. Qiao for their help with SEM and XPS tests, and Dr. Z.H. Zheng and Y.X. Zhuang for their help with TEM measurements.

## Appendix A. Supporting information

Supplementary data associated with this article can be found in the online version at doi:10.1016/j.nanoen.2022.107779.

## References

[1] S. Chae, S.H. Choi, N. Kim, J. Sung, J. Cho, Integration of graphite and silicon anodes for the commercialization of high-energy lithium-ion batteries, Angew. Chem. Int. Ed. 59 (1) (2020) 110–135, https://doi.org/10.1002/anie.201902085.
[2] Y. Zhang, J. Ren, T. Xu, A. Feng, K. Hu, N. Yu, Y. Xia, Y. Zhu, Z. Huang, G. Wu, Covalent bonding of Si nanoparticles on graphite nanosheets as anodes for lithium-ion batteries using diazonium chemistry, Nanomaterials 9 (12) (2019) 1741, https://doi.org/10.3390/nano9121741.
[3] Y. Xu, Y. Zhu, C. Wang, Mesoporous carbon/silicon composite anodes with enhanced performance for lithium-ion batteries, J. Mater. Chem. A 2 (25) (2014) 9751–9757, https://doi.org/10.1039/c4ta01691b.
[4] D.H.S. Tan, Y.-T. Chen, H. Yang, W. Bao, B. Sreenarayanan, J.-M. Doux, W. Li, B. Lu, S.-Y. Ham, B. Sayahpour, J. Scharf, E. A.Wu, G. Deysher, H.E. Han, H.J. Hah, H. Jeong, J.B. Lee, Z. Chen, Y.S. Meng, Carbon-free high-loading silicon anodes enabled by sulfide solid electrolytes, Science 373 (2021) 1494–1499, https://doi.org/10.1126/science.abg7217.
[5] Y. Ding, Z.P. Cano, A. Yu, J. Lu, Z. Chen, Automotive Li-ion batteries: current status and future perspectives, Electrochem. Energy Rev. 2 (1) (2019) 1–28, https://doi.org/10.1007/s41918-018-0022-z.
[6] F. Chen, J. Han, D. Kong, Y. Yuan, J. Xiao, S. Wu, D.-M. Tang, Y. Deng, W. Lv, J. Lu, F. Kang, Q.-H. Yang, 1000 Wh L−1 lithium-ion batteries enabled by crosslink-shrunk tough carbon encapsulated silicon microparticle anodes, Natl. Sci. Rev. 8 (9) (2021), https://doi.org/10.1093/nsr/nwab012.
[7] A. Magasinski, P. Dixon, B. Hertzberg, A. Kvit, J. Ayala, G. Yushin, High-performance lithium-ion anodes using a hierarchical bottom-up approach, Nat. Mater. 9 (4) (2010) 353–358, https://doi.org/10.1038/nmat2725.
[8] M. Ko, S. Chae, J. Ma, N. Kim, H.-W. Lee, Y. Cui, J. Cho, Scalable synthesis of silicon-nanolayer-embedded graphite for high-energy lithium-ion batteries, Nat. Energy 1 (9) (2016) 1–8, https://doi.org/10.1038/nenergy.2016.113.
[9] C. Gao, P. Wang, Z. Wang, S.K. Kær, Y. Zhang, Y. Yue, The disordering-enhanced performances of the Al-MOF/graphene composite anodes for lithium ion batteries, Nano Energy 65 (2019), 104032, https://doi.org/10.1016/j.nanoen.2019.104032.
[10] X. Li, F. Cheng, S. Zhang, J. Chen, Shape-controlled synthesis and lithium-storage study of metal-organic frameworks $Zn_4O$ (1, 3, 5-benzenetribenzoate) 2, J. Power Sources 160 (1) (2006) 542–547, https://doi.org/10.1016/j.jpowsour.2006.01.015.
[11] T. Wei, M. Zhang, P. Wu, Y.-J. Tang, S.-L. Li, F.-C. Shen, X.-L. Wang, X.-P. Zhou, Y.-Q. Lan, POM-based metal-organic framework/reduced graphene oxide nanocomposites with hybrid behavior of battery-supercapacitor for superior lithium storage, Nano Energy 34 (2017) 205–214, https://doi.org/10.1016/j.nanoen.2017.02.028.
[12] C. Gao, Z. Jiang, S. Qi, P. Wang, L.R. Jensen, M. Johansen, C.K. Christensen, Y. Zhang, D.B. Ravnsbæk, Y. Yue, Metal-organic framework glass anode with an exceptional cycling-induced capacity enhancement for lithium-ion batteries, Adv. Mater. 34 (10) (2022), 2110048, https://doi.org/10.1002/adma.202110048.
[13] Y. Han, P. Qi, X. Feng, S. Li, X. Fu, H. Li, Y. Chen, J. Zhou, X. Li, B. Wang, In situ growth of MOFs on the surface of si nanoparticles for highly efficient lithium storage: Si@MOF nanocomposites as anode materials for lithium-ion batteries, ACS Appl. Mater. Interfaces 7 (4) (2015) 2178–2182, https://doi.org/10.1021/am5081937.
[14] Y. Bai, M. Zeng, X. Wu, Y.Q. Zhang, J.W. Wen, J. Li, Three-dimensional cage-like Si@ZIF-67 core-shell composites for high-performance lithium storage, Appl. Surf. Sci. 510 (2020), https://doi.org/10.1016/j.apsusc.2020.145477.
[15] Q. Wei, Y.M. Chen, X.J. Hong, C.L. Song, Y. Yang, L.P. Si, M. Zhang, Y.P. Cai, Saclike-silicon nanoparticles anchored in ZIF-8 derived spongy matrix as high-performance anode for lithium-ion batteries, J. Colloid Interface Sci. 565 (2020) 315–325, https://doi.org/10.1016/j.jcis.2020.01.050.
[16] Q. Wei, Y.M. Chen, X.J. Hong, C.L. Song, Y. Yang, L.P. Si, M. Zhang, Y.P. Cai, Novel bread-like nitrogen-doped carbon anchored nano-silicon as high-stable anode for lithium-ion batteries, Appl. Surf. Sci. 511 (2020), https://doi.org/10.1016/j.apsusc.2020.145609.
[17] L. Longley, S.M. Collins, C. Zhou, G.J. Smales, S.E. Norman, N.J. Brownbill, C. W. Ashling, P.A. Chater, R. Tovey, C.-B. Schönlieb, Liquid phase blending of metal-organic frameworks, Nat. Commun. 9 (1) (2018) 1–10, https://doi.org/10.1038/s41467-018-04553-6.
[18] L. Frentzel-Beyme, M. Kloß, R. Pallach, S. Salamon, H. Moldenhauer, J. Landers, H. Wende, J. Debus, S. Henke, Porous purple glass – a cobalt imidazolate glass with accessible porosity from a meltable cobalt imidazolate framework, J. Mater. Chem. A 7 (3) (2019) 985–990, https://doi.org/10.1039/c8ta08016j.

[19] A. Qiao, T.D. Bennett, H. Tao, A. Krajnc, G. Mali, C.M. Doherty, A.W. Thornton, J. C. Mauro, G.N. Greaves, Y. Yue, A metal-organic framework with ultrahigh glass-forming ability, Sci. Adv. 4 (3) (2018) eaao6827, https://doi.org/10.1126/sciadv.aao6827.

[20] R. Banerjee, A. Phan, B. Wang, C. Knobler, H. Furukawa, M. O'Keeffe, O.M. Yaghi, High-throughput synthesis of zeolitic imidazolate frameworks and application to $CO_2$ capture, Science 319 (5865) (2008) 939–943, https://doi.org/10.1126/science.1152516.

[21] A. Ulu, Metal–organic frameworks (MOFs): a novel support platform for ASNase immobilization, J. Mater. Sci. 55 (14) (2020) 6130–6144, https://doi.org/10.1007/s10853-020-04452-6.

[22] M. Mubashir, R. Ashena, A. Bokhari, A. Mukhtar, S. Saqib, A. Ali, R. Saidur, K. S. Khoo, H.S. Ng, F. Karimi, Effect of process parameters over carbon-based ZIF-62 nano-rooted membrane for environmental pollutants separation, Chemosphere 291 (2022), 133006, https://doi.org/10.1016/j.chemosphere.2021.133006.

[23] S. Mala, L. Tsybeskov, D. Lockwood, X. Wu, J.-M. Baribeau, Raman scattering in Si/SiGe nanostructures: revealing chemical composition, strain, intermixing, and heat dissipation, J. Appl. Phys. 116 (1) (2014), 014305, https://doi.org/10.1063/1.4886598.

[24] S. Ashraf, R. Mehek, N. Iqbal, T. Noor, G. Ali, A. Wahab, A.A. Qayyum, A. Ahmad, ZIF 67 derived Co–Sn composites with N-doped nanoporous carbon as anode material for Li-ion batteries, Mater. Chem. Phys. 270 (2021), 124824, https://doi.org/10.1016/j.matchemphys.2021.124824.

[25] Y. Liu, X. Que, X. Wu, Q. Yuan, H. Wang, J. Wu, Y. Gui, W. Gan, ZIF-67 derived carbon wrapped discontinuous CoxP nanotube as anode material in high-performance Li-ion battery, Mater. Today Chem. 17 (2020), 100284, https://doi.org/10.1016/j.mtchem.2020.100284.

[26] C. Li, X. Lou, Q. Yang, Y. Zou, B. Hu, Remarkable improvement in the lithium storage property of $Co_2$ $(OH)_2$BDC MOF by covalent stitching to graphene and the redox chemistry boosted by delocalized electron spins, Chem. Eng. J. 326 (2017) 1000–1008, https://doi.org/10.1016/j.cej.2017.06.048.

[27] B. Li, F. Yao, J.J. Bae, J. Chang, M.R. Zamfir, D.T. Le, D.T. Pham, H. Yue, Y.H. Lee, Hollow carbon nanospheres/silicon/alumina core-shell film as an anode for lithium-ion batteries, Sci. Rep. 5 (2015) 7659, https://doi.org/10.1038/srep07659.

[28] W. An, B. Gao, S. Mei, B. Xiang, J. Fu, L. Wang, Q. Zhang, P.K. Chu, K. Huo, Scalable synthesis of ant-nest-like bulk porous silicon for high-performance lithium-ion battery anodes, Nat. Commun. 10 (1) (2019) 1–11, https://doi.org/10.1038/s41467-019-09510-5.

[29] X. Hu, J. Jia, G. Wang, J. Chen, H. Zhan, Z. Wen, Reliable and general route to inverse opal structured nanohybrids of carbon-confined transition metal sulfides quantum dots for high-performance sodium storage, Adv. Energy Mater. 8 (25) (2018), 1801452, https://doi.org/10.1002/aenm.201801452.

[30] Y. Yu, C. Yue, X. Lin, S. Sun, J. Gu, X. He, C. Zhang, W. Lin, D. Lin, X. Liao, ZIF-8 cooperating in TiN/Ti/Si nanorods as efficient anodes in micro-lithium-ion-batteries, ACS Appl. Mater. Interfaces 8 (6) (2016) 3992–3999, https://doi.org/10.1021/acsami.5b11287.

[31] X.L. Wu, Y.G. Guo, J. Su, J.W. Xiong, Y.L. Zhang, L.J. Wan, Carbon-nanotube-decorated nano-LiFePO4@C cathode material with superior high-rate and low-temperature performances for lithium-ion batteries, Adv. Energy Mater. 3 (9) (2013) 1155–1160, https://doi.org/10.1002/aenm.201300159.

[32] G. Khandelwal, N.P.M.J. Raj, S.-J. Kim, ZIF-62: a mixed linker metal–organic framework for triboelectric nanogenerators, J. Mater. Chem. A 8 (34) (2020) 17817–17825, https://doi.org/10.1039/D0TA05067A.

[33] Y. Chen, C. Zou, M. Mastalerz, S. Hu, C. Gasaway, X. Tao, Applications of micro-fourier transform infrared spectroscopy (FTIR) in the geological sciences—a review, Int. J. Mol. Sci. 16 (12) (2015) 30223–30250, https://doi.org/10.3390/ijms161226227.

[34] M. Mubashir, Y.F. Yeong, K.K. Lau, T.L. Chew, J. Norwahyu, Efficient $CO_2/N_2$ and $CO_2/CH_4$ separation using $NH_2$-MIL-53 (Al)/cellulose acetate (CA) mixed matrix membranes, Sep. Purif. Technol. 199 (2018) 140–151, https://doi.org/10.1016/j.seppur.2018.01.038.

[35] D. Tuncel, A. Ökte, Improved adsorption capacity and photoactivity of ZnO-ZIF-8 nanocomposites, Catal. Today 361 (2021) 191–197, https://doi.org/10.1016/j.cattod.2020.04.014.

[36] J. Cheng, D. Ma, S. Li, W. Qu, D. Wang, Preparation of zeolitic imidazolate frameworks and their application as flame retardant and smoke suppression agent for rigid polyurethane foams, Polymers 12 (2) (2020) 347, https://doi.org/10.3390/polym12020347.

[37] C. Hu, Y.-C. Huang, A.-L. Chang, M. Nomura, Amine functionalized ZIF-8 as a visible-light-driven photocatalyst for Cr (VI) reduction, J. Colloid Interface Sci. 553 (2019) 372–381, https://doi.org/10.1016/j.jcis.2019.06.040.

[38] I. Muzammil, Y. Li, M. Lei, Tunable wettability and pH-responsiveness of plasma copolymers of acrylic acid and octafluorocyclobutane, Plasma Process. Polym. 14 (10) (2017), 1700053, https://doi.org/10.1002/ppap.201700053.

[39] X. Chen, X. Wang, D. Fang, A review on C1s XPS-spectra for some kinds of carbon materials, Fuller., Nanotub. Carbon Nanostruct. 28 (12) (2020) 1048–1058, https://doi.org/10.1080/1536383X.2020.1794851.

[40] S. Jurng, Z.L. Brown, J. Kim, B.L. Lucht, Effect of electrolyte on the nanostructure of the solid electrolyte interphase (SEI) and performance of lithium metal anodes, Energy Environ. Sci. 11 (9) (2018) 2600–2608, https://doi.org/10.1039/C8EE00364E.

[41] M. Morita, T. Ohmi, E. Hasegawa, M. Kawakami, M. Ohwadab, Growth of native oxide on a silicon surface, J. Appl. Phys. 68 (3) (1990) 1272–1281, https://doi.org/10.1063/1.347181.

[42] Y. Lin, Q. Zhang, C. Zhao, H. Li, C. Kong, C. Shen, L. Chen, An exceptionally stable functionalized metal–organic framework for lithium storage, Chem. Commun. 51 (4) (2015) 697–699, https://doi.org/10.1039/C4CC07149B.

Supplementary Materials

# Encapsulation of nano-Si into MOF glass to enhance lithium-ion battery anode performances

Jiajia Yan[a,1], Chengwei Gao[b,1], Shibin Qi[c], Zhenjing Jiang[c,d], Lars Rosgaard Jensen[e], Hongbing Zhan[f], Yanfei Zhang[c]*, Yuanzheng Yue[a]*

[a]Department of Chemistry and Bioscience, Aalborg University, DK-9220 Aalborg, Denmark
[b]Laboratory of Infrared Material and Devices, Advanced Technology Research Institute, Ningbo University, Ningbo 315211, China.
[c]School of Materials Science and Engineering, Qilu University of Technology (Shandong Academy of Sciences), Jinan 250353, China.
[d]SEU-FEI Nano-Pico Center, Key Laboratory of MEMS of Ministry of Education, Southeast University, Nanjing, 210096, China.
[e]Department of Materials and Production, Aalborg University, 9220 Aalborg, Denmark
[f]College of Materials Science and Engineering, Fuzhou University, Fuzhou 350108, China
[1] These authors contributed equally to this work
*Corresponding authors. zhang-yanfei@hotmail.com (Y.F. Zhang); yy@bio.aau.dk (Y.Z. Yue).

**This file includes:**

Figs. S1-S6

Tables S1-S3

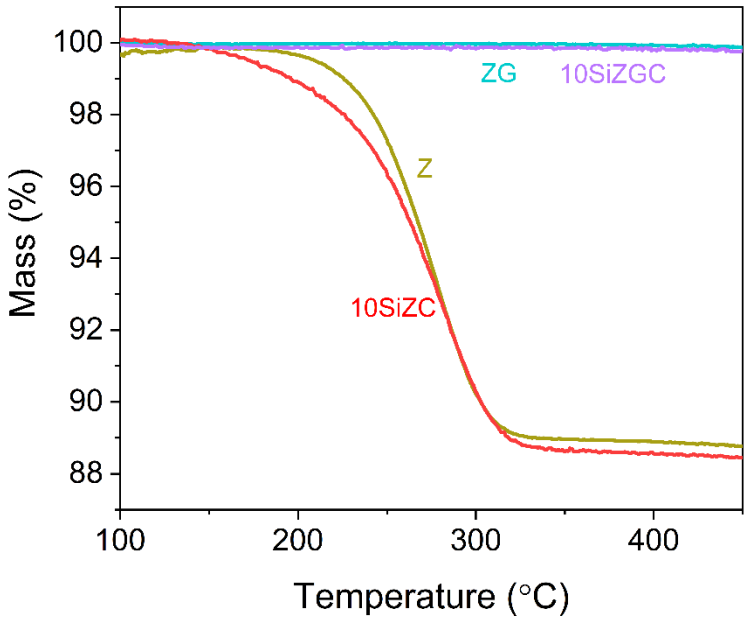


Fig. S1 Thermogravimetric curves of Z, ZG, 10SiZC, and 10SiZGC.

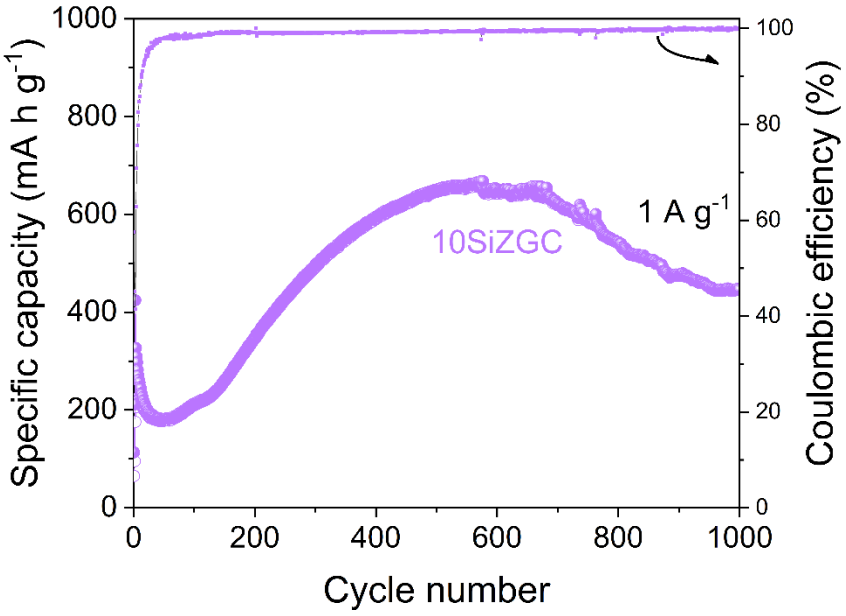


Fig. S2. The cycling performance of anode made from 10SiZGC at 1 A $g^{-1}$ for 1000 cycles.

Table S1 Calculated impedance ($R_e$, $R_s$, $R_{ct}$) of 10SiZC, 10SiZGC before and after 500 cycles based on EIS equivalent circuit model. $R_e$ stands for the resistance of the bulk electrode, electrolyte, and the separator, while $R_s$ and $R_{ct}$ are related to the resistance of SEI resistance and that of charge transfer, respectively.

| Impedance / Samples | $R_e$ (Ω) | $R_s$ (Ω) | $R_{ct}$ (Ω) |
|---|---|---|---|
| 10SiZC | 2.1 | / | 290.4 |
| 10SiZGC | 1.3 | / | 405.3 |
| 10SiZC-after 500 cycles | 2.9 | 14.9 | 29.7 |
| 10SiZGC-after 500 cycles | 2.5 | 17.7 | 10.8 |

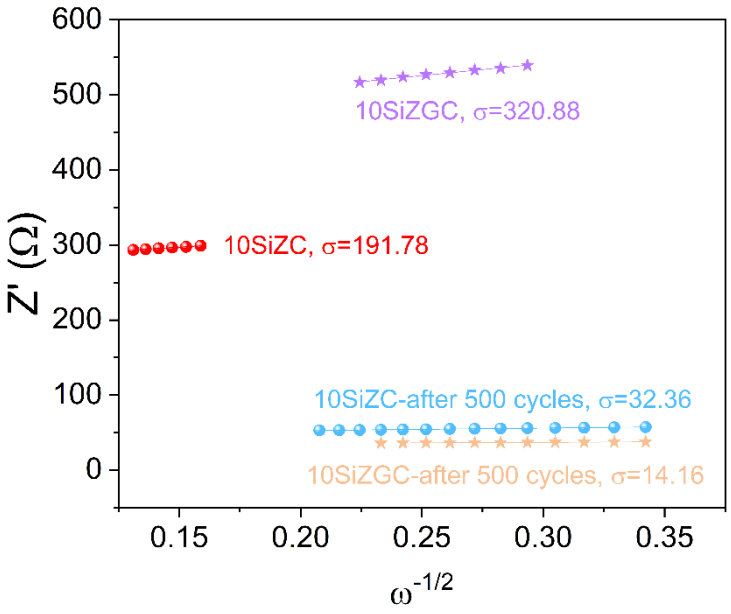


Fig. S3. The dependence of Z' on $\omega^{-1/2}$ in the low frequency region obtained from Nyquist plots in Fig. 3f.

Table S2 The fraction of C=N-C, C-N-H of 10SiZC and 10SiZGC before and after cycling, which were obtained from the deconvoluted N 1s XPS spectra shown in Fig. 4d.

| Bonds / Samples | C=N-C (%) | C-N-H (%) | Ratio (C=N-C/C-N-H) |
|---|---|---|---|
| 10SiZC | 94.3 | 5.7 | 16.5 |
| 10SiZGC | 93.1 | 6.9 | 13.5 |
| 10SiZC-after cycling | 73.8 | 26.2 | 2.8 |
| 10SiZGC-after cycling | 72.9 | 27.1 | 2.7 |

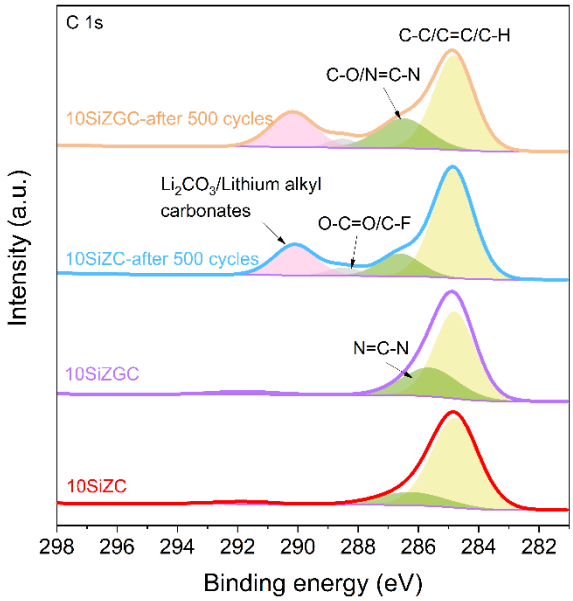


Fig. S4 High-resolution of C 1s XPS spectra for 10SiZC and 10SiZGC before and after cycling.

Table S3 The fraction of Si, $SiO_2$ of 10SiZC and 10SiZGC before and after cycling, which were obtained from the deconvoluted Si2p XPS spectra shown in Fig. 4e.

| Chemical state / Samples | Si (%) | $SiO_2$ (%) | Ratio ($Si/SiO_2$) |
|---|---|---|---|
| 10SiZC | 15.0 | 85.0 | 0.18 |
| 10SiZGC | 13.8 | 86.2 | 0.16 |
| 10SiZC-after cycling | 10.0 | 90.0 | 0.11 |
| 10SiZGC-after cycling | 10.2 | 89.8 | 0.11 |

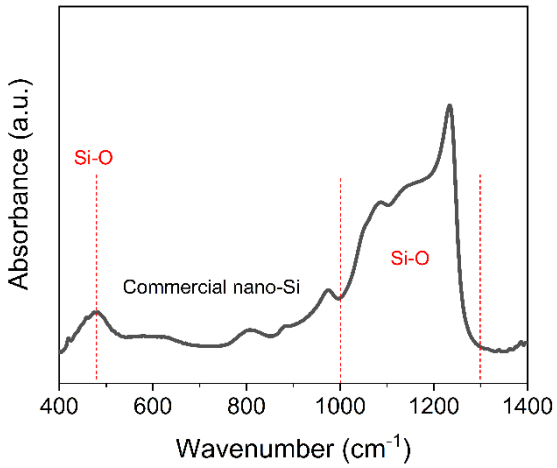


Fig. S5 FTIR spectrum of commercial nano-Si, in which Si-O bonds are already present, indicating the existence of $SiO_2$ in the commercial nano-Si.

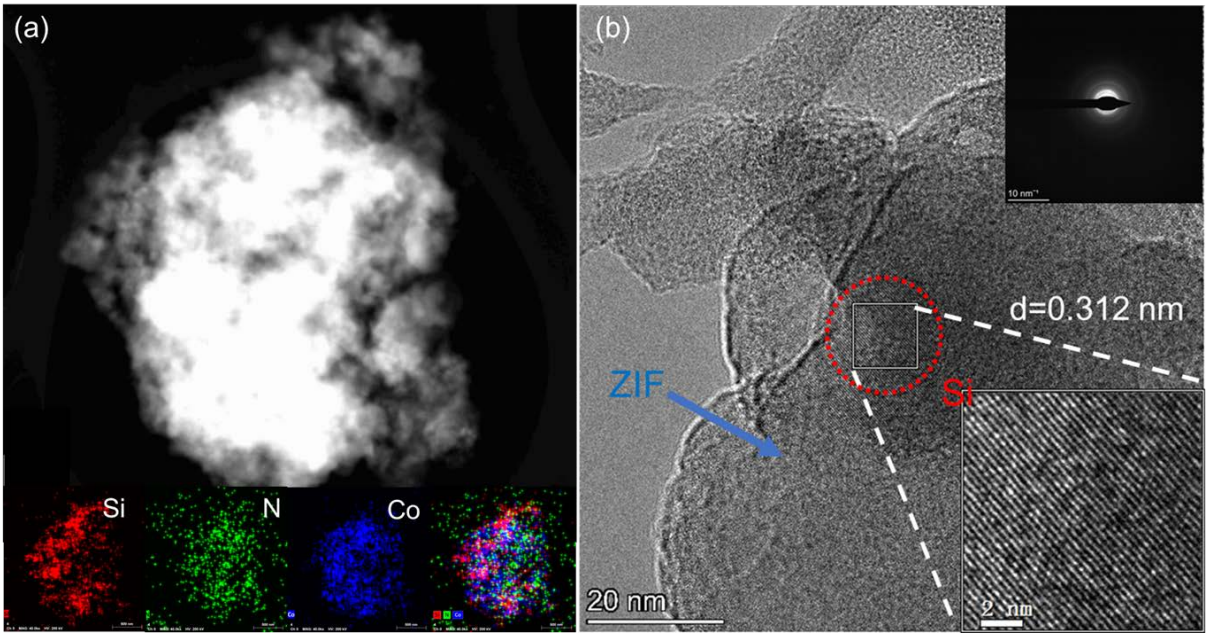


**Fig. S6. Microscopic characterization.** (a) TEM image and EDS mappings of Si, N, Co for 10SiZC after cycling. (b) HRTEM image and the corresponding SAED patterns of 10SiZC after cycling.

# Paper III

# Optimizing Si/vanadium-tellurite glass composites as superior anodes for Li-ion batteries by hot pressing

Jiajia Yan[a], Xiangyu Li[b], Nian Shi[c], Xianglong Ren[d], Hemin Zhou[d], Haizheng Tao[d], Jinjun Ren[c], Ang Qiao[d], Yanfei Zhang[b]*, Yuanzheng Yue[a]*

[a]Department of Chemistry and Bioscience, Aalborg University, 9220 Aalborg, Denmark
[b]School of Materials Science and Engineering, Qilu University of Technology (Shandong Academy of Sciences), Jinan 250353, China.
[c]Key Laboratory of Materials for High Power Laser, Shanghai Institute of Optics and Fine Mechanics, Chinese Academy of Sciences, Shanghai 201800, China.
[d]State Key Laboratory of Silicate Materials for Architectures, Wuhan University of Technology, Wuhan 430070, China

*Corresponding authors. zhang-yanfei@hotmail.com (Y.F. Zhang); yy@bio.aau.dk (Y.Z. Yue).

## Abstract

Vanadium-tellurite glasses (VT) have emerged as promising anode materials for lithium-ion batteries (LIBs) due to their unique disordered open network for $Li^+$ diffusion and high cycling stability. However, the capacity of VT still needs to be greatly improved. To tackle this problem, combining VT with high active elements is a bright way. Silicon (Si), which exhibits ultrahigh theoretical capacity (>4000 mA h $g^{-1}$) but suffers from rapid capacity decline due to vast volume changes upon lithiation/delithiation. This inspired us to combine VT with Si to take advantage of both materials. Here, we embedded Si nanoparticles into VT glass matrix and obtained Si/VT composite (VTS) by hot pressing method. The obtained VTS yields a synergistic effect, exhibitng a capacity of 408 mA h $g^{-1}$ at 1 A $g^{-1}$ after 1000 cycles, which is more than three times that of VT and fourteen times that of pure Si. The origin of this huge enhancement is revealed by performing structural analyses. The VT matrix with open network not only can contribute to lithium storage, but also buffer the volume changes and prevent the aggregation of Si nano particles during lithiation/delithiation processes.

**Keywords**: Vanadium-tellurite glass; Silicon; Anode; Lithium-ion batteries

## 1. Introduction

With high energy density, long lifespan, and environmental friendliness, lithium-ion batteries (LIBs) represent one of the most attractive portable energy storage devices. However, the current LIBs cannot satisfy the demands for safer and higher energy density batteries used in electric vehicles and large-scale energy storages [1]. To tackle these problems, many efforts have been made. From the aspect of safety, all-solid-state batteries have been widely studied, that is, replacing conventional organic liquid electrolytes with solid electrolytes, of which inorganic glass-ceramic/glass-based solid electrolytes are one of the most promising candidates as they show the highest ionic conductivities with $10^{-2}$~$10^{-3}$ S $cm^{-1}$[2-5]. In terms of high energy density (proportional to specific capacity), one of the main attempts is to use silicon (Si), which has a theoretical capacity exceeding 4000 mA h $g^{-1}$, to replace current graphite anodes [1, 6]. Nonetheless, the drastic volume fluctuation of Si (~400%) during lithiation/de-lithiation [1] leads to a dramatic decay of specific capacity, i.e., capacity retention is about 50 mA h $g^{-1}$ within 100 cycles [7, 8]. To buffer the volume expansion of Si, some specific structures, such as hollow core-shell, york-shell, porous structures, in combination with carbon have been constructed mostly by sol-gel method, solvothermal method, chemical vapor deposition method et.al. [9-12]. However, the complex synthesis processes, low yield and high cost [2] hinder their practical applications.

Vanadium-tellurite glasses (VT), which exhibit a superior cycling stability, i.e., almost no capacity fading for 5000 cycles [13, 14], have emerged as promising anode material for LIBs. The reason for the high cycling stability of VT glasses lies in their unique structure feature, i.e., not purely 3D tetrahedral network, that exhibits higher liquid fragility and stronger crystallization tendency upon heating compared to most the conventional oxide glasses with the tetrahedral network. During discharging/charging process, electrochemically active γ-$Li_3VO_4$ nanocrystals are formed in VT glass. The in-situ growth of nanocrystals from glass not only toughening the glass matrix, and thereby

increasing the cycling stability, but also providing more space/channels between the crystals and glass matrix to facilitate the transportation of $Li^+$ [13-16]. However, the capacities of VT glasses are around 120 mA h $g^{-1}$ at a current density of 1 A $g^{-1}$ [13, 14] and still need to be improved. Thus, combing Si with VT glass could be a promising strategy to achieve the synergetic effect, i.e., to both enhanced capacity and increased cycling stability of the anode for LIBs.

In our previous study [15], we have investigated how Si-doping affects the structure and crystallization behavior of VT glasses during heating process. Based on these results, in this work, we focused on how Si and VT glass can be properly combined by comparing traditional heating process and hot-pressing process and studied the electrochemical performance of the composites. The reason we chose heat-treatment to conduct the combination of Si and glass is that glass exhibits viscous flow above $T_g$ and thus can act as 'binder' for bonding Si. It is found that the Si@VT composite after hot pressing exhibited a reversible specific capacity of 408 mA h $g^{-1}$, which is more than three times that of VT and fourteen times that of pure Si at the current density of 1 A $g^{-1}$ after 1000 cycles, resulting from the synergy effects between Si and VT glass. Furthermore, considering that the best lithium solid-state electrolytes are inorganic glass/glass-ceramics, the interfacial stability between the glassy solid-state electrolyte and the traditional electrode faces a big challenge due to the mismatch of expansion coefficient and poor compatibility at the interface [4]. Thus, it can be anticipated that glassy electrolyte and glassy electrode could provide good expansion coefficient matching and interfacial compatibility and thus a minimal interfacial polarization of the cell [6]. In addition, glass materials pose many other advantages, i.e., tunable composition, simple preparation process, low cost, etc. All of these suggest that the composites incorporating high-capacity elements into glasses are promising anode materials for the next generation of high-performance LIB (all-solid-state LIB). This work not only proved that combining Si with VT glass through hot pressing is an

effective strategy to obtain high-performance anode materials for LIBs, but also paves a new path for preparation glass-based functional materials.

## 2. Experimental section

### 2.1 sample preparation

The $50V_2O_5$-$50TeO_2$ (in mol %) glass (VT) was prepared via the melt-quenching method [13, 14], followed by crushing and sieving to obtain glass power with a size distribution between 10 and 20 μm. 100-mg, 200-mg, 300-mg, 400-mg commercial nano-silicon powder (about 20-60 nm particle size) were separately added into 0.9, 0.8, 0.7, 0.6g glass powder, and then mixed thoroughly, which are referred to as 10VTS, 20VTS, 30VTS, 40VTS, according to the fraction of Si by weight, respectively. To find out a proper hot pressing process, we firstly fixed the fraction of Si and hot pressed 10VTS samples in a vacuum furnace under 100 MPa and kept for 0.5 h at different temperatures. The temperatures selected were based on the differential scanning calorimeter (DSC) result of 10VTS (Fig. S1), which shows characteristic temperatures, i.e., glass transition temperature ($T_g$=509 K), onset crystallization temperatures ($T_{c1}$=563 K, $T_{c2}$=602 K), melting temperature ($T_m$=755 K). Specifically, 10VTS samples were hot-pressed at 550 K (above $T_g$), 570 K (above $T_{c1}$), 620 K (above $T_{c2}$), 670 K (below $T_m$), and 770 K (above $T_m$), respectively. These samples are referred to as 10VTS-550-HP, 10VTS-570-HP, 10VTS-620-HP, 10VTS-670-HP, and 10VTS-770-HP, respectively, according to the hot pressing temperature. For comparison, 10VTS was heated to 620 K and kept for 0.5 h in the vacuum furnace without pressure (traditional heating process), and the obtained sample is named as 10VTS-620. In addition, to find the optimal fraction of Si, 20VTS-620-HP, 30VTS-620-HP, 40VTS-620-HP samples were also obtained.

### 2.2 Materials characterizations

The crystal phases of samples after heat-treatment were identified on a PANalytical X-ray diffractometer with Cu Kα (λ = 1.5406 Å) radiation during the 2θ range of 5~70° with a step size of 0.013°. The thermal events of samples, such as the glass transition temperature ($T_g$) and the crystallization onset temperature et. al, were detected by the differential scanning calorimeter (DSC) (Jupiter 449C, Netzsch) in argon to 500°C at 10 K/min. Fourier transform infrared (FTIR) spectra were conducted on a Bruker TENSOR II FTIR spectrometer with Platinum ATR Accessory at room temperature in the range of 400-4000 $cm^{-1}$. To study the chemical environment of V, Si, X-ray photoelectron spectroscopy (XPS) was performed by using ESCALAB 250Xi spectrometer (ThermoFisher Scientific, USA) with nonmonochromatic Al Ka X-ray (1486.6 eV) at pass energy of 50 eV. The morphologies and distribution of Si in samples were analyzed using field-emission scanning electron microscopy (FE-SEM) (Supra-55, Zeiss Inc.), and X-ray energy dispersive spectroscopy (EDS) (X-Max, OXFORD Instruments Inc.).

2.3 Cell assembly and Electrochemical Characterizations

The electrochemical performance of VTS after heat-treatment were evaluated by using CR2032 coin cells with lithium foil as the reference electrode. The as-prepared VTS (70 wt%), acetylene black (20 wt%), and polyvinylidene difluorides (PVDF, 10 wt%) were mixed evenly in N-methyl-2-pyrrolidone (NMP) and then pasted onto a copper foil substrate and dried at 110 °C in a vacuum oven for 12 h to get working electrodes. 1 M $LiPF_6$ in ethylene carbonate (EC)/diethyl carbonate (DEC)/dimethyl carbonate (DMC) (1:1:1 vol%) was used as the electrolyte and the Celgard 2325 membrane (diameter of 19.0 mm) was used as the separator. Cells were assembled in an argon-filled glovebox with both the moisture and the oxygen content below 0.1 ppm and then tested at 25 °C. The galvanostatic charging/discharging tests of the samples were conducted on a Land battery test system (CT2001A) with the voltage range 0.01-3V. Cyclic voltammetry (CV) curves were obtained in the voltage range of 0.01–3 V at the scanning rate of 0.1 mV $s^{-1}$. EIS spectra were recorded in the frequency range of

0.1 Hz–100 kHz on CHI 760e electrochemical workstation. All electrochemical measurements were repeated with different batches of samples to confirm the reproducibility of their performances.

### 3. Results and Discussions

Fig. 1a shows the XRD patterns of the as-prepared hot-pressing samples. Clearly, sharp diffraction peaks at 2θ≈28, 47, 56° corresponding to Si are detected in all the samples, indicating that Si is preserved after heat-treatment. In addition, $V_2O_5$ and $TeVO_4$ crystals appeared in 10VTS-670-HP and 10VTS-770-HP but were not detected in 10VTS-550-HP, 10VTS-570-HP and 10VTS-620-HP samples. The reason why samples 10VTS-570-HP and 10VTS-620-HP heated above $T_{c1}$ (563K) did not show other crystals besides Si could be due to the different heating conditions between the different devices (DSC and furnace).

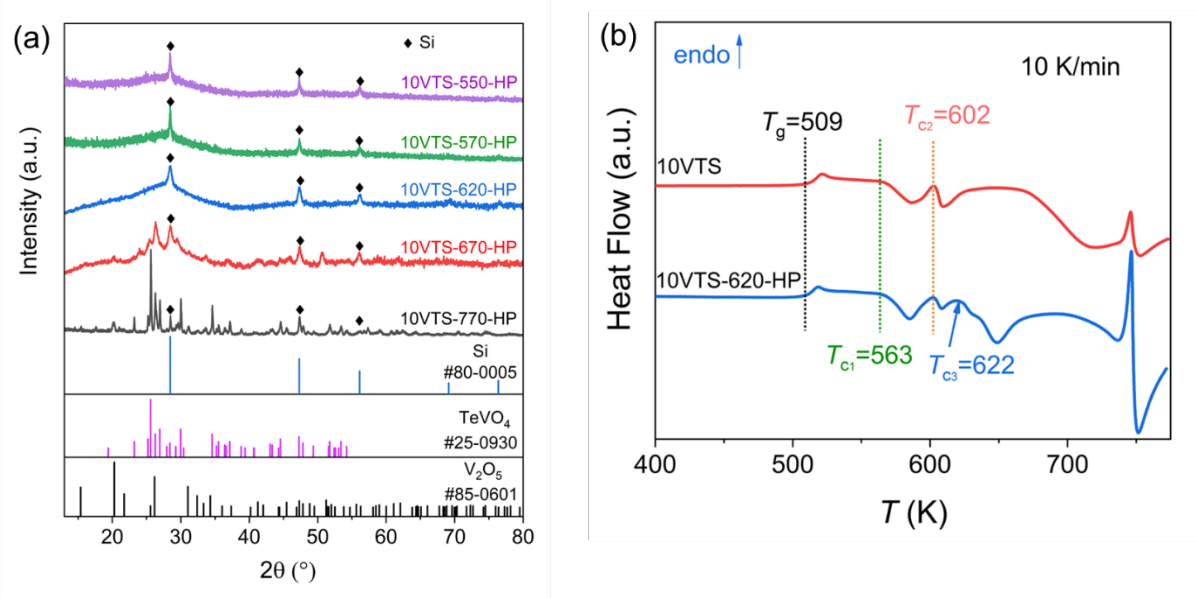


**Fig. 1 Phase and thermodynamic analyses.** (a) XRD patterns of 10VTS-550-HP, 10VTS-570-HP, 10VTS-620-HP, 10VTS-670-HP, and 10VTS-770-HP. (b) DSC upscan curves of both 10VTS (the red line) and 10VTS-620-HP (the blue line), which are obtained at 10 K/min in argon. The characteristic temperatures such as glass transition ($T_g$) and crystallization onset temperatures ($T_{c1}$, $T_{c2}$, and $T_{c3}$) are denoted in the curves.

To study whether the hot-pressing sintering process leads to the viration of thermal properties, DSC measurements of 10VTS and 10VTS-620-HP were conducted. As shown in Fig. 1b, the $T_g$, $T_{c1}$, $T_{c2}$

of both samples are the same, while a new crystallization peak appears in 10VTS-620-HP ($T_{c3}$=622 K). This is understandable when considering that that during heating process, the thermal energy can be used to increase the potential energy of VTS and overcome energy barrier of a redox reaction which may occur between Si and VT [15]. Therefore, 10VTS-620-HP is more likely to precipitate new crystals in the subsequent DSC scan compared to 10VTS.

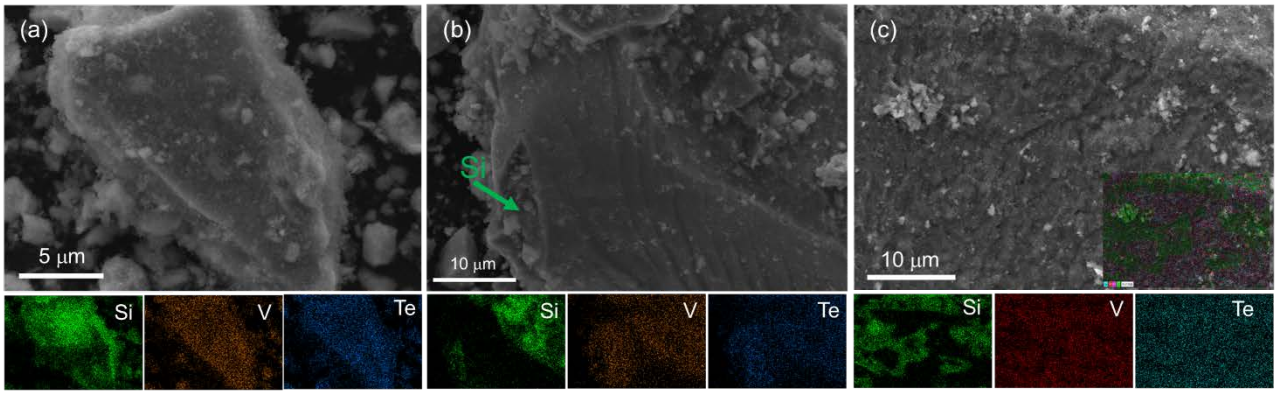


**Fig. 2 Morphological Characterization**. SEM images and EDS elemental mappings of Si, N and Te. (a) 10VTS-620, (b) 10VTS-620-HP, (c) 10VTS-670-HP.

The morphologies and microstructures of 10VTS-620, 10VTS-620-HP, and 10VTS-670-HP were measured using SEM, as shown in Fig. 2. For 10VTS-620 (Fig. 2a), VT with a particle size of 10~20 μm was observed. Clearly, Si nano particles agglomerated and covered the surface of VT, suggesting that Si is only physically contact with VT when no pressure is applied. For 10VTS-620-HP (Fig. 2b) and 10VTS-670-HP (Fig. 2c) samples, numerous Si nano particles are embedded into VT matrix and formed Si/VT composites. The composites fabricated by hot pressing may lead to a synergistic effect and enhance the electrochemical performances of composite-based anodes because VT matrices are expected to buffer the volume change of Si.

To investigate the structural evolution upon heat-treatment, FTIR and XPS measurements were performed. Fig. 3a show the FTIR spectra of Si, 10VTS, 10VTS-620, 10VTS-620-HP. Peaks at around 478 $cm^{-1}$ and 1000~1250 $cm^{-1}$ correspond to Si-O vibrations [17, 18], which are clearly shown

in sample Si suggesting that Si-O already exists in commercial Si particles. Peaks at 680 $cm^{-1}$ are ascribed to Te–O–Te or O–Te–O [19], while peaks at around 982$cm^{-1}$ are attributed to [$VO_5$] [15, 19]. In addition, the broad peaks locating between 750 and 940 $cm^{-1}$ are mainly due to V–O–V, [$VO_4$], and [$VO_5$] vibrations. Clearly, the intensity of the peak at 1000~1250 $cm^{-1}$ increases for both 10VTS-620 and 10VTS-620-HP compared to that of the pristine 10VTS, implying the oxidation of Si upon heat-treatment. Considering that the heating process is carried out in a vacuum, it can only be explained that VT oxidized Si. Moreover, a sharp peak at 530 $cm^{-1}$ corresponding to V–O–V vibrations [15] was observed in 10VTS-620 but not in 10VTS-620-HP. Instead, sharp peaks at 644 $cm^{-1}$ and 435 $cm^{-1}$ arising from V–O–V/Te–O–Te vibrations were detected in 10VTS-620-HP [20, 21]. The spectral differences between 10VTS-620 and 10VTS-620-HP suggest that the pressure applied affects the structural evolution of VTS during heating.

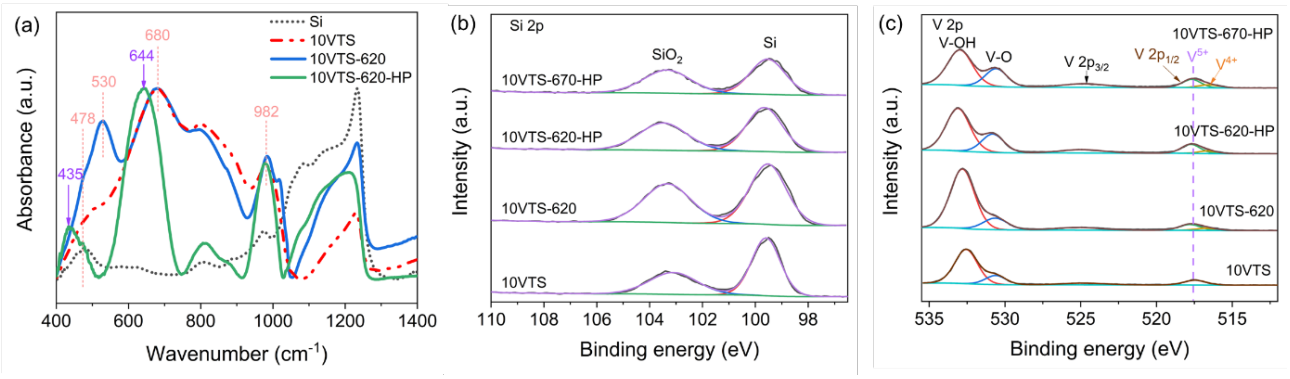


**Fig. 3 Structure Characterizations.** (a) FTIR spectra of Si, 10VTS, 10VTS-620, and 10VTS-620-HP, where the number, i.e., 10, represents the introduction of 10 wt% Si nanoparticles into VT. XPS high-resolution of Si 2p(b) and V 2p (c) spectra for 10VTS, 10VTS-620, 10VTS-620-HP, and 10VTS-670-HP.

Fig. 3a shows the XPS high-resolution of Si 2p spectra for 10VTS, 10VTS-620, 10VTS-620-HP, and 10VTS-670-HP samples. Each spectrum can be deconvoluted into peaks at ~99.5 eV and ~103.1 eV, which are assigned to Si and $SiO_2$, respectively [22]. The deconvolution results are shown in table 1. Clearly, the fraction of Si that converts into $SiO_2$ increases as the heating temperature rises. In addition, the same fractions of Si in VTS-620 and VTS-620-HP (~54.5%) indicate that the pressure does not

promote the Si-to-$SiO_2$ conversion. The high-resolution spectra of V 2p for these samples are shown in Fig. 3c. the V $2p_{1/2}$ and V $2p_{3/2}$ peaks are located at 517.5 and 524.9 eV. Peaks at 532.7 and 530.6 are ascribed to V-OH, and V-O, respectively. [23, 24]. For 10VTS subjected to heat-treatment, i.e., samples 10VTS-620, 10VTS-620-HP, and 10VTS-670-HP, as the V $2p_{1/2}$ peak becomes wider compared with that of pristine 10VTS, it can be deconvoluted into two peaks, i.e., ~517.5 and 516.4 eV arising from $V^{5+}$ and $V^{4+}$, respectively [23, 24]. These results suggest a redox reaction occurred in 10VTS during heating process. Moreover, the formation of $V^{4+}$ could facilitate the electrical conductivity in VT glass. This is because that during discharging/charging process, electrons can cause formation of polarons, and thus, high electronic conductivity can be realized by polaron-hopping in $V^{4+}$–O–$V^{5+}$ chains ($V^{4+}$–O–$V^{5+}$→$V^{5+}$–O–$V^{4+}$) [15]. However, another product of redox reaction between Si and VT, i.e., $SiO_2$, can decrease the electrical conductivity of materials as it is an insulating material. Therefore, there should be a compromise ratio between $V^{4+}$ and $SiO_2$ to achieve high electrical conductivity.

Table 1 The fraction of Si, $SiO_2$ of VTS, VTS-620, VTS-620-HP, VTS-670-HP, which were obtained from the deconvoluted Si 2p XPS spectra shown in Fig. 3b.

| Chemical state / Samples | Si (%) | $SiO_2$ (%) | Ratio ($Si/SiO_2$) |
|---|---|---|---|
| VTS | 61.1 | 38.9 | 1.6 |
| VTS-620 | 54.5 | 45.5 | 1.2 |
| VTS-620-HP | 54.6 | 45.4 | 1.2 |
| VTS-670-HP | 52.2 | 47.8 | 1.1 |

To explore whether the combination of Si and VT glass by traditional heat-treatment or hot-pressing sintering poses a synergistic effect, the cycling performances of Si, VT, 10VTS-570-HP, 10VTS-620-HP, 10VTS-670-HP, 10VTS-770-HP, and10VTS-620 based anodes were measured (Fig. 4a). The capacities of Si, VT, 10VTS-570-HP, 10VTS-620, 10VTS-770-HP are 28, 110, 136, 206, 205 mA h $g^{-1}$ at a current density of 1 A $g^{-1}$ up to 1000 cycles, respectively, while those of 10VTS-620-HP

and 10VTS-670-HP reaches 408 and 313 mA h $g^{-1}$, respectively. The significant capacity enhancement of the latter two samples verifies that the hot pressing is an effective method to combine Si and VT, and hence, realizing a synergistic effect. As 10VTS-620-HP shows the highest capacity among the above-mentioned samples, we increased the fraction of doping Si in VT, i.e., 20%, 30%, 40%, and hot pressed the mixture with the same process as that of 10VTS-620-HP. The as-prepared samples are referred to as 20VTS-620-HP, 30VTS-620-HP, 40VTS-620-HP, respectively. Fig. 4b shows the cycling performances of these samples. Clearly, the capacity of the three samples is 216, 260, and 126 mA h $g^{-1}$ at 1 A $g^{-1}$ after 1000 cycles, respectively, which is much lower than that of 10VTS-620-HP. The increased Si fractions in VT leads to lower capacities compared to 10VTS-620-HP, indicating that 10% Si is the optimal doping level in our study.

The rate performances of the above-mentioned samples at the current densities of 0.1, 0.2, 0.5, 1, and 2 A $g^{-1}$ are shown in Figs. 4c, d. In Fig. 4c, the average specific capacity of samples 10VTS-620-HP and 10VTS-670-HP are 725 and 621 mA h $g^{-1}$ after 5 cycles at 0.1 A $g^{-1}$, respectively, which are the top two among the samples. The capacity of Si drops dramatically from 2290 to 774 mA h $g^{-1}$ after the first 5 cycles. The capacities of 10VTS-570-HP, 10VTS-620, and 10VTS-770-HP decrease from ~450 to ~200 mA h $g^{-1}$ after 5 cycles at 0.1 A $g^{-1}$. With the increase in the current density, the average capacities of all samples decrease, among which 10VTS-620-HP exhibits the highest capacity retention after cycles at 0.2, 0.5, 1, and 2 A $g^{-1}$. When the current density was set back to 0.1 A $g^{-1}$, the capacities of 10VTS-620-HP and 10VTS-670-HP recover to 710 and 532 mA h $g^{-1}$, respectively, and remain stable in the following cycles, indicating a superior rate performance. In contrast, the capacity of Si reaches 568 mA h $g^{-1}$ when the current density was switched back to 0.1 A $g^{-1}$, but decreases rapidly to 67 mA h $g^{-1}$ after 100 cycles. This significant capacity decrease of Si is due to its volume expansion and pulverization [25].

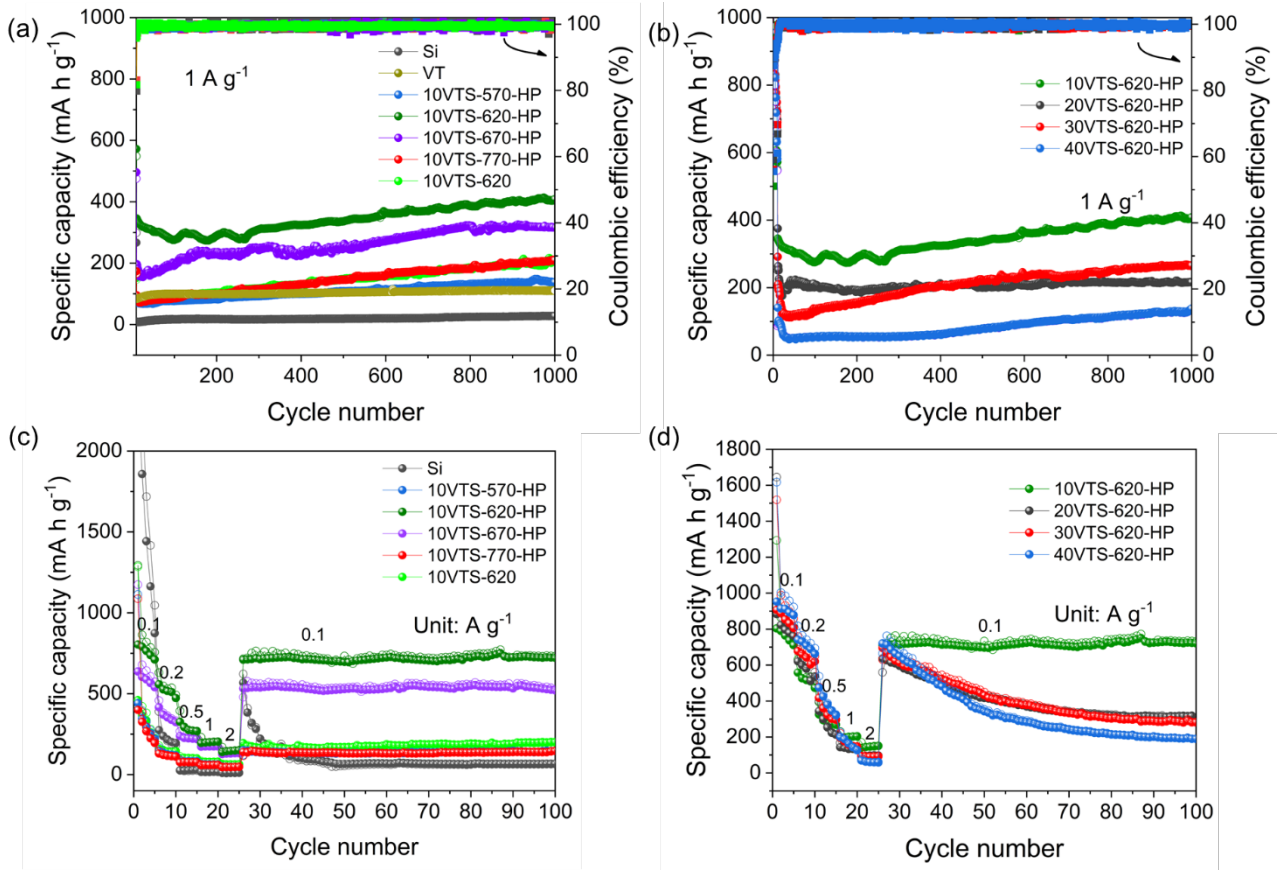


**Fig. 4 Cycling and rate performances**. (a), (b) Cycling performances of anodes based on Si, VT, 10VTS-570-HP, 10VTS-620-HP, 10VTS-670-HP, 10VTS-770-HP, 10VTS-620, 20VTS-620-HP, 30VTS-620-HP, and 40VTS-620-HP at 1 A $g^{-1}$ after 1000 cycles; (c), (d) The rate performances of anodes based on Si, 10VTS-570-HP, 10VTS-620, 10VTS-620-HP, 10VTS-670-HP, 10VTS-770-VTS, 20VTS-620-HP, 30VTS-620-HP, and 40VTS-620-HP at current densities of 0.1, 0.2, 0.5, 1, 2 and 0.1 A $g^{-1}$.

Fig. 4d exhibits the rate performances of 10VTS-620-HP, 20VTS-620-HP, 30VTS-620-HP, and 40VTS-620-HP. In the first 5 cycles, the average capacity of the latter three samples is 808, 857, and 910 mA h $g^{-1}$, respectively, which is higher than that of 10VTS-620-HP (725 mA h $g^{-1}$). However, those three samples are sensitive to the current density and a show rapid decline with the increase of the current density. When the current was back to 0.1 A $g^{-1}$, the capacity of the three samples is 636, 695, and 720 mA h $g^{-1}$, respectively, and decrease fast to 316, 281, and 189 mA h $g^{-1}$ after 100 cycles. This could be interpreted that although the fraction of doping Si in 20VTS-620-HP, 30-VTS-620HP, 40-VTS-620-HP is higher than that in 10-VTS-620-HP, not all the Si nanoparticles can be embedded into the VT glass matrices due to their limited ability to accommodate Si. A higher fraction of doping

Si can lead to more amount of bare Si aggregating on the surface of VT particles rather than embedding into glass protection matrices, resulting in an increase of volume expansion and pulverization of Si and hence rapid capacity decline.

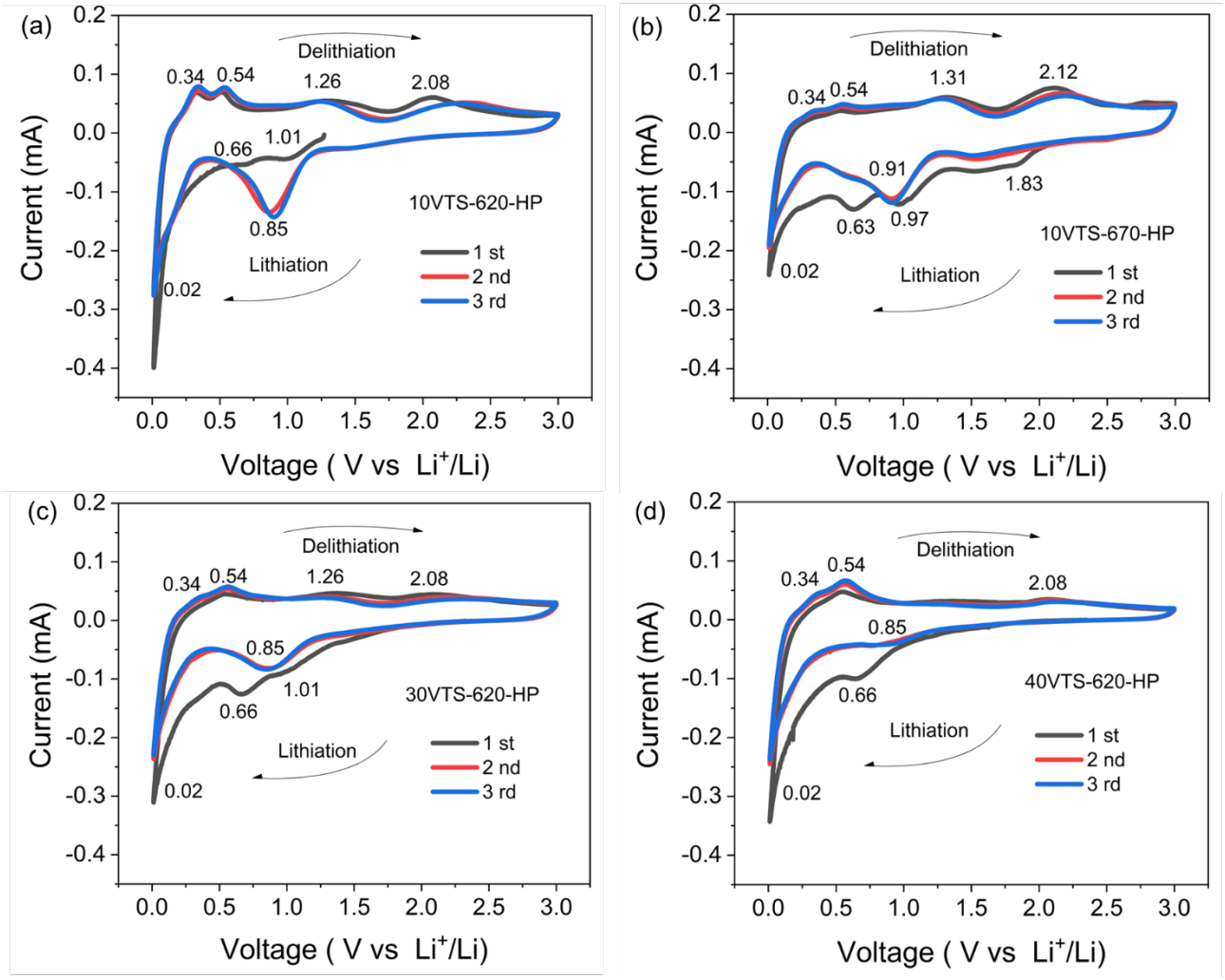


**Fig. 5 Cyclic Voltammetry (CV) curves**. (a) 10VTS-620-HP, (b) 10VTS-670-HP, (c) 30VTS-620-HP, (d) 40VTS-620-HP. The curves are obtained in the voltage range from 0.01 to 3.0 V at a scan rate of 0.1 mV $s^{-1}$.

The cyclic voltammetry (CV) measurements of 10VTS-620-HP, 10VTS-670-HP, 30VTS-620-HP, and 40VTS-620-HP were carried out to study why the 10VTS-620-HP based anode shows higher capacity than other as-prepared samples and investigate the electrochemical reaction involved, as shown in Fig. 5. In the first lithiation process of 10VTS-620-HP (Fig. 5a), the reduction peaks at around 1.01 V, 0.66 V, and 0.02 V attribute to the interaction between $Li^+$ and VT, formation of solid

electrolyte interface film (SEI), and the insertion of $Li^+$ into Si, forming $Li_xSi$ phase, respectively [13, 26]. The anodic peaks at around 0.34 V and 0.54 V are ascribed to the extraction of $Li^+$ from $Li_xSi$, while the peaks at ~1.26 and ~2.08 come from the extraction of $Li^+$ from VT glass matrix [13, 14]. In the subsequent two CV cycles, peaks at 1.01 and 0.66 V disappear and instead, a new strong peak located at ~0.85 V arising from the insertion of $Li^+$ into VT appears.

Fig. 5b shows the CV curves of 10VTS-670-HP. This sample contains both glass and V/V-Te crystals ($V_2O_5$, and $TeVO_4$), namely glass-ceramic. In the first cathodic scan, we observed peaks at 1.83 V and 0.97 V corresponding to the insertion of $Li^+$ into VT glass-ceramic and 0.63 and 0.02 V, which arise from the formation of SEI and the insertion of $Li^+$ into Si, respectively. The anodic peaks are at 1.31 and 2.21 V, attributing to the $Li^+$ extraction from VT glass-ceramic [13, 14]. In the second and third CV curves, new strong peaks at ~0.91 V appear in the cathodic scan due to the $Li^+$ insertion into VT glass-ceramic. In addition, peaks at 0.02, 0.34, and 0.54 V in 10VTS-670-HP are weaker than those in 10VTS-620-HP, indicating that the reversible reaction between Si and $Li_xSi$ is reduced. This phenomenon could be explained that as the hot pressing temperature increases, more Si in VTS is converted into $SiO_2$ verified by the FTIR and XPS results (Fig. 3), leading to fewer Si active sites and hence fewer reversible reaction.

The CV curves of 30VTS-620-HP (Fig. 5c) show the same cathodic and anodic peak positions as those of 10VTS-620-HP (Fig. 5a), but peak intensities of the former sample are weaker. This suggests fewer $Li^+$ insertion/extraction into/from both $Si/Li_xSi$ and VT matrix in 30VTS-620-HP. In Fig. 5d, 40VTS-620-HP shows no anodic peak at 1.26 eV, and weaker peaks at 0.02, 0.34, and 0.54 eV compared with those in 10VTS-620-HP. In addition, peaks at 0.85 and 2.08 eV are almost invisible in 40VTS-620-HP, indicating nearly no $Li^+$ insertion/extraction into/from VT matrix. These results imply that as the fraction of doping Si increases, the reversible reactions decrease, results in the

decrease in capacity. This is reasonable considering the limited ability of VT matrix to accommodate Si. When the amount of doping Si particles exceeds the accommodating limit of VT, the excess Si cannot be embedded into VT matrix by the hot pressing. Instead, bare Si particles aggregated and covered the surface of VT particles, causing the inability of $Li^+$ to go into VT matrix. Moreover, the bare Si without protection of VT matrix is easily pulverized due to volume expansion during charge/discharge, resulting in a rapid decrease in capacity.

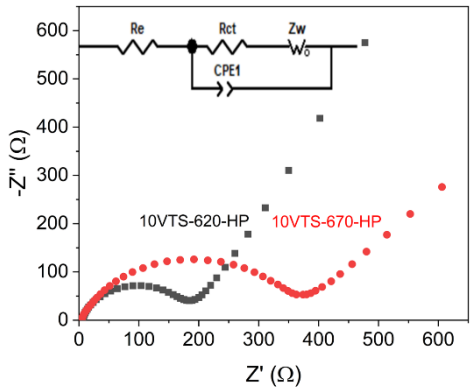


Fig. 6 Nyquist plots of 10VTS-620-HP and 10VTS-670-HP obtained from electrochemical impedance spectra within frequency range from 0.01 Hz to 100 kHz.

Fig. 6 shows the electrochemical impedance spectroscopy (EIS) of 10VTS-620-HP and 10VTS-670-HP. Each EIS curve contains one semicircle at high frequency and an inclined line at the low frequency region. The resistance parameters (table 4-2) were obtained from the inset equivalent circuit, where $R_e$, $R_{ct}$, $C_{PE1}$ and $Z_w$ represent the ohmic resistance, charge transfer resistance, interface capacitance and diffusion impedance of the half-cell systems, respectively [27, 28]. The charge transfer resistance ($R_{ct}$) of 10VTS-620-HP (161.6 Ω) is much smaller than that of 10VTS-670-HP (354.8 Ω), indicating that the former exhibits a higher electrical conductivity, which can lead to a better electrochemical performance in 10VTS-620-HP.

Table 4-2 Calculated impedance ($R_e$, $R_{ct}$) of 10VTS-620-HP and 10VTS-670-HP based on EIS equivalent circuit model.

| Impedance / Samples | $R_e$ (Ω) | $R_{ct}$ (Ω) |
|---|---|---|
| 10VTS-620-HP | 4.4 | 161.6 |
| 10VTS-670-HP | 3.4 | 354.8 |

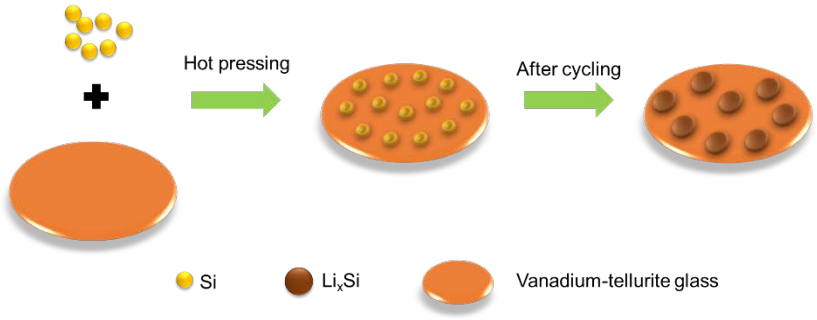


Fig. 7 The protecting role of VT glass matrix which prolongs the cycling life of Si.

As shown in Fig. 6, the possible mechanism of the electrochemical performance enhancements of VTS after hot pressing is related to VT matrix that protect Si from pulverization during charging and discharging process. First, VT glass exhibits an open disordered network structure, beneficial for $Li^+$ diffusion. Second, the Si was embedded into VT matrix by hot pressing and VT constrains the volume expansion and buffers pulverization of Si to some extend during the insertion of $Li^+$ into the composite, thereby realizing good cycling performances. Third, the formation of $V^{4+}$ arising from redox reaction between Si and VT increases the electrical conductivity of VT. Therefore, the VTS-HP samples yield a synergistic effect and exhibit better reversible capacity and rate capability than pristine Si and VT.

## 4. Conclusions

In this work, we embedded Si nanoparticles into vanadium-tellurite glass (VT) matrix by hot pressing method to obtain Si/VT composite (VTS) for lithium storage. By optimizing the hot-pressing temperature and Si fraction, the VTS can yield a strong synergistic effect. Specifically, 10VTS-620-HP based anode exhibits a capacity of 408 mA h $g^{-1}$ at 1 A $g^{-1}$ after 1000 cycles, which is more than

three times that of VT and fourteen times that of pure Si. The significant performance enhancement could be due to that VT glass matrix with open disordered network not only can provide channels for lithium transfer but also accommodate Si and buffer its volume change, and hence make full use of both VT glass and Si for lithium storage. In addition, during heat-treatment, the formation of $V^{4+}$ arising from redox reaction between Si and VT, facilitates the electron transfer in 10VTS-620-HP. Our strategy to construct Si/VT-glass composite could be further extended to other types of oxide glasses to combine with highly active materials like $SnO_2$ and Sn for application in electrochemical energy storage.

**Acknowledgments**

Authors would like to acknowledge support by China Scholarship Council (201906650022). Y.F.Z. would like to acknowledge support by Taishan Youth Scholar Project of Shandong Province (tsqn202103098) and the Shandong Provincial Natural Science Foundation (ZR2020ME025).

**References**

[1] Z.H. Liu, Q. Yu, Y.L. Zhao, R.H. He, M. Xu, S.H. Feng, S.D. Li, L. Zhou, L.Q. Mai, Silicon oxides: a promising family of anode materials for lithium-ion batteries, Chem. Soc. Rev. 48(1) (2019) 285-309.

[2] W. Hou, X. Guo, X. Shen, K. Amine, H. Yu, J. Lu, Solid electrolytes and interfaces in all-solid-state sodium batteries: Progress and perspective, Nano Energy 52 (2018) 279-291.

[3] J. Souquet, Glasses as electrolytes and electrode materials in lithium batteries, J. Power Sources 26(1-2) (1989) 33-35.

[4] R. Chen, W. Qu, X. Guo, L. Li, F. Wu, The pursuit of solid-state electrolytes for lithium batteries: from comprehensive insight to emerging horizons, Materials Horizons 3(6) (2016) 487-516.

[5] K. Kaup, J.D. Bazak, S.H. Vajargah, X. Wu, J. Kulisch, G.R. Goward, L.F. Nazar, A lithium oxythioborosilicate solid electrolyte glass with superionic conductivity, Adv. Energy Mater. 10(8) (2020) 1902783.

[6] D.H.S. Tan, Y.-T. Chen, H. Yang, W. Bao, B. Sreenarayanan, J.-M. Doux, W. Li, B. Lu, S.-Y. Ham, B. Sayahpour, J. Scharf, E. A.Wu, G. Deysher, H.E. Han, H.J. Hah, H. Jeong, J.B. Lee, Z. Chen, Y.S. Meng, Carbon-free high-loading silicon anodes enabled by sulfide solid electrolytes, Science 373 (2021) 1494-1499.
[7] Y. Zhang, J. Ren, T. Xu, A. Feng, K. Hu, N. Yu, Y. Xia, Y. Zhu, Z. Huang, G. Wu, Covalent bonding of Si nanoparticles on graphite nanosheets as anodes for lithium-ion batteries using diazonium chemistry, Nanomaterials 9(12) (2019) 1741.
[8] Y. Xu, Y. Zhu, C. Wang, Mesoporous carbon/silicon composite anodes with enhanced performance for lithium-ion batteries, J. Mater. Chem. A 2(25) (2014) 9751-9757.
[9] J. Liu, P. Kopold, P.A. van Aken, J. Maier, Y. Yu, Energy storage materials from nature through nanotechnology: a sustainable route from reed plants to a silicon anode for lithium-ion batteries, Angew. Chem. 127(33) (2015) 9768-9772.
[10] X. Li, M. Zhang, S. Yuan, C. Lu, Research progress of silicon/carbon anode materials for lithium-ion batteries: structure design and synthesis method, ChemElectroChem 7(21) (2020) 4289-4302.
[11] W. Zhang, J. Li, P. Guan, C. Lv, C. Yang, N. Han, X. Wang, G. Song, Z. Peng, One-pot sol-gel synthesis of Si/C yolk-shell anodes for high performance lithium-ion batteries, J. Alloys Compd. 835 (2020) 155135.
[12] Z. Hou, X. Zhang, J. Liang, X. Lia, X. Yan, Y. Zhu, Y. Qian, Synchronously synthesized Si@C composites through solvothermal oxidation of $Mg_2Si$ as lithium ion battery anode, RSC advances 5(87) (2015) 71355-71359.
[13] Y. Zhang, P. Wang, T. Zheng, D. Li, G. Li, Y. Yue, Enhancing Li-ion battery anode performances via disorder/order engineering, Nano Energy 49 (2018) 596-602.
[14] Y.F. Zhang, P.X. Wang, G.D. Li, J.H. Fan, C.W. Gao, Z.Y. Wang, Y.Z. Yue, Clarifying the charging induced nucleation in glass anode of Li-ion batteries and its enhanced performances, Nano Energy 57 (2019) 592-599.
[15] J. Yan, T. Zhao, N. Shi, H. Zhan, J. Ren, Y. Zhang, Y. Yue, Impact of silicon doping on the structure and crystallization of a vanadium-tellurite glass, J. Non-Cryst. Solids 589 (2022) 121651.
[16] J. Kjeldsen, Y. Yue, C.B. Bragatto, A.C. Rodrigues, Electronic conductivity of vanadium-tellurite glass-ceramics, J. Non-Cryst. Solids 378 (2013) 196-200.
[17] I. Joni, L. Nulhakim, M. Vanitha, C. Panatarani, Characteristics of crystalline silica ($SiO_2$) particles prepared by simple solution method using sodium silicate ($Na_2SiO_3$) precursor, Journal of Physics: Conference Series, IOP Publishing, 2018, p. 012006.
[18] W. Yang, W. Huang, Q. Zheng, W. Huang, Z. Chen, High Efficiency Preparation, Structure and Properties of Silicon Nano-Crystals by Induction Plasma Method, NanoWorld J 2(3) (2016) 63-68.

[19] S. Rada, E. Culea, V. Rus, M. Pica, M. Culea, The local structure of gadolinium vanado-tellurite glasses, J. Mater. Sci. 43(10) (2008) 3713-3716.
[20] C. O'Dwyer, V. Lavayen, S.B. Newcomb, M.A. Santa Ana, E. Benavente, G. Gonzalez, C.S. Torres, Vanadate conformation variations in vanadium pentoxide nanostructures, J. Electrochem. Soc. 154(8) (2007) K29.
[21] M.D. Kaya, B.C. Sertel, N.A. Sonmez, M. Cakmak, S. Ozcelik, Thickness-dependent physical properties of sputtered $V_2O_5$ films and Ti/$V_2O_5$/n-Si Schottky barrier diode, Appl. Phys. A 126(11) (2020) 1-11.
[22] D.S. Jensen, S.S. Kanyal, N. Madaan, M.A. Vail, A.E. Dadson, M.H. Engelhard, M.R. Linford, Silicon (100)/$SiO_2$ by XPS, Surf. Sci. Spectra 20(1) (2013) 36-42.
[23] G. Silversmit, D. Depla, H. Poelman, G.B. Marin, R. De Gryse, An XPS study on the surface reduction of $V_2O_5$ (0 0 1) induced by Ar+ ion bombardment, Surf. Sci. 600(17) (2006) 3512-3517.
[24] M. Taha, S. Walia, T. Ahmed, D. Headland, W. Withayachumnankul, S. Sriram, M. Bhaskaran, Insulator–metal transition in substrate-independent $VO_2$ thin film for phase-change devices, Scientific reports 7(1) (2017) 1-10.
[25] Y. Xu, Y. Zhu, C. Wang, Mesoporous carbon/silicon composite anodes with enhanced performance for lithium-ion batteries, J. Mater. Chem. A 2(25) (2014) 9751-9757.
[26] S. Ashraf, R. Mehek, N. Iqbal, T. Noor, G. Ali, A. Wahab, A.A. Qayyum, A. Ahmad, ZIF 67 derived Co–Sn composites with N-doped nanoporous carbon as anode material for Li-ion batteries, Mater. Chem. Phys. 270 (2021) 124824.
[27] C. Gao, Z. Jiang, S. Qi, P. Wang, L.R. Jensen, M. Johansen, C.K. Christensen, Y. Zhang, D.B. Ravnsbæk, Y. Yue, Metal-Organic Framework Glass Anode with an Exceptional Cycling-Induced Capacity Enhancement for Lithium-Ion Batteries, Adv. Mater. 34(10) (2022) 2110048.
[28] X. Hu, J. Jia, G. Wang, J. Chen, H. Zhan, Z. Wen, Reliable and General Route to Inverse Opal Structured Nanohybrids of Carbon-Confined Transition Metal Sulfides Quantum Dots for High-Performance Sodium Storage, Adv. Energy Mater. 8(25) (2018) 1801452.

Supplementary Materials

# Optimizing Si/vanadium-tellurite glass composites as superior anodes for Li-ion batteries by hot pressing

Jiajia Yan[a], Xiangyu Li[b], Nian Shi[c], Xianglong Ren[d], Hemin Zhou[d], Haizheng Tao[d], Jinjun Ren[c], Ang Qiao[d], Yanfei Zhang[b]*, Yuanzheng Yue[a]*

[a]Department of Chemistry and Bioscience, Aalborg University, 9220 Aalborg, Denmark
[b]School of Materials Science and Engineering, Qilu University of Technology (Shandong Academy of Sciences), Jinan 250353, China.
[c]Key Laboratory of Materials for High Power Laser, Shanghai Institute of Optics and Fine Mechanics, Chinese Academy of Sciences, Shanghai 201800, China.
[d]State Key Laboratory of Silicate Materials for Architectures, Wuhan University of Technology, Wuhan 430070, China

*Corresponding authors. zhang-yanfei@hotmail.com (Y.F. Zhang); yy@bio.aau.dk (Y.Z. Yue).

**This file includes:**

Fig. S1

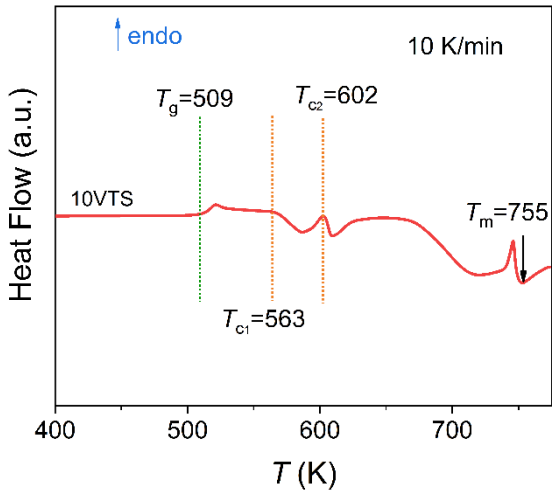


Fig. S1 DSC upscan curve of 10VTS, which is obtained at the rate of 10 K/min in argon. The characteristic temperatures such as glass transition ($T_g$) and crystallization onset temperatures ($T_{c1}$, $T_{c2}$) are denoted in the curve.

ISSN (online): 2446-1636
ISBN (online): 978-87-7573-820-5

AALBORG UNIVERSITY PRESS